Louisiana State University
LSU Digital Commons

LSU Doctoral Dissertations | Graduate School

2016

Direct Measurements of Nuclear Reactions in Hot Stellar Environments

Kevin Thomas Macon
Louisiana State University and Agricultural and Mechanical College

Follow this and additional works at: https://digitalcommons.lsu.edu/gradschool_dissertations

 Part of the Physical Sciences and Mathematics Commons

Recommended Citation
Macon, Kevin Thomas, "Direct Measurements of Nuclear Reactions in Hot Stellar Environments" (2016). *LSU Doctoral Dissertations*. 3241.
https://digitalcommons.lsu.edu/gradschool_dissertations/3241

This Dissertation is brought to you for free and open access by the Graduate School at LSU Digital Commons. It has been accepted for inclusion in LSU Doctoral Dissertations by an authorized graduate school editor of LSU Digital Commons. For more information, please contactgradetd@lsu.edu.

DIRECT MEASUREMENTS OF NUCLEAR REACTIONS IN HOT STELLAR ENVIRONMENTS

A Dissertation

Submitted to the Graduate Faculty of the
Louisiana State University and
Agricultural and Mechanical College
in partial fulfillment of the
requirements for the degree of
Doctor of Philosophy

in

Physics and Astronomy

by
Kevin Thomas Macon
B.S., University of North Carolina at Chapel Hill, 2010
August 2016

To Mom and Dad: Thomas Kent Macon and Jo Elaine Macon

Acknowledgments

First of all, I thank my advisor Dr. Jeffrey Blackmon for opening up numerous opportunities to get involved in several research projects in the lab downstairs at LSU, across the country, and beyond. Jeff taught me many physics and life lessons, but I still have much I could learn from him. Thanks to the Louisiana State Board of Regents and the US Department of Energy grant number DE-FG02-96ER40978 for supporting my graduate studies. It was a pleasure to be a part of the LSU nuclear physics group, and I also thank Dr. B. Charles Rasco and Dr. Catherine Deibel for their advice and guidance. I thank my committee for taking their time to provide advice and feedback on my dissertation.

I also thank Dr. Ingo Wiedenhöver, Dr. Lagy Baby, Dr. Evgeniy Koshchiy, and Dr. Grigory Rogachev for their countless hours and effort working with me during experiments at the John D. Fox Superconducting Accelerator Laboratory at FSU. I would like to thank Dr. Jolie Cizewski, the Center of Excellence for Radioactive Ion Beam Studies for Stewardship Science, and the NNSA Stewardship Science Academic Programs for exposing me to exciting research areas associated with the national labs and funding my eight week practicum at LANSCE.

A special thanks Dr. Aaron Couture and Dr. Shea Mosby for mentoring me, giving me the opportunity to work on DANCE, and making the ^{67,68}Zn experiment possible. At LANSCE it was also a pleasure to learn from Dr. John Ullmann, Dr. John M. O'Donnell, and Dr. Marian Jandel. I am also grateful for Dr. Milan Krtička who was instrumental in the DICEBOX simulations that was key piece of this work. Finally, I would like to thank three of my undergraduate professors Dr. Reyco Henning, Dr. Peter Mucha, and Dr. Hugon Karwowski for teaching useful research skills and encouraging me to pursue graduate studies.

Table of Contents

List of Tables

List of Figures

Abstract

Understanding the origins of intermediate mass nuclei requires accurate knowledge of nuclear reaction rates. This thesis addresses two projects targeting measurements of nuclear cross sections relevant in hot astrophysical environments. Direct measurements of neutron capture on ^{67}Zn and ^{68}Zn were performed using the Detector for Advanced Neutron Capture Experiments (DANCE) at the Los Alamos Neutron Science Center (LANSCE). A new $^{68}\mathrm{Zn}(n,\gamma)$ cross section in the neutron energy range from 150 eV to 850 keV and Maxwellian-Averaged Cross Sections from 20 keV-100 keV are presented along with the details of the analysis. These reaction rates are important for the weak s process that takes place in massive stars and is responsible for the production of a major portion of the elements from mass $60 < A < 90$.

A technical component of this thesis pertains to the development of the LSU-FSU Array for Nuclear Astrophysics and Structure with Exotic Nuclei (ANASEN). This advanced detector technology will be used to perform direct (and indirect) measurements of charged particle nuclear reactions on proton-rich nuclei using radioactive ion beams. Reactions on proton-rich nuclei impact the abundances of intermediate mass nuclei produced in core-collapse supernova and have a substantial impact on understanding observations of Type I X-Ray bursts, the most common stellar explosion. Specifically, we developed an approach using ANASEN for direct measurements of (α, p) reactions that have a significant influence on Type I X-Ray bursts. The results from a $^{14}\mathrm{N}(\alpha, p)$ proof-of-principle test, and progress with direct measurements of (α, p) reactions with the ANASEN active gas target are reported.

Chapter 1
Origin of Intermediate Mass Elements

One of the driving goals in nuclear astrophysics is understanding the observed abundances of the elements. It was recognized in the 20^{th} century that the solar system abundances heavier than the iron group must be predominantly formed from neutron-capture processes, and that two distinct classes of environments must contribute to the observed abundances [14, 15, 16]. Charged-particle reactions on such isotopes are generally unfavorable because of the low probability of penetrating the Coulomb barrier at astrophysical energies, whereas there is no such hindrance for neutron captures.

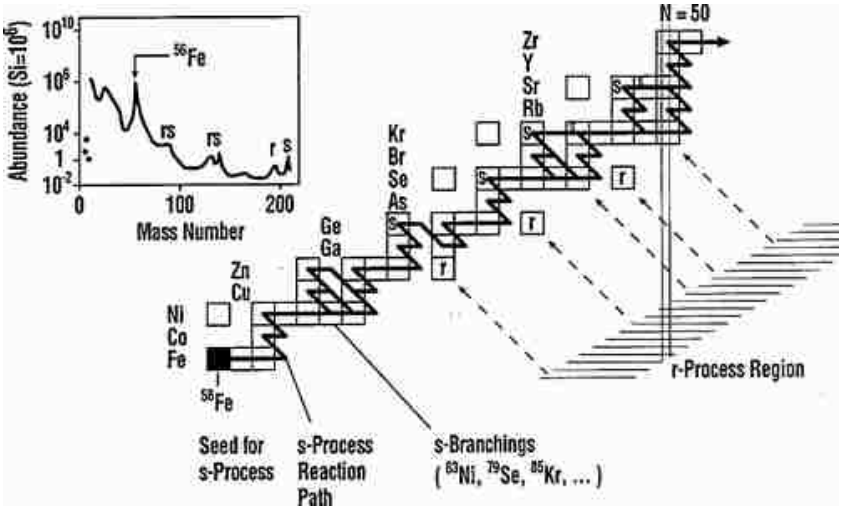

FIGURE 1.1: A portion of the chart of the nuclides showing the s process path and the r process region where horizontal paths are neutron captures, and diagonal lines are beta decays. Specific nuclei that are produced by the r process or s process alone are shown labeled by the letter s or r respectively. The solar system isotopic abundance distribution is shown in the inset. (Figure taken from [1].)

The neutron-capture processes responsible for the formation of the nuclei between iron and the actinides are illustrated in Figure 1.1. The double-peaked struc-

ture in the abundance pattern shown in the inset of Figure 1.1 arises from the two distinct time scales for neutron captures in the s and r process causing isotope abundances to accumulate at closed neutron shells (for example at the N=50 shell closure) in different mass regions. The rapid neutron-capture process (the r process) takes place far from beta stability on a very short time scale and the isotopes of interest have thus far been largely inaccessible to experiments. In contrast, the slow neutron-capture process (the s process) takes place over a timescale of tens of thousands of years, with the mean time between sequential neutron captures on the order of tens to hundreds of years. In the s process, neutron captures take place primarily on stable nuclei that can be studied in the laboratory. Precise cross section measurements of s process reactions are key in interpreting evidence of other nucleosynthetic processes, since they allow a robust determination of s process abundances that can be subtracted from the solar system distribution.

A simplified model, called the classical model of the s process, is useful for understanding the general features of the s process abundance pattern and the astrophysical environment in which it takes place. In the classical s process model, two drastically different exponential neutron exposure components are required to explain the observed abundances and have come to be known as main and weak components of the s process. The results of a two component exposure fit to the product of cross section and abundance is illustrated in Figure 1.2 [17]. At equilibrium, this product is constant explaining the stair-step dependence in the main s process in Figure 1.2 [17] where equilibrium is approximately achieved between neutron magic numbers. While such a site-independent analysis determines the conditions of the necessary stellar environment (i.e. neutron exposure, initial metallicity, and time scale), detailed stellar and galactic chemical evolution models

are also required to fully understand the detailed abundances, especially those of branch points and the weak s process isotopes [18, 19, 2].

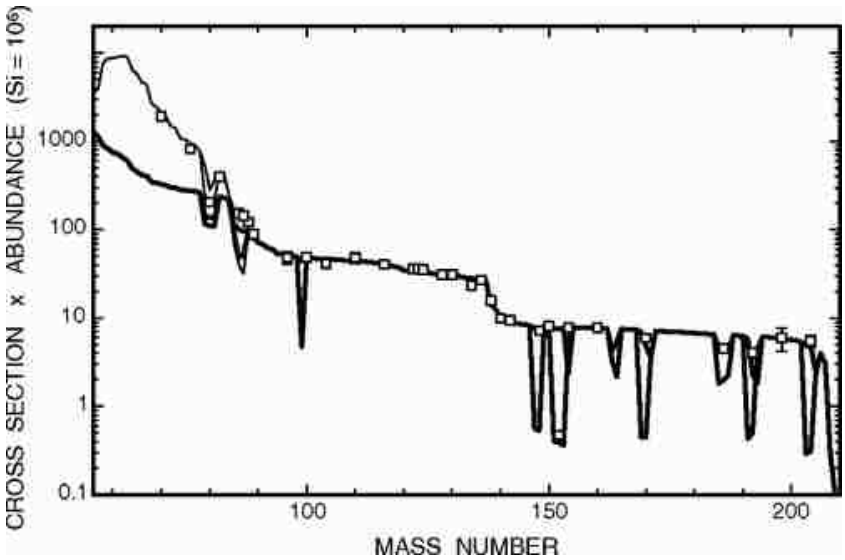

FIGURE 1.2: The product of cross section and s-process abundance is plotted as a function of mass number where open squares are the known abundances of s-only nuclei. The thick (thin) lines represent the main and (main+weak) s process components [1].

The abundance pattern for the main component of the s process arises from neutron production in 1.5 to 3 solar mass Asymptotic Giant Branch (AGB) stars and is relatively well understood. This is a result of a large amount of directly measured nuclear data [20, 11], known solar abundances for a large number of isotopes (s-only isotopes) that can only be produced in the s process, and measured isotopic ratios from pre-solar grains originating in AGB stars [21]. For the main s process, an important remaining nuclear uncertainty is due to uncertain neutron capture cross sections on branch points, which occur when the s-process flow reaches a radioactive isotope with a β-decay half-life comparable to the time between neutron captures. This causes s-process nucleosynthesis to split into two paths that result in the sharp dips in Figure 1.2. Measuring neutron capture cross sections on these radioactive branch-point isotopes can provide a constraint for

stellar s-process models, but these experiments are extremely difficult where the detector rate limit places constraints on the maximum sample mass and minimum neutron flux feasible [22].

Less well understood is the weak s process taking place in massive stars (8-25 solar masses) that undergo significant mass loss and eventually explode as Type II Supernovae. There are fewer s-only nuclides in weak s process mass region ($60 > M > 90$) to constrain calculations, and only recently have detailed models started to address nucleosynthesis in the weak s process. Uncertainties in reaction rates effecting neutron production via $^{22}\mathrm{Ne}(\alpha, n)$ are a main uncertainty for weak s process abundance predictions. The weak s process abundance calculations are also sensitive to the initial CNO seed abundance assumed in the model. Furthermore, new neutron capture cross section measurements are required to reduce the uncertainties in abundance predictions in the weak s process [2].

Observations of metal-poor stars also provide elemental abundance data that reveal information about nucleosynthesis in the early Galaxy [23]. Subtracting the expected s-process abundance distribution from the solar system abundances provides a residual abundance that is strikingly similar to the abundances seen in metal poor stars for elements heavier than tin. The observed abundances of some elements that are believed to be primarily formed in the rapid neutron-capture process (e.g. Eu) do not generally correlate with the production of iron (primarily originating in supernovae), and evidence is mounting for rarer scenarios such as neutron star mergers as the source of the r process in the early Galaxy [24, 25].

Later stages of massive star evolution may also play an additional role in the production of the intermediate mass nuclei (from nickel to tin). Star-to-star comparisons of abundances show an excess of intermediate mass elements in the metal-poor stars HD88609 and HD122563 providing evidence for an additional primary

process, called the Light Element Primary Process (LEPP), that contributes to the production of intermediate mass elements in the early Galaxy [26, 27, 23]. The elemental abundance pattern between the iron group and tin shows substantial variation from star-to-star, and abundances in this region correlate with the production of iron, suggesting an association with core-collapse supernovae [24, 25].

Site independent studies are able to reproduce the LEPP abundance pattern using a neutron-capture process called a weak r process [23]. Another proposed scenario is an s process taking place in fast rotating massive stars where neutron production at low metallicity is possible due to primary production of the $^{22}\mathrm{Ne}(\alpha, n)$ neutron source [28, 29]. In addition, results from core-collapse supernovae simulations have been shown to favor proton-rich conditions, and a sequence of proton capture reactions on proton-rich nuclei aided by neutrino-induced reactions (the νp-process) can occur in neutrino-driven winds of core-collapse supernova and may be the site for the LEPP [30, 31].

Site independent classical s-process analyses are also able to reproduce the general features of the abundances produced by the r-process [17], determining abundances especially for intermediate mass nuclei require more careful analysis [18, 19, 23]. Early comparisons between the solar residual abundances for intermediate mass nuclei showed significant deviations, especially for the lighter elements (Sr, Y, and Zr), from the LEPP abundance pattern seen in metal-poor observations [27]. Only after including a more detailed description of the main s-process component in AGB stars and the weak s process component in massive stars does the solar residual abundance pattern begin to agree with that observed in metal-poor stars [18, 19, 23].

In order to build a better understanding of the origin of intermediate mass nuclei, direct measurements to reduce uncertainties in nuclear data are essential. More

accurate data on neutron capture reactions important for the s process are pivotal for residual abundance determinations that serve as the basis for understanding the r process and the LEPP. A new frontier is also emerging as measurements of nuclear data involving radioactive nuclei that are important in stellar explosions like supernovae and X-Ray bursts are becoming possible at radioactive ion beam facilities. Both frontiers are complementary in reducing uncertainties in the nuclear physics that helps to constrain the interpretation of ever increasing observational data and improve our understanding of the origin of intermediate mass elements.

This thesis includes seven chapters and two appendices. Chapter 1 provides an overview of the complex problem of understanding the origin of intermediate mass elements. A description of the weak s process neutron production is given in Chapter 2 along with a motivation for directly measuring neutron capture on stable, neutron rich zinc isotopes. Chapter 3 is a discussion of the technical details of a $^{67,68}\mathrm{Zn}(n,\gamma)$ neutron capture experiment, data analysis, and methods. Results from the $^{67,68}\mathrm{Zn}(n,\gamma)$ experiment are given in Chapter 4. A motivation for direct measurements with radioactive ion beams using the Array for Nuclear Astrophysics and Structure with Exotic Nuclei (ANASEN) is given in Chapter 5. Current developments, preliminary results, and an outlook on the future of ANASEN are presented in Chapter 6. Finally, a conclusions section highlighting the work and results achieved in this thesis are given in Chapter 7.

Chapter 2
^{68}Zn Experiment Motivation

2.1 The Weak s Process

The weak s process is the slow neutron capture process that occurs in massive stars (8 - 25 solar masses) producing most of the s process isotopes between iron and strontium. The dominant neutron source in the weak s process is the alpha-driven $^{22}\mathrm{Ne}(\alpha, n)$ reaction. The neutron production begins with an initial CNO metallicity that is converted to ^{14}N in core hydrogen burning in the star [32, 33, 2]. The initial CNO metallicity assumed in weak s process stellar models linearly affects the weak s process neutron production [32, 33, 2]. In the early stages of core helium burning ^{14}N is converted into ^{18}O via the $^{14}\mathrm{N}(\alpha,\gamma)^{18}\mathrm{F}(\beta^{+}\nu)^{18}\mathrm{O}$ reaction path [34], and ^{22}Ne is produced by $^{18}\mathrm{O}(\alpha,\gamma)^{22}\mathrm{Ne}$ when core temperatures reach 2.5×10^8 K towards the end of core helium burning and He exhaustion [33, 34]. The remaining helium present in the core provides neutrons for the weak s process via the $^{22}\mathrm{Ne}(\alpha, n)$ reaction when temperatures have reached 3×10^8 K producing neutrons with an effective energy (kT) of 30 keV. This helium core burning phase results in a peak neutron exposure of 10^6 n/cm^3 over a time scale of 100,000 years [13, 2].

A fraction of the ^{22}Ne produced in the core remains after the end of helium exhaustion [2, 32]. The $^{22}\mathrm{Ne}(\alpha, n)$ neutron source reaction is re-ignited with α particles produced in carbon burning by the $^{12}\mathrm{C}(^{12}\mathrm{C}, \alpha)$ reaction [2]. Carbon burning takes place at approximately 1×10^9 K producing neutrons with an effective energy (kT) of 90 keV over a much shorter time scale of less than a year [35, 2] with a peak neutron exposure of 10^{12} n/cm^3. Nucleosynthesis in shell helium burning is significantly affected by proceeding supernova explosion, and the core carbon

burning region will eventually collapse in a neutron star or black hole thus do not affect the s process abundances [2].

2.2 Sensitivity Studies and the Role of $^{66-68}$Zn

In a recent study by Pignatari *et al.*, the impact of updated neutron capture rates since the Bao *et al.* reaction rate compilation [20] were evaluated for their affects on abundances in the weak s-process [2]. Recent improvements on cross sections of stable Ni isotopes showed that the nucleosynthesis in this regime is not in local equilibrium. Thus improving the cross section on one isotope has an effect on many isotopes downstream [36, 37, 16, 13]. For the weak s process, reaction rates are needed both at core helium burning temperatures ($kT = 30$ keV) and at carbon shell-burning temperatures ($kT = 90$ keV) especially when neutron capture cross sections are sufficiently small (<150 mb) [2].

A sensitivity study by Pignateri *et al.* specifically called for new measurements on the $^{66-68}$Zn isotopes [2]. Shown in Figure 2.1 are the results of a sensitivity study varying the standard ^{68}Zn(n,γ) rates by a factor of 1.5 that affects the predicted abundances up to rubidium. This 50% variation is larger than the modestly reported uncertainties ($\approx$ 10%); however, recent evaluation of previous data on ^{nat}Zn resulted in a 30% reduction in the ^{67}Zn(n,γ) Maxwellian Averaged Cross Section at kT=30 keV [6, 38]. The zinc isotopes (^{66,68}Zn) being specifically important because, in the weak s process, lighter nuclei with low capture cross sections have a greater impact on the entire mass region and must be known to a precision of 10% or better [2].

There is a significant effort to improve the neutron capture cross sections needed for nucleosynthesis calculations [20, 38, 2]. In this region, recent calorimeter measurements on isotopes with small neutron capture cross sections (^{62}Ni,^{63,65}Cu, ^{74,76}Ge, and ^{75}As) reveal systematic discrepancies with previous measurements

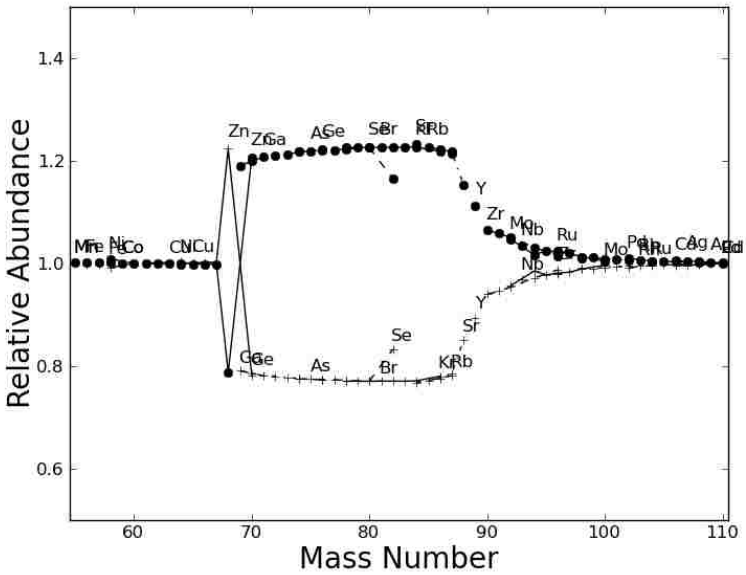

FIGURE 2.1: Relative overabundance for isotopes of interest following C-shell burning in a 25 $M_\odot$ star with an initial solar metallicity. Solid circles show the impact of scaling up the standard ^{68}Zn(n,γ) by 1.5 while the crosses show the effect of decreasing the cross section by a factor of 1.5 [2].

most likely due to improperly accounting for the scattered neutron background or ambiguities arising from target inpurities [37, 16, 39, 40]. Recently recommended $^{66-68}$Zn accepted cross sections up to 100 keV are based on recent adjustments of the combined results of Garg *et al.* and Agrawal *et al.* [41, 42, 43] in a systematic evaluation of five stable zinc isotopes ^{64,66,67,68,70}Zn using elemental zinc neutron capture cross section data. Above 100 keV a coupled-channels optical model calculation parameterizes the cross section fit to experimental data up to 3 MeV [6]. The ^{68}Zn$(n,\gamma)^{69m}$Zn cross section has also recently been revisited via activation at $kT = 30$ keV [44]. However, the germanium detector γ-counting measurement was limited to the partial cross section to the metastable state ($T^m_{1/2}$=13.76 h) because the experiment was not optimized for measuring the ground state of ^{69}Zn that decays by β-emission with a much shorter half-life ($T^{g.s.}_{1/2}$=56.4 m).

Chapter 3
^{68}Zn Neutron Capture Experiment

The ^{68}Zn neutron capture experiment was performed with the Detector for Advanced Neutron Capture Experiments (DANCE) at Los Alamos National Laboratory. DANCE is a BaF_2 calorimeter located at a dedicated flightpath at the Manuel Lujan Center at the Los Alamos Neutron Science Center (LANSCE) in Los Alamos, New Mexico. At LANSCE, a high intensity pulsed proton beam is accelerated to 800 MeV by a linear accelerator. The proton beam, bunched in 250 ns wide pulses, impinges on a water-cooled tungsten production target producing a white source of spallation neutrons [45]. The spallation neutrons are then moderated by the room temperature water surrounding the production target before traveling down multiple flightpaths to various experiments.

The DANCE flightpath shown in Figure 3.1 does not have a direct line of sight to the production target and views only the water moderator. The neutron energy is deduced by the flightpath length, $l_{\text{FP}} = 20.29$ m, and the neutron time-of-flight, t_{TOF} using Equation 3.1. The time-of-flight is measured between a reference to the primary proton pulse and events in the BaF_2 detectors. Since the maximum neutron energy considered in this experiment is 1 MeV the non-relativistic kinematic energy equation can be used to calculate the neutron energy E_n.

$$E_n = \frac{1}{2} m_n \frac{l_{\text{FP}}^2}{t_{\text{TOF}}^2} \tag{3.1}$$

For a given flightpath length, the width of the primary proton pulse combined with the broadening effects of the water moderator are factors that limit the neutron energy resolution achievable. The uncertainty in neutron energy ΔE_n due to an independent time-of-flight uncertainty Δt_{TOF} and flightpath length uncertainty Δl_{FP}

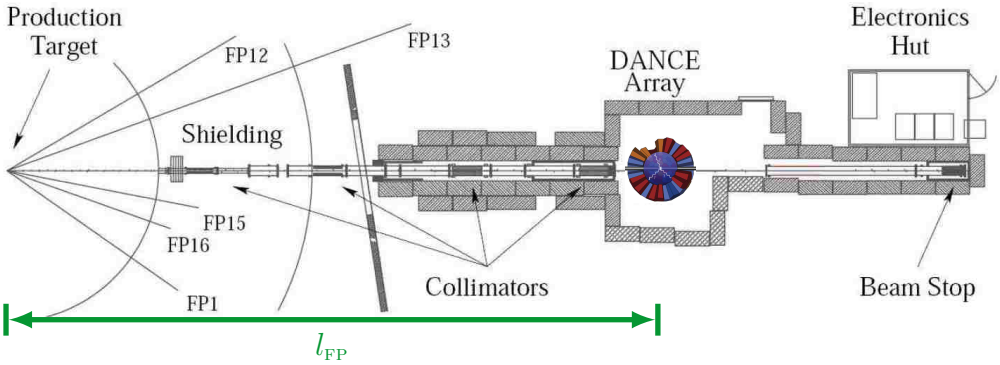

FIGURE 3.1: Flight Path 14 (FP14) illustrating shielding and collimation of the DANCE dedicated neutron beam line [3].

can be propagated from Equation 3.1.

$$\Delta E_n = 2E_n \sqrt{\left(\frac{\Delta l_{\mathrm{FP}}}{l_{\mathrm{FP}}}\right)^2 + \left(\frac{\Delta t_{\mathrm{TOF}}}{t_{\mathrm{TOF}}}\right)^2} \tag{3.2}$$

The neutron energy resolution is modeled in more detail within the framework of the R-matrix code SAMMY allowing the cross section from this experiment to be compared to recommended cross section parameters in §4 [46, 47].

TABLE 3.1: Run log for zinc experiment

Run Number	Time Start	Time Stop	Sample
48488-48505	10/23/2014 17:05:22	10/24/2014 09:46:49	^{68}Zn
48506-48510	10/24/2014 10:36:24	10/24/2014 17:04:30	^{67}Zn
48515-48534	10/24/2014 20:31:33	10/24/2014 18:08:31	^{68}Zn
48847-48881	11/13/2014 00:50:17	11/14/2014 11:40:44	^{68}Zn
48882-48887	11/14/2014 12:02:15	11/14/2014 21:57:39	^{197}Au
48888-48896	11/14/2014 22:17:52	11/15/2014 21:16:51	^{208}Pb (30 mg)
48897-48922	11/15/2014 21:32:48	11/16/2014 18:42:37	^{67}Zn
48923-48936	11/16/2014 19:02:10	11/17/2014 11:16:14	^{68}Zn
49144-49225	12/01/2014 18:51:00	12/05/2014 17:03:13	^{68}Zn
49226-49283	12/05/2014 17:15:38	12/08/2014 08:16:57	^{208}Pb (97.4 mg)
49284-49297	12/08/2014 08:26:39	12/09/2014 07:58:55	^{197}Au
49465-49503	12/17/2014 14:30:51	12/19/2014 09:11:45	^{208}Pb

Measurements on various targets were conducted for beam intensity normalization and background subtraction. Table 3.1 shows the breakdown of the experimental data taken for this experiment. In addition to a measurement of ^{68}Zn(n,γ),

a measurement of ^{67}Zn(n,γ) was also conducted as it is also important for understanding background in the ^{68}Zn enriched sample. Both data sets are important for understanding the systematics of the previous zinc measurements. This work also provides some limited information on the strongest ^{66}Zn(n,γ) resonances.

3.1 DANCE: The Detector for Advanced Neutron Capture Experiments

DANCE is an array of 160 BaF_2 crystals, each 734 cm^3 in volume located at a distance of 19 cm from the target to form a spherical shell. The geometry shown in Figure 3.2 is based on a spherical packing of four distinct crystal shapes totaling 162 modules each viewing the same solid angle [48]. Two of the modules are omitted to allow the neutron beam to enter and exit the detector. With 160 crystals, the array covers a total solid angle of approximately 3.5 π steradians. The solid angle matching for all crystals is crucial for the data interpretation of the number of gamma rays emitted (multiplicity) in the decay cascade following a neutron capture. Since a single gamma-ray can often Compton scatter in more than one detector crystal in DANCE, the measured multiplicity is defined as the number of nearest-neighbor detector clusters that fire. Summing the detector energies within nearest-neighbor clusters defines a cluster energy, E_γ, that is a better representation of individual gamma rays than single crystal energies.

The multiplicity and energy information measured in DANCE is extremely important for understanding the detector efficiency and is a powerful tool that can be used to probe nuclear properties. A 6 cm thick, hollow sphere of LiH surrounds the target position passively shielding the crystals from scattered neutrons [22]. The high detector efficiency ($\approx 87\%$) and segmentation of DANCE provides an active suppression of backgrounds [49]. DANCE functions as a calorimeter by summing the measured energy from all detectors to get the total energy E_{sum}. The neu-

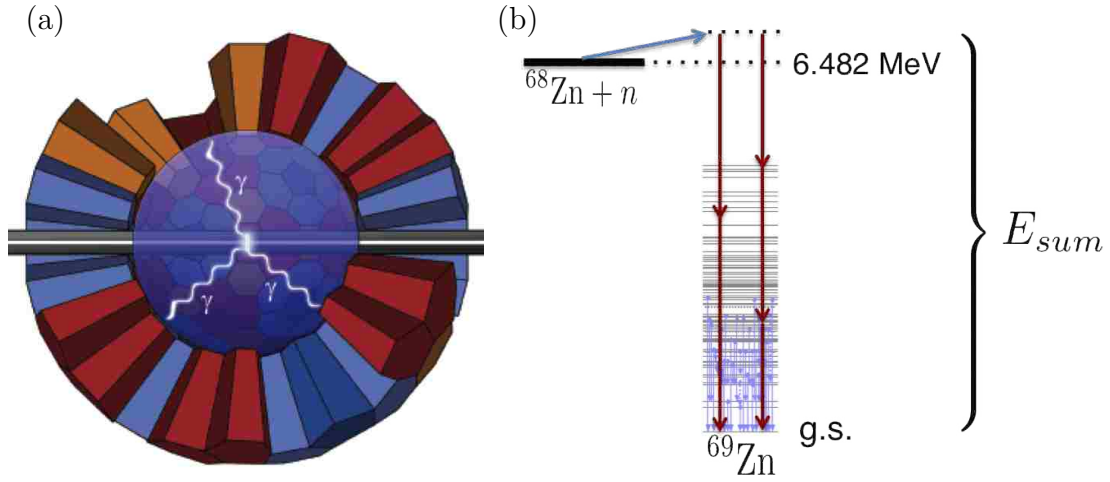

FIGURE 3.2: (a) Schematic representation of DANCE showing the beam-line, lithium hydride sphere, and the four BaF_2 crystal shapes represented by the different colors. (b) Illustration of hypothetical gamma-ray cascades following neutron capture on ^{68}Zn.

tron capture on different isotopes can be identified cleanly when the total energy corresponds to the reaction Q-value: 6.482 MeV for ^{68}Zn(n,γ). The this total energy detected in the detector provides a means for identification and subtraction of backgrounds throughout this analysis.

3.2 Targets

The zinc target material was procured from by Trace Sciences [50] as metal pieces that were bent into layers and fixed with scotch tape so that the target remained within a 5 mm diameter. With non-uniform targets, it is advantageous that the sample be smaller than the central, homogeneous part of the beam that is approximately 7 mm diameter at the target location.

TABLE 3.2: ^{67,68}Zn Targets Composition and Natural Abundances

Isotope	^{64}Zn	^{66}Zn	^{67}Zn	^{68}Zn	^{70}Zn
Natural Abundance	49.17%	27.73%	4.04%	18.45%	0.61%
^{67}Zn (50 mg)	0.12%	5.92%	88.58%	5.38%	<0.01%
^{68}Zn (200 mg)	0.13%	0.10%	0.43%	99.23%	0.09%

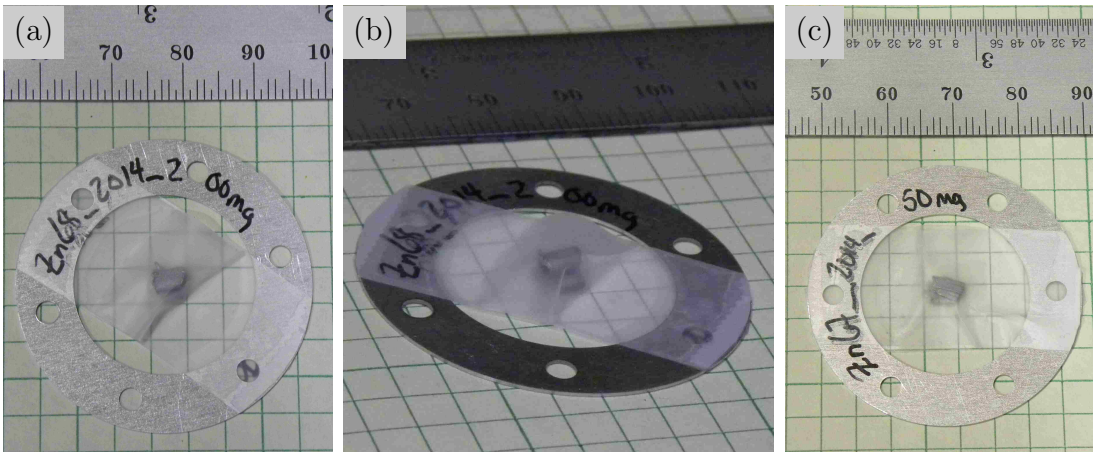

FIGURE 3.3: Photographs of ^{68}Zn, (a) top view and (b) side view, and a photograph of ^{67}Zn (c) illustrating the 5 mm maximal dimensions.

In addition to the zinc targets listed in Table 3.2, two other targets were essential for the experiment. A measurement on a gold target with 4 mm diameter and a thickness of 490 nm ($2.91 \pm 0.12 \times 10^6$ atoms/barn) determined the overall normalization of the neutron flux shape provided by the flux monitors (See §3.4). Two targets of ^{208}Pb, a 30 mg and a 97.4 mg of the same sample bulk, were used as scattering samples in order to characterize the background from neutrons capturing on barium in the detector crystals. The capture cross section for ^{208}Pb has no resonances below approximately 100 keV and is generally much smaller than the neutron scattering cross section [5, 49].

3.3 Calibrations

The energy calibration is performed with standard gamma sources placed at the target position; however, to correct periodic shifts in the detector gains on a run-by-run basis, the intrinsic alpha activity of the BaF_2 crystals is utilized. The alpha activity in the crystals is due to the presence of radium which is a chemical analog to barium. The alpha decay events are clearly separated by comparing a short time integral of the detector signals to a long integral shown in Figure 3.4(c) [48, 49, 4]. The alpha events are removed from the event analysis and are reserved for an

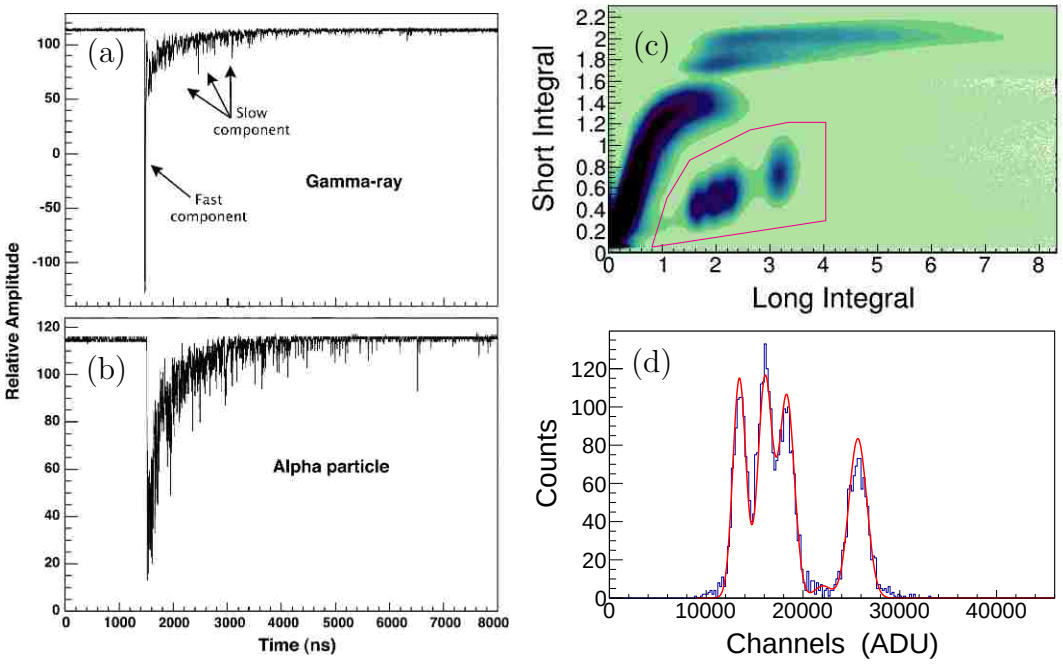

FIGURE 3.4: Figures on the left were taken from [4] of DANCE BaF_2 showing signals produced by gamma rays (a) and alpha events (b). Alpha particles are selected by the pulse shape discrimination cut shown in (c), and a representative alpha decay spectrum fit is shown in (d).

in-situ calibration. An automatic fitting routine then extracts the energies of the alpha peaks providing a reliable relative energy calibration. An example fit from the fitting routine is shown in Figure 3.4(d).

The relative timing between crystals is also calibrated on a run-by-run basis. Time calibrations utilize the large number of Compton scattering coincidences between neighboring crystals. Starting from a reference detector, the calibration is bootstrapped pair-by-pair over the whole DANCE array. The timing calibration and BaF_2 resolution permit imposing a narrow coincidence gate of ± 5 ns (See Figure 3.5). A narrow time coincidence is extremely important to reduce random background in addition to suppressing pile-up events. The background subtraction method described in §3.5 explicitly assumes the absence of pile-up.

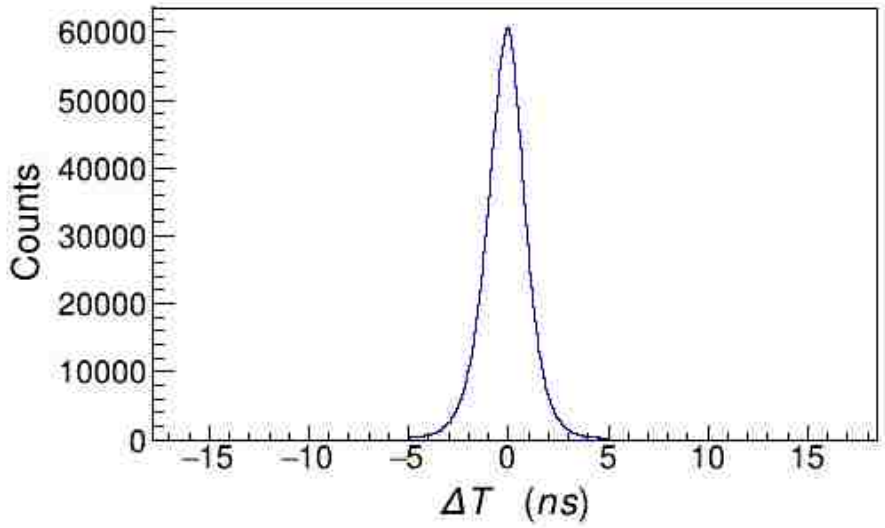

FIGURE 3.5: Representative time difference spectra between two BaF_2 crystals in the DANCE array after calibration.

3.4 Neutron Flux Determination

The neutron flux is measured downstream from DANCE by two complementary neutron monitor detectors: a silicon detector in vacuum with a ^{6}LiF converter foil at 22.59 m, and gas-filled ^{235}U fission chamber at 22.82 m. At low neutron energies (near thermal energies), a ^{3}He proportional counter can be used [51]. For this experiment, only the silicon monitor and ^{235}U fission chamber were used since the energy region of astrophysical interest is near 30 keV and 90 keV.

3.4.1 Neutron Beam Monitors

The number of counts, $Y_{BM}(E_n)$, for a given neutron energy bin, E_n, was measured for the silicon and fission chamber beam monitors. This yield measured by beam monitor BM is proportional to the product of the cross section, $\sigma_{BM}(E_n)$, and neutron flux $\Phi_{BM}(E_n)$ averaged over a given bin: $Y_{BM}(E_n) \propto \Phi_{BM}(E_n)\sigma_{BM}(E_n)$. The determined flux and the cross sections used are shown in Figure 3.6. The neutron flux at the beam monitor location is less than the flux at the target position due to the divergence of the beam. To account for this, a constant geometrical

factor is introduced in the neutron flux normalization of the beam monitor. In previous experiments, this constant correction agrees with the expected beam profile determined by the upstream collimation in DANCE [52, 51]. Combining the beam monitor normalization (thickness, acceptance, and the geometrical factor) into one constant, κ, the incident flux on target, $\Phi^{(0)}$, in units of neutrons/barn can be determined by the following equation:

$$\Phi^{(0)} = \kappa \frac{Y_{BM}}{\sigma_{BM}} \tag{3.3}$$

For the silicon monitor, the $^{6}\mathrm{Li}(n,\alpha)^{3}\mathrm{H}$ cross section is smooth ($\sim 1/v$) up until a broad resonance centered at approximately 240 keV complicates the flux determination. To be conservative, we adopt the silicon monitor only up to 5 keV. The counts in the detector, for each neutron energy bin, are divided by the ENDF/B-VII.1 evaluated cross section for $^{6}\mathrm{Li}(n,\alpha)^{3}\mathrm{H}$ to define the neutron flux from 1 eV to 5 keV neutron energy [5].

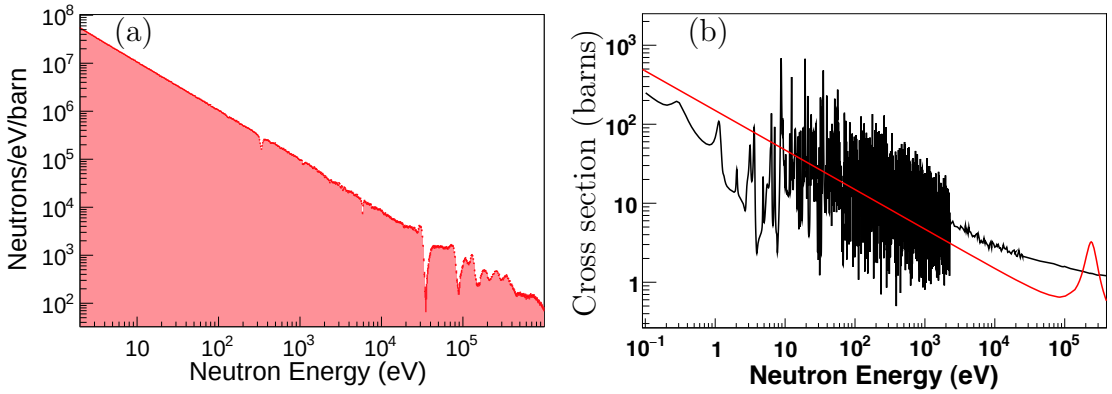

FIGURE 3.6: (a) Normalized neutron flux. (b) ENDF/B-VII.1 Cross section used in the neutron flux determination. The $^{6}\mathrm{Li}(n,\alpha)^{3}\mathrm{H}$ cross section is shown in red and the $^{235}\mathrm{U}(n,f)$ cross section is shown in black.

The fission chamber consists of a gas-filled ion chamber that detects the fragments from neutron-induced fission on a $^{235}\mathrm{U}$ foil inside the chamber. The $^{235}\mathrm{U}(n,f)$ cross section varies rapidly below 3 keV due to a large number of resonances mak-

ing the neutron flux difficult to constrain. At higher energies, above 3 keV, the ^{235}U fission chamber is both more efficient and has a smooth cross section. The counts in this monitor, for each neutron energy bin, are divided by the ENDF/B-VII.1 evaluated cross section for $^{235}\mathrm{U}(n,f)$ to define the neutron flux shape from 5 keV to 1 MeV [5]. The ^{235}U monitor flux is then normalized to the silicon monitor flux in the region from 3 keV to 5 keV. The absolute normalization of the silicon monitor was determined from the data with the gold foil described in the next section. The large dips in the neutron flux above 10^4 keV in Figure 3.6(a) are due to beam attenuation and absorption at strong aluminum and magnesium resonances. The aluminum and magnesium are contained in components of the beam-line shutter assembly at the DANCE flightpath.

3.4.2 ^{197}Au Target Data

A strong $^{197}\mathrm{Au}(n,\gamma)$ resonance, with a peak cross section of 27 kilobarns at $E_n = 4.9$ eV was used to normalize the flux measured at the beam monitor location to the flux at the target position. The number of capture events in a neutron energy bin, $Y^{Au}_{n,\gamma}$, is given by the product of the efficiency for detecting a gamma cascade, $\varepsilon_{cas.}$, the number of neutrons per area Φ, the number of target gold atoms N_{Au} and the cross section $\sigma^{Au}_{n,\gamma}$:

$$Y^{Au}_{n,\gamma} = \varepsilon_{cas.}\Phi N_{Au}\sigma^{Au}_{n,\gamma} \tag{3.4}$$

Out of the total energy of 6.5 MeV in the $^{197}\mathrm{Au}(n,\gamma)$ cascade, the efficiency of detecting at least 150 keV of energy is approximately 100%. Because the threshold is at low energy, the calibration was checked with a standard ^{133}Ba source with a characteristic 356 keV gamma ray energy. Proper subtraction and suppression of low energy backgrounds were also important to ensure that the true number of neutron captures $Y_{n,\gamma}$ was measured accurately.

A blocking time was used to suppress a low energy artifact (§3.4.2.1) requiring a correction for dead time (§3.4.2.2). A linear background subtraction (§3.4.2.3) was performed to the time-of-flight yield spectrum that was then transformed into a neutron energy spectrum using Equation 3.1 resulting in the gold neutron capture yield $Y^{Au}_{n,\gamma}(E_n)$ spectrum. The normalization constant κ in Equation 3.3 was then determined by fitting the data shown in Figure 3.7 by:

$$\sigma^{Au}_{n,\gamma} = \frac{1}{\kappa}\frac{Y^{Au}_{n,\gamma}}{N_{Au}}\frac{\sigma_{BM}}{Y_{BM}} \tag{3.5}$$

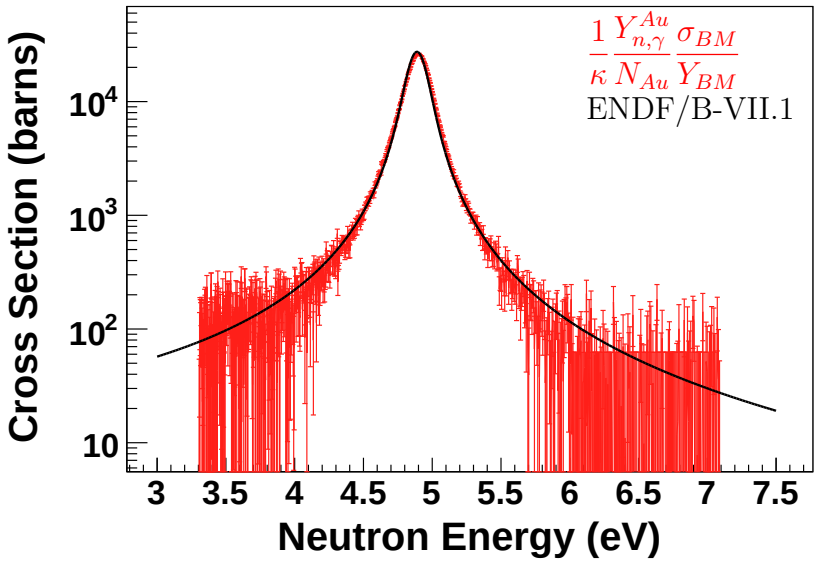

FIGURE 3.7: Fit to the measured spectrum in the region of the 4.9 eV ^{197}Au capture resonance using the evaluated cross section from ENDF/B-VII.1 [5].

The dominant source of uncertainty in the gold normalization comes from a 4% uncertainty in the number of gold atoms determined by Rutherford backscattering with a proton beam. The statistical uncertainty from this gold normalization fit is negligible compared to the 4% systematic uncertainty in the number of gold atoms.

3.4.2.1 Suppressing Re-triggering with Blocking time

Near the single detector threshold of 150 keV, an intense low energy peak was observed at approximately 250 keV in the E_{sum} spectrum correlated with the two strongest ^{197}Au resonances and the production target gamma flash. See [22] for simulations of cascades following ^{197}Au neutron capture with a single detector threshold of 100 keV and 200 keV. The simulations produce an E_{sum} spectra very similar to the background subtracted spectra shown in Figures 3.8 and 3.10.

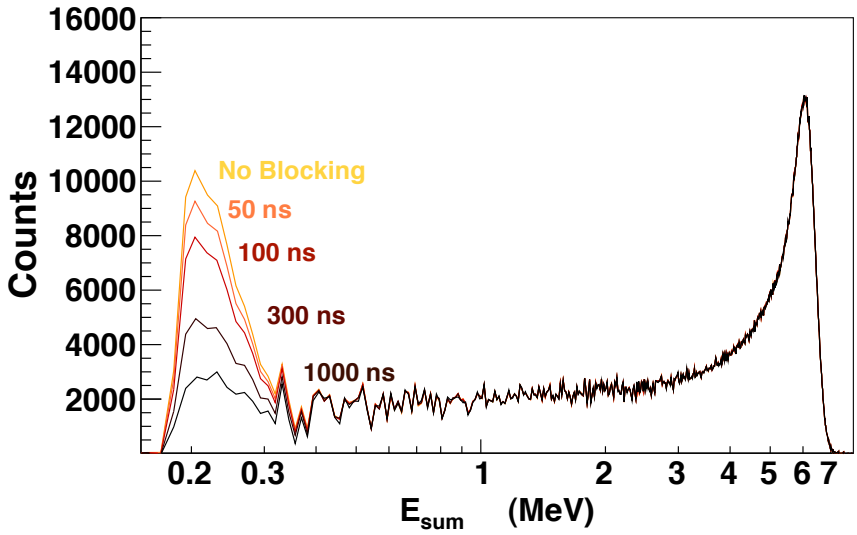

FIGURE 3.8: Background subtracted E_{sum} spectra for blocking times of 0-1000 nanoseconds illustrates a suppression of a low energy artifact that arises from re-triggering at high event rates.

Essentially, this feature is apparent at time-of-flight regions when the detector is experiencing high rates and is attributed to re-triggering on the tails of pulses that is difficult to disentangle. Speculating on possible sources of these after-pulses, one possibility arises from ionization of trace gas molecules inside the photomultiplier vacuum tube. The time scale of ion after-pulses is given by the ion transit time of the tube that can range from hundreds of nanoseconds up to a few microseconds, and this signal is expected to produce tens to hundreds of electrons that matches

the range of expected *photoelectrons* produced by a 200 keV gamma ray [53]. The possibility that these low energy events were due to the decay of an isomeric state populated in ^{198}Au was considered; however, the intensity of this excess (10% of the E_{sum} distribution for a neutron energy of 4.9 eV) is too large and the time scale too long (~ 1 μs) to be attributed to any known isomeric states.

Regardless of the exact source of this excess, it is clearly suppressed by introducing a finite *blocking time*, τ_B. Following an event coincidence gate, all later events within DANCE are vetoed for a time interval set by the blocking time. As seen in Figure 3.8, a blocking time of 1 μs was sufficient to suppress the majority of the low energy background. No further change was observed by increasing the blocking time to 2 μs. This blocking time imposes a dead-time that vetoes valid events within the detector, and a correction described in §3.4.2.2 must be made to determine the real event rate.

3.4.2.2 Dead-time correction

The observed count rate per time-of-flight bin, C'_n, in units of counts per beam pulse is:

$$C'_n = N_c/N_{t0} \tag{3.6}$$

where N_{t0} is the number of beam pulses and N_c is the total number of counts in a time-of-flight bin n. The observed rate, C'_n, in the presence of dead-time τ_B is less than the real event rate C_n. Following the procedure described in [52, 53], the real rate can be calculated by:

$$C_n = -\ln\left(1 - \frac{C'_n}{1-d_n}\right), \quad \text{where } d_n = \sum_{m=n-1}^{\tau_B/\delta t} C'_m \tag{3.7}$$

assuming each time-of-flight bin is statistically independent and the arrival of events for an individual bin is described by Poisson statistics. Since the limits

of the summation run from $m = n - 1$ to $\tau_B/\delta t$, for convenience blocking times used were chosen to be constant multiples of time-of-flight bin width $\delta t = 10$ ns.

Defining a dead-time correction ratio $d_n = C_n/C'_n = N_n/N'_n$ for the count rate in each time-of-flight bin, the number of counts in each bin after applying cuts can be scaled to correct for events lost due to the dead time. This dead-time correction ratio is shown in Figure 3.9 with a maximum value of 10% at the peak of the 4.9 eV $^{197}\mathrm{Au}(n,\gamma)$ resonance.

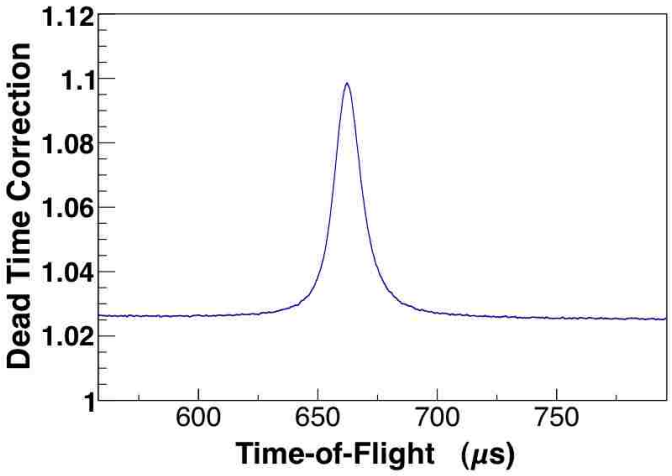

FIGURE 3.9: Dead-time correction for a one microsecond blocking time in a 250 μs time-of-flight window centered on the 4.9 eV resonance.

3.4.2.3 Background Subtraction

Not all of the counts near the strong, isolated 4.9 eV neutron resonance are due to neutron capture. There is background from neutron scattering at this resonance energy; however, this background is strongly suppressed by the LiH sphere surrounding the target position and can be neglected. The dominant background in this time-of-flight region has a smooth time dependence resulting mainly from the ambient neutron background, the decay of neutron-induced reaction products, and random coincidences. This smooth background is assumed linear with neutron energy in the region near the 4.9 eV resonance.

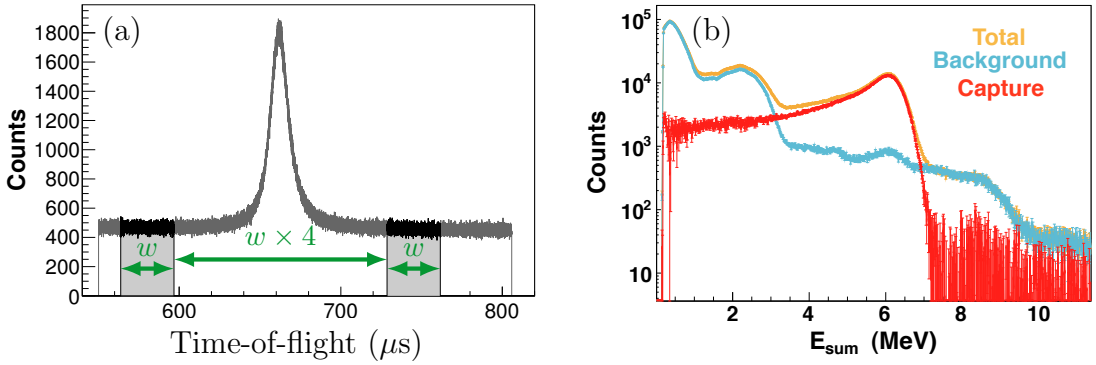

FIGURE 3.10: (a) Counts vs. Time-of-flight near the ^{197}Au resonance showing the background regions (w) and foreground region with width ($w \times 4$). (b) Total energy distribution in the resonance window before subtraction, the background calculated from the two shaded regions, and E_{sum} spectra for ^{197}Au neutron capture.

The background diagnostic shown in Figure 3.10(b) was produced by performing a linear background subtraction on individual projected time-of-flight spectra corresponding to 150 keV wide E_{sum} bins. The slope and offset parameters were allowed to be free parameters with respect to E_{sum} since the background in the time-of-flight spectra is strongly correlated with total energy (See Figure 3.10). After summing over all E_{sum} this is equivalent to a single linear background subtraction under the gold resonance, but the low energy excess shown in §3.4.2.1 would have gone unnoticed without the E_{sum} diagnostic plot. The background measured in the "off-resonance" intervals shown in Figure 3.10(a) were chosen to conveniently have a width w equal to 1/4 the width of the "on-resonance" integral. This allows for a straightforward background subtraction and error propagation similar to the method used in [54], where the integral of a linear background under the resonance is given by the sum of the area of the shaded regions multiplied by a constant. There is some contribution to capture in the "off-resonance" intervals that can be seen by a small peak in the background of Figure 3.10 at the ^{197}Au Q-value of 6.5 MeV; however, this effect is small ($< 0.1\%$) and is neglected.

3.4.3 Thick Target Corrections

Two corrections related to the thick ^{68}Zn target are considered. An attenuation correction is described in §3.4.3.1 that accounts for the reduced flux seen by the monitors, and a target self-shielding correction is discussed in §3.4.3.2. The effect of the target edges, geometrical complexities, and any multiple scattering contribution to the yield are neglected and contribute to a systematic uncertainty in the attenuation correction described in §3.4.3.1. Since a number of assumptions are made in order to determine these analytical correction factors, they are only effective when small because only then can you neglect introduction of the unknown systematic errors due to the simplifications.

3.4.3.1 Transmission Correction for Neutron Monitors

The thick targets used in the zinc measurements require considering the attenuation of neutrons by the target in order to correct the beam monitor flux. For a fixed neutron energy E_n, the number of neutrons attenuated from the beam (-dN) is given by the product of the incident number of neutrons N, the total neutron cross section σ_{tot}, and the target thickness dx with units of (atoms/barn).

$$dN = -N\sigma_{tot}dx \tag{3.8}$$

Equation 3.8 applies to a target of uniform thickness that is much larger than the size of the incident neutron beam eliminating edge effects. Secondly, this applies to the attenuation of a parallel neutron beam, while the beam at DANCE has a small divergence determined by the collimator geometry. Despite these conditions not being met, the number of unreacted neutrons at a given location x in the target can be approximated by:

$$N(x) = N_0 \mathrm{e}^{-\sigma_{tot}x}, \quad \text{where } N_0 = N(0). \tag{3.9}$$

Although the targets are non-uniform, the neutron transmission through the target can be used to define an average thickness and an effective target area. The central portion of the neutron beam (7 mm diameter) is uniform, enabling the cross section measurement with targets of non-uniform thickness. The beam diameter is approximately 1 cm at the target location [52]. The zinc targets were constrained to have 5 mm maximal dimensions, smaller than the area of the beam at the target location. As illustrated in Figure 3.11, the beam monitors are partially shadowed by the ^{68}Zn sample and see a number of neutrons, N_{BM}, that is a mixture of incident neutrons N_0 and transmitted neutrons $N(\tau)$,

$$N_{BM} = \alpha N_0 + \beta N(\tau) = N_0 \left(1 - \beta + \beta \mathrm{e}^{-\sigma_{tot}\tau}\right) \tag{3.10}$$

Where $\beta \approx \dfrac{A_{\text{eff}}}{A_{beam} - A_{\text{eff}}}$ is related to the effective target area (A_{eff}), τ represents an average target thickness, and N_0 is the number neutrons incident on the beam monitors without the ^{68}Zn target in place.

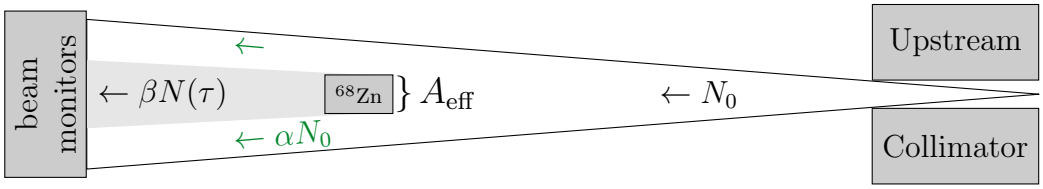

FIGURE 3.11: (*not to scale*) Simplified geometry used to define transmission correction in Equation 3.10.

The relative normalization between N_{BM} and N_0 was fixed in the region near $E_n = 400$ eV constraining $\alpha = 1 - \beta$ where the calculated attenuation is negligible. This is near the 516 eV resonance; however, this is the minimum in the attenuation calculated using the current recommended ^{68}Zn total neutron cross section [5]. A beam attenuation correction factor f_a can be defined from Equation 3.10 to correct the number of neutrons seen by the beam monitors with the ^{68}Zn target in place.

$$f_a = N_{BM}/N_0 = \frac{1}{1 - \beta + \beta \mathrm{e}^{-\sigma_{tot}\tau}} \tag{3.11}$$

The two remaining free parameters β and τ were determined by fitting to the ratio N_{BM}/N_0 using Equation 3.10. The resulting fit with $\beta = 0.27 \pm 0.03$ and $\tau = 0.012 \pm 0.004$ barns^{-1} is shown in Figure 3.12. Approximating the ^{68}Zn target

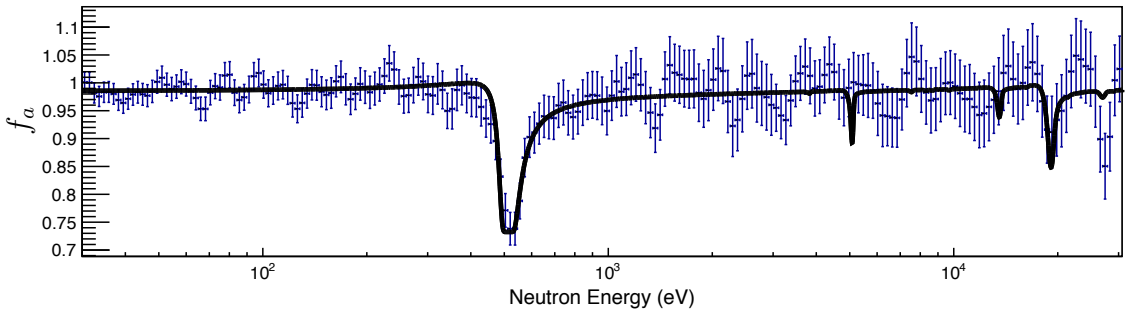

FIGURE 3.12: Transmission probability calculated using the ENDF/B-VII.1 ^{68}Zn total neutron cross section [5]. The calculated transmission is approximately 1 near 400 eV and is used to reduce the number of parameters in the fit.

as a parallelepiped and taking flat, 1 cm diameter beam profile [52] translates β into the effective target area:

$$A_{\text{eff}} = \frac{\pi}{4}\frac{\beta}{1+\beta}\ \text{cm}^2 = 0.17 \pm 0.01\ \text{cm}^2\ (\text{stat}) \tag{3.12}$$

Since the target attenuates all of the neutrons at the peak of the 516 eV resonance, the depth of the transmission probability is sensitive to the target effective area while the width of the transmission resonance constrains the average target thickness. The statistical uncertainties in these best-fit parameters were determined using the MINOS method [55], while the simplifying assumptions made contribute an additional systematic uncertainty.

The effective area 0.17 ± 0.01 cm^2 is consistent with the measured zinc target dimensions and is smaller than the homogeneous portion of the beam. Furthermore, this estimated thickness and effective area correspond to a target mass of (200 ± 60) mg consistent with the mass measured on a balance of 200.5 mg. It is important to note that this uncertainty in the target thickness does not directly influence the cross section results. This effective target thickness is only necessary for target

thickness correction factors, which are small in the astrophysical energy range. The important result from this transmission calculation is a consistency check that indeed the zinc target mass was fully illuminated by the central portion of the neutron beam.

3.4.3.2 Target Self-Shielding Correction

The attenuation correction described in the last section corrects for neutrons that are scattered and not seen by the beam monitors. Another possible correction can be made for self-shielding, which is an attenuation of neutrons inside the target from the target material itself. As illustrated in Figure 3.13(b), a cancellation in the interior of the target diminishes the influence of neutron scattering on the local flux of neutrons. Instead, the downstream side of the target is shielded mainly by capture occurring at the upstream side of the target. The target self-shielding transmission probability, shown in Figure 3.13(a), is calculated using only the neutron capture cross section [5] is only significant near the strong resonance at 516 eV.

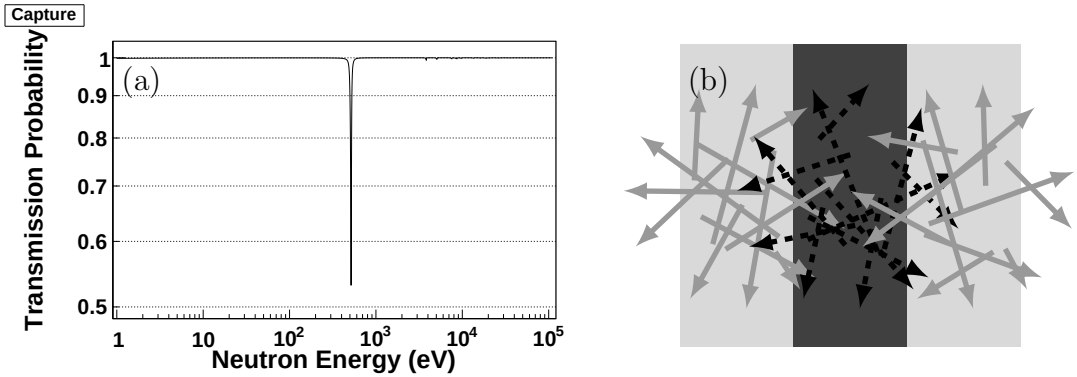

FIGURE 3.13: (a) Transmission Probability through thickness $\tau = 0.01$ barn^{-1} using the ^{68}Zn capture cross section from ENDF/B-VII.1. (b) Simplified picture of how neutrons scattered *out* (dashed arrows) are compensated by neutrons scattering *in* (solid grey arrows) from a neighboring region.

The yield at this resonance is further complicated by multiple scattering prior to capture that is impractical to model analytically given the sample geometry. Furthermore, the neutron energy loss in the kinematics of scattering is entirely neglected here. More importantly, this resonance will not have a significant effect on the Maxwellian-Averaged Cross Section at weak s process temperatures. Thus, only the beam attenuation is corrected for and the target self-shielding is neglected.

3.5 ^{68}Zn Background Subtraction

DANCE is a calorimeter capable of measuring, with high efficiency, the total energy (E_{sum}) of gamma-ray cascades following neutron capture. Calorimeters provide the capability to distinguish, by the reaction Q-value, capture events of interest from events due to scattered neutrons and capture on contaminants in the target. The ability to perform accurate characterization of backgrounds is one of the key features of DANCE [13, 56, 52, 49]. The detected E_{sum} signatures are used to determine the normalizations for subtracting the dominant sources of background from ^{67}Zn contamination and the scattered neutron background. The ^{208}Pb target yield is dominated by neutrons scattering from the target location that are captured on barium isotopes in the detector crystals.

The total counts measured for each target of nominal atomic mass A, lowercase $y^A = y^A(E_{sum}, M; E_n)$, comprises multiple components, capital $Y^{A'} = Y^{A'}(E_{sum}, M; E_n)$ arising from different isotopes in the target of mass A', as a function of neutron energy E_n, total gamma energy E_{sum}, and multiplicity M.

$$\begin{aligned} y^{68} &= Y^{68} + b^{68}Y^{67} + c^{68}Y^{208} \\ y^{67} &= a^{67}Y^{68} + Y^{67} + c^{67}Y^{208} \\ y^{208} &= Y^{208} \end{aligned} \tag{3.13}$$

Each component, ^{67}Zn, ^{68}Zn, and ^{208}Pb, is labeled by the atomic mass ($A = 67, 68, 208$) respectively. Leveraging that a given isotope will produce a characteristic E_{sum} spectrum, the linear coefficients (a^A, b^A, c^A) for each component are assumed independent of E_{sum} and only functions of neutron energy, multiplicity, and target enrichment. The background-subtracted ^{68}Zn yield, Y^{68}, can be determined by solving the system of linear equations relating the target yields shown above.

$$Y^{68} = \underbrace{\frac{1}{1 - a^{67}b^{68}}}_{\simeq 1} \left(y^{68} - b^{68}y^{67} - \left(c^{68} - b^{68}c^{67}\right) y^{208} \right) \tag{3.14}$$

$$= y^{68} - \alpha y^{67} - \beta y^{208} \tag{3.15}$$

The pre-factor in Equation 3.14 can be neglected because the term $a^{67}b^{68}$, although being a function of neutron energy and multiplicity, is on the order of the product of the relative isotopic contamination in each of the enriched zinc targets given in Table 3.2.

$$a^{67}b^{68} \sim \left(\frac{5.38\%}{88.58\%}\right)\left(\frac{0.43\%}{99.23\%}\right) = 2.6 \times 10^{-4}$$

At E_{sum} energies above the ^{68}Zn Q-value peak ($Q_{68} = 6.48$ MeV), in the absence of pile-up events, neutron capture on ^{68}Zn does not contribute to the yield. This allows the background contributions to be constrained by leveraging the characteristic E_{sum} distributions for each component. Summing over a range of multiplicities $M = [2, 5]$, for each fixed neutron energy bin E_n, the total energy spectrum for each target A can be represented as column vector $\mathbf{y}^A_{E_n}$ and related by,

$$\mathbf{y}^{68}_{E_n} - \alpha \mathbf{y}^{67}_{E_n} - \beta \mathbf{y}^{208}_{E_n} = \sum_{M=2}^{5} \widetilde{Y}^{68}(E_{sum}, M; E_n). \tag{3.16}$$

The yield in each E_{sum} bin, weighted by the statistical uncertainty, defines a row element in the column vector $\mathbf{y}^A$ for each component A. The variable $\widetilde{Y}^{68}$ is given

by Y^{68} weighted by the statistical uncertainty. The statistical uncertainties are calculated assuming Poisson statistics.

Equation 3.16 was solved at E_{sum} energies above 7.0 MeV, where $Y^{68} = 0$, using the method of linear least squares. This fitting was performed for each neutron energy bin from 150 eV to 850 keV, and representative background subtraction results are shown in Figure 3.14 for four neutron energy bins. Figures 3.14(c) and 3.14(d) demonstrate the robustness of the background subtraction even in the 10 to 100 keV region where the signal-to-background ratio is low.

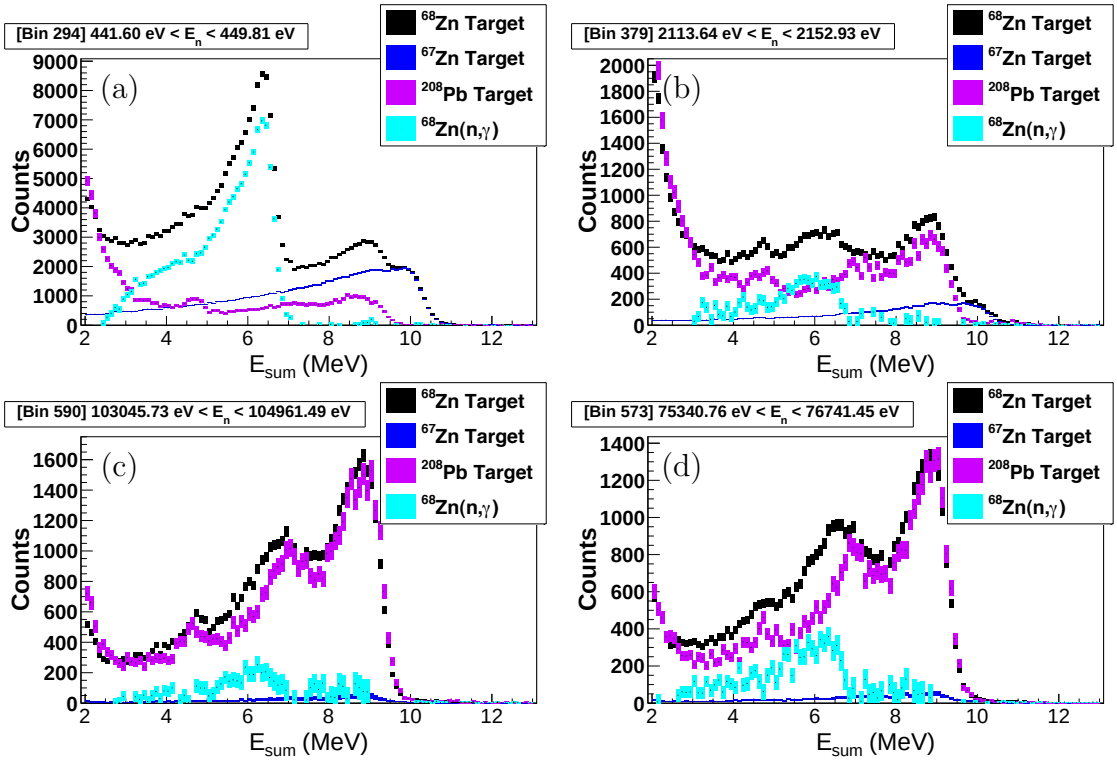

FIGURE 3.14: Representative background-subtracted total energy distributions shown in light blue for selected neutron energy bins for multiplicities $M = [2, 5]$. The neutron scattering background is shown in pink, and the ^{67}Zn background is shown in dark blue. (a) & (b) Examples of background subtractions where both background components are present. (c) & (d) Examples of approximately one dimensional background subtraction.

Throughout the neutron energy range of interest, the ^{67}Zn capture cross section is typically much smaller than the neutron elastic scattering cross section. At neutron energies where the $^{67}\mathrm{Zn}(n,\gamma)$ yield is sufficiently small so that it is not statistically significant, the ^{67}Zn target is then also dominated by the neutron scattering background. In such regions the total energy distributions, E_{sum}, for ^{208}Pb and ^{67}Zn are not linear independent and Equation 3.16 is ill-posed. This causes linear least-squares fitting methods that rely on linear independence or direct matrix inversion to fail. For these reasons, the Singular Value Decomposition linear least-squares method (SVD) described in [57] was chosen to guarantee a solution even in the case of a singularity.

As described in [57], the fitting method calculates the least-squares best-fit using a Singular Value Decomposition of the matrix $\mathbf{A}$ comprised of the two column vectors $\mathbf{y}^{67}$ and $\mathbf{y}^{68}$.

$$\mathbf{A} = \begin{pmatrix} \vdots & \vdots \\ \mathbf{y}^{67}_{E_n} & \mathbf{y}^{208}_{E_n} \\ \vdots & \vdots \end{pmatrix} = \sigma_1 \mathbf{u}_1 \mathbf{v}_1^T + \sigma_2 \mathbf{u}_2 \mathbf{v}_2^T, \qquad \sigma_1 \geq \sigma_2 \tag{3.17}$$

In a Singular Value Decomposition, the vectors $\mathbf{u}_i$ and $\mathbf{v}_i$ are the respective eigenvectors of $\mathbf{A}\mathbf{A}^T$ and $\mathbf{A}^T\mathbf{A}$ with eigenvalues σ_i where i runs from one to the minimum dimension of A.. The Singular Value Decomposition in two dimensions can be interpreted geometrically with $\mathbf{v}_1$ ($\mathbf{v}_2$) defining a coordinate axis parallel (perpendicular) to the least-squares best-fit line of $\mathbf{y}^{67}$ plotted against $\mathbf{y}^{68}$. A threshold placed on the smallest singular value ($\sigma_2 \geq f_{\mathrm{tol}}\sigma_1$) truncates the background fit to one dimension in the case of degeneracy. When the second term in Equation 3.17 is truncated, the vector $\mathbf{u_1}$ defines the shape of the background as a normalized least-squares best-fit to both background components. When the statistical fluctuations in the data are high, a competition between $\mathbf{y}^{67}$ and $\mathbf{y}^{208}$ may persist.

The parameters α and β are highly correlated, which can complicate estimates of the background subtraction statistical error. The SVD method solves the linear equation in an orthonormal basis allowing the uncertainties in α and β to be estimated in the absence of covariances. The fitting was performed using the SVD decomposition and linear solver provided in ROOT [58] similar to the example given in [59].

More can be said about the linear coefficients in Equation 3.16. The enrichment of each target ensures that the parameter α is always positive and less than one. The scattering coefficient, $\beta = c^{68} - b^{68}c^{67}$, describes the neutron scattering contribution of both zinc targets simultaneously. Negative values of β can compensate for over subtracting the scattering background that is present in the ^{67}Zn. This issue only arises at the peak of ^{67}Zn resonance near 200 eV, which is far from the important energy range for astrophysics. At this energy, thick-target effects in the ^{67}Zn sample result in a higher ratio of $^{67}\mathrm{Zn}(n,n)$ to $^{67}\mathrm{Zn}(n,\gamma)$ than in the ^{68}Zn target causing the scattered background component to be over-subtracted.

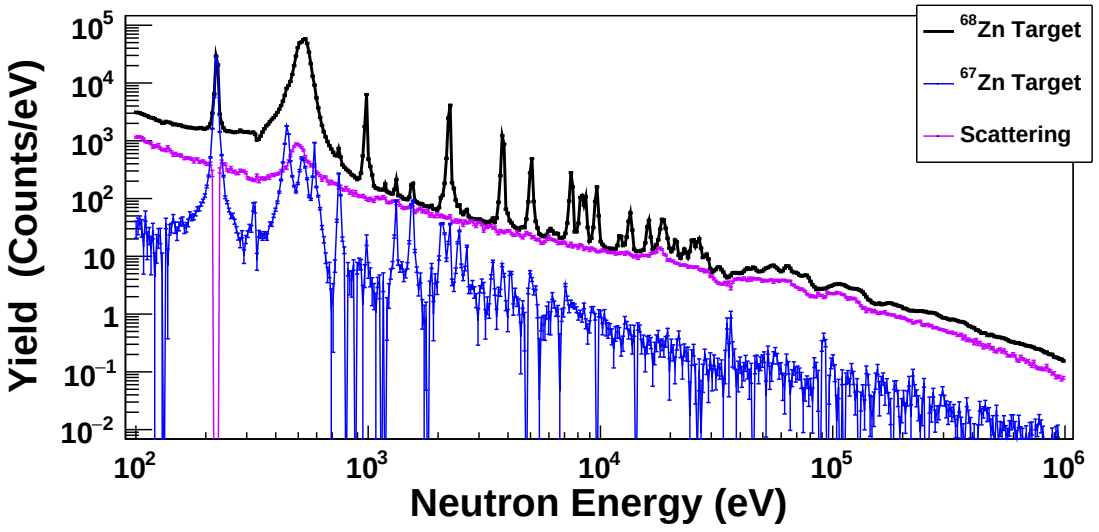

FIGURE 3.15: The ^{68}Zn target total yield is shown in black. The contamination from the ^{67}Zn is shown in dark blue, and the ^{208}Pb scattering used to determine the neutron scattering background is shown in pink.

For a given neutron energy bin, the background contributions are determined by summing over the individual terms in Equation 3.15 corresponding to a chosen E_{sum} range. See Figure 3.15 for a comparison of the background contributions to the ^{68}Zn target yield as a function of neutron energy for multiplicities 2 to 5 and total energies of 3.5 MeV to 7 MeV. Because photons are also a component of the beam below total energies of 3.5 MeV, the background subtraction is problematic due to the systematic difference between the photon scattering on ^{68}Zn and ^{208}Pb samples having different atomic number [49]. The difference in atomic mass results in a systematic shift in the neutron energy distributions following neutron scattering on the ^{68}Zn and ^{208}Pb samples. This leads to a shift in the peaks of the E_{sum} spectra resulting from neutrons capturing on the BaF_2 detectors that increases with neutron energy. This systematic shift explains the "bipolar" shape of the residuals shown in background subtracted E_{sum} spectra, shown in Appendix A, for the neutron energy range of 50 keV to 850 keV. Despite these limitations, the E_{sum} spectra resulting from the background subtractions (shown in this Section and Appendix A) indicate clean ^{68}Zn(n,γ) events for measured E_{sum} energies between 5.0 MeV and 7.0 MeV.

Another interesting feature of the background subtraction is the capability to simultaneously remove the small ^{66}Zn background. Separated by two mass units, the contamination in the ^{68}Zn enriched sample is small, 0.10% (See Table 3.2), and on average the capture cross sections for ^{66,68}Zn are of similar order of magnitude. Yet still, on a strong resonance, the ^{66}Zn(n,γ) reaction is a concern having a Q-value of 7.0 MeV that overlaps with the ^{68}Zn capture Q-value of 6.48 MeV. Conveniently, the ^{67}Zn enriched sample has six times the concentration of ^{66}Zn and is utilized in the background subtraction. The equations listed in this section still directly apply by simply making the label substitution $67 \rightarrow 66$. Thus, the ^{66}Zn

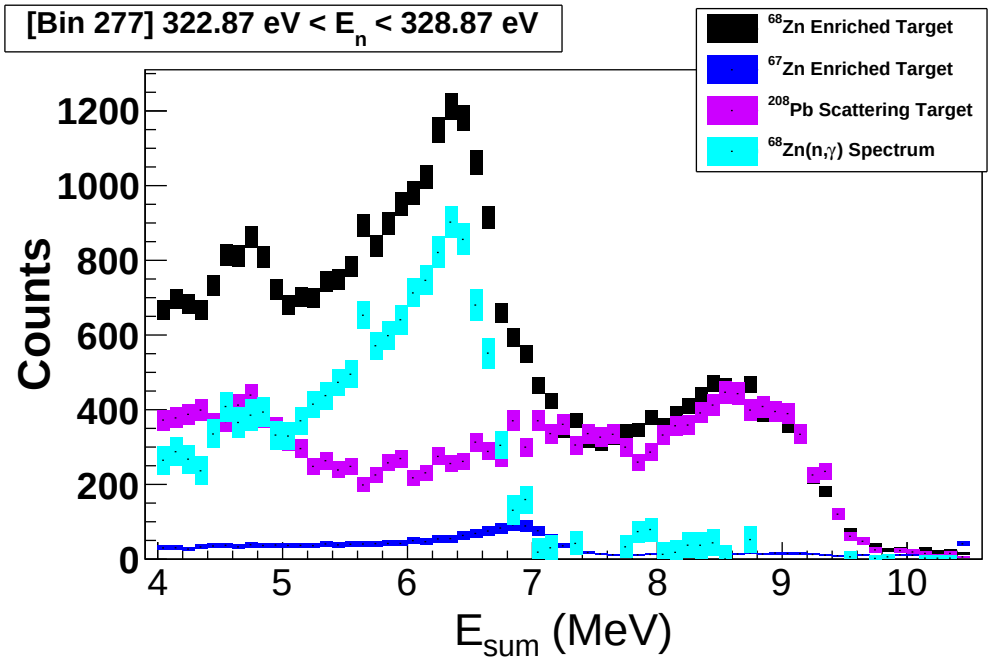

FIGURE 3.16: The background subtraction provided by the ^{67}Zn enriched target also accounts for yield correlated with a 7.0 MeV Q-value indicative of $^{66}\mathrm{Zn}(n,\gamma)$.

background subtraction occurs automatically as long as $^{66}\mathrm{Zn}(n,\gamma)$ and $^{67}\mathrm{Zn}(n,\gamma)$ resonances do not appear at the same neutron energy. Even then, the largest of the two backgrounds will be the one removed. The peak at approximately 300 eV seen in the ^{67}Zn component of Figure 3.15 is actually a $^{66}\mathrm{Zn}(n,\gamma)$ resonance. As shown in Figure 3.16, despite the similar Q-value, the $^{66}\mathrm{Zn}(n,\gamma)$ contribution can be easily identified and cleanly removed in the background subtraction.

3.6 DICEBOX Cascade Efficiency Simulations

If the experimental conditions allow the use of all multiplicities and low energy thresholds (150 keV), as is done for the gold target normalization in §3.4.2, DANCE is approximately 100% efficient. The signal-to-background ratio is also very unfavorable in the single multiplicity data. In the presence of these two limitations, the multiplicity and total energy cuts were chosen be as wide as possible to minimize the uncertainty in the detector efficiency. In the analysis of the zinc data, only events with multiplicities from 2 to 5 and total energies of $E_{sum} = 3.5$ MeV–

7.0 MeV were counted. The efficiency, ε_{cut}, is given by the ratio of counted events to the true number of neutron captures. Given these cuts, the actual efficiency of DANCE is less than 100% and in principle depends on the properties of the emitted gamma-rays, and the efficiency, ε_{cut}, is calculated from simulations.

The efficiency of detecting a gamma-ray from the cascade following a neutron capture depends on the multiplicity and energy distribution of the gamma-ray cascades. The details of the cascades depend ultimately on the properties of the resonant states in the newly formed nucleus, ^{69}Zn, and strongly on the spin-parity of the resonance. To understand the efficiency, gamma-ray cascades were simulated using DICEBOX, which uses the known levels and transitions below a critical energy E_{crit} (1.74 MeV for ^{69}Zn) which are most likely complete. Above the critical energy, the extreme statistical model is used to artificially generate levels and transition probabilities [60]. In DICEBOX, a set of levels are generated using a model for the nuclear level density $\rho(E_a, J_a^{\pi_a})$, then transition probabilities are calculated from partial radiation widths,

$$\Gamma_{ab} = \sum_{X,L} y_{XL}^2 (E_a - E_b)^{2L+1} \frac{f_{XL}(E_a - E_b)}{\rho(E_a, J_a^{\pi_a})}, \tag{3.18}$$

using a model for the photon strength function f_{XL} where y_{XL} is a random variable with zero mean and unit variance. The labels a and b denote the initial and final state and XL represents the type and multipolarity of electromagnetic transition (E1, M1, E2, etc.). The simulation results, shown in detail in Appendix A, were calculated using a constant temperature model for the nuclear level densities and show reasonable agreement with the data [61]. The KMF model was used for the E1 photon strength function [62, 63]. The E2 and M1 photon strength functions were modeled by a combination of spin-flip and single-particle transitions.

Fifteen artificial nuclear realizations for each capture spin-parity were simulated in DICEBOX, with 150000 cascades for each realization.

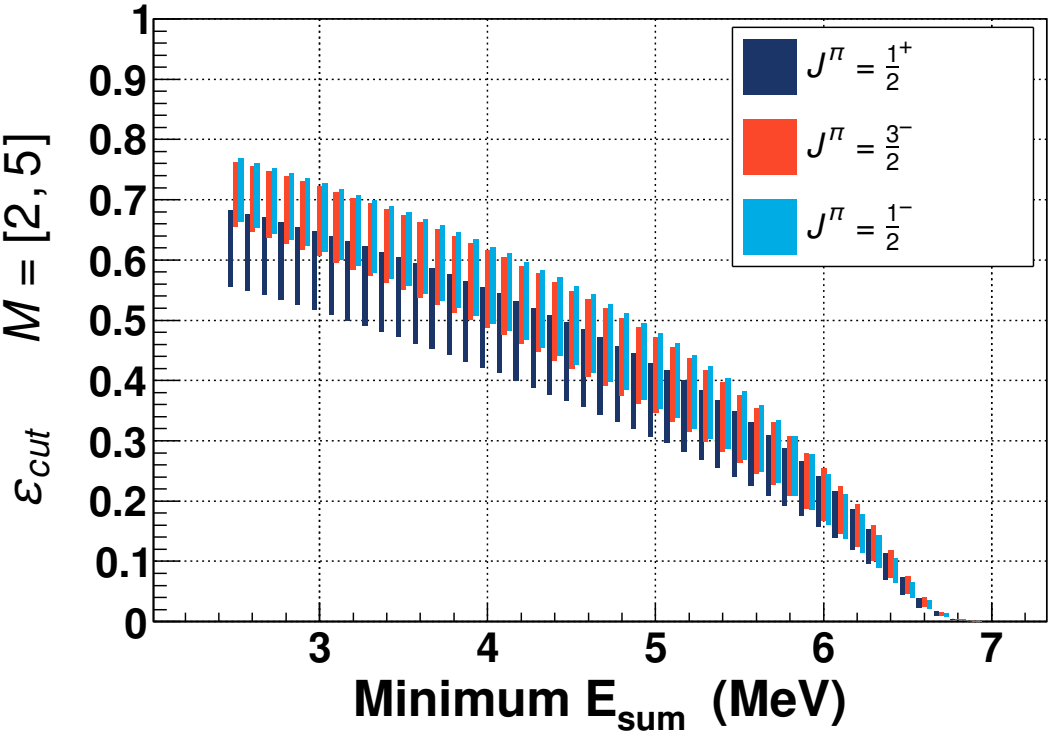

FIGURE 3.17: DICEBOX efficiencies for multiplicities as a function of lower E_{sum} gate boundary $M = [2, 5]$ and $E_{sum} <$ 7.0 MeV. The minimum E_{sum} was varied starting at 2.5 MeV and was increased in 100 keV steps (vertical bars are artificially offset for visualization)

The statistical cascades from DICEBOX were then used as an input to a detector response simulation modeled using the Geant4 toolkit [64]. In order to validate the DICEBOX+Geant4 simulations, the total energy distributions and Multi-Step Cascade (MSC) spectra were used to compare the data to the simulations. MSC spectra are the energy spectra of individual gamma rays (Cluster Energies E_γ) for a given multiplicity gated on the neutron energy of an individual capture resonance and E_{sum} gate on the reaction Q-value. The spectra produced from the simulations were subject to the same conditions applied to the analysis of the zinc data. See

Appendix 7.2 for a comparison of an ensemble of simulations to DANCE data on several strong resonances.

TABLE 3.3: DICEBOX efficiencies ($M = [2,5]$, 3.5 MeV $> E_{sum} >$ 7 MeV) for different spin parities calculated for 150000 gamma ray cascade simulations on fifteen artificial nuclei.

#	$J^\pi = \frac{1}{2}^+$	$J^\pi = \frac{1}{2}^-$	$J^\pi = \frac{3}{2}^-$
1	0.53(2)	0.60(5)	0.57(8)
2	0.43(2)	0.63(5)	0.62(7)
3	0.62(6)	0.59(0)	0.61(8)
4	0.37(0)	0.63(0)	0.64(2)
5	0.43(7)	0.59(2)	0.62(9)
6	0.54(8)	0.55(7)	0.60(6)
7	0.39(1)	0.63(7)	0.62(8)
8	0.58(7)	0.60(9)	0.61(5)
9	0.58(9)	0.61(7)	0.63(7)
10	0.45(5)	0.62(4)	0.55(2)
11	0.59(4)	0.63(9)	0.62(9)
12	0.63(1)	0.63(6)	0.63(5)
13	0.63(6)	0.56(5)	0.63(7)
14	0.62(4)	0.60(9)	0.61(7)
15	0.61(5)	0.63(1)	0.61(3)

For multiplicities $M = [2,5]$, the effect on the efficiency of the lower E_{sum} gate boundary was investigated. A much larger efficiency difference between $J^\pi = \frac{1}{2}^+, \frac{1}{2}^-, \frac{3}{2}^-$ spin-parities was seen when only multiplicity $M = [3,5]$ were included emphasizing the importance of including M=2 events. The vertical bars in the efficiency plot shown in Figure 3.17 represent the efficiency average and standard deviation of 15 nuclear realizations for each spin-parity. The lower E_{sum} boundary of 3.5 MeV was chosen as a compromise between minimizing the resulting uncertainty in the efficiency and maintaining confidence in the background subtraction at low E_{sum} energies. The efficiencies calculated from the simulations are shown

in Table 3.3 for this chosen E_{sum} range and multiplicities 2 to 5. Taking a global average over all simulations, an average of efficiency of 0.59 was adopted with a systematic uncertainty of 20%. Averaging over nuclear realizations provides an efficiency that can be interpreted as an average efficiency over several neutron capture resonances. These simulations predict less dependence on spin-parity if single multiplicities are included, and preliminary background subtractions in the zinc experiment show promising single multiplicity data. This could provide a venue for further reducing the efficiency uncertainty that is a dominant source of systematic error. However, the variation in the gamma cascades for different neutron energies in the zinc data will ultimately produce an irreducible uncertainty in the cross section.

Chapter 4
Cross Section Results

Using the results from Chapter 3, the ^{68}Zn(n,γ) cross section was calculated using,

$$\sigma_{n\gamma}(E_n) = \frac{1}{\varepsilon_{cut}} \frac{Y^{68}_{n\gamma}(E_n)}{N_{68}} \underbrace{\left(\frac{\sigma_{BM}}{\kappa f_a(E_n) Y_{BM}(E_n)} \right)}_{\Phi^{-1}_{BM}} \tag{4.1}$$

where ε_{cut} is the cut efficiency determined by DICEBOX; $Y^{68}_{n\gamma}(E_n)$ is the background subtracted yield (counts); N_{68} is the number of ^{68}Zn atoms in the target; and Φ_{BM} is the normalized neutron flux (neutrons/barn) determined from the beam monitors. Figure 4.1 shows the cross section from this work. The statistical uncertainty for each neutron energy bin is the result of independently propagated errors from the neutron flux and background subtraction. The flux errors were calculated assuming poisson statistics for the neutron flux monitors, and the errors in the background subtracted yield were calculated using the SVD method. The statistical errors increase with energy, since both the flux and the cross section are decreasing.

We also compare our result to the most recent evaluated cross section by Iwamoto. Below 100 keV the resonance parameters from Iwamoto were used to produce a resolution broadened cross section using the R-matrix code SAMMY [65, 6, 46, 47]. Above 100 keV, in the unresolved resonance region, the cross section is based on a coupled-channels optical model calculation fit to measured data up to 3 MeV [6]. At this point, the uncertainty in the current measurement is dominated by a systematic error in the efficiency of detecting a gamma-ray cascade following neutron capture. Further simulation studies of the detector efficiency, and including single multiplicity data could reduce this uncertainty. The next largest uncertainty

is the 4% systematic error in the gold target thickness determined by Rutherford back-scattering sets a lower limit on the obtainable uncertainty. Other sources of systematic error from the number of ^{68}Zn atoms and the attenuation correction factor are negligible.

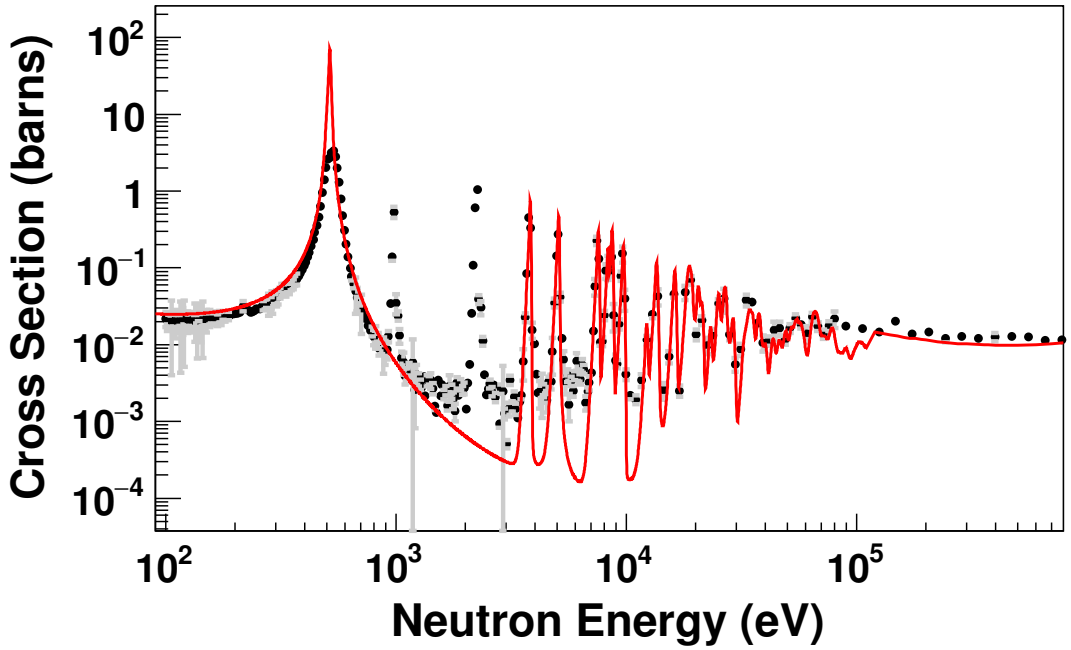

FIGURE 4.1: The ^{68}Zn(n,γ) cross section from this work is shown in black with statistical error bars with a comparison to the current recommended cross section in red [6, 5].

Due to the large cross section and target thickness, the peak of the 516 eV resonance shows a saturation effect in the measured yield. However, this resonance has a small impact on the Maxwellian-Averaged Cross Sections for kT$>$ 20 keV. However, the effect of this saturated resonance could become more important once other sources of error are reduced. Large discrepancies are seen at neutron energies of 0.98 keV and 2.2 keV corresponding to missing resonances in the ^{68}Zn(n,γ) evaluated cross section (See Figure 4.2). A resonance at 983 eV was originally seen in the Garg *et al.* experiment and was preliminarily reported to Mughabghab by

private communication as a p-wave resonance with no spin assignment or gamma width [66], and later this resonance was omitted in the published resonance parameters [42]. Iwamoto noted a significant discrepancy at 2.245 keV in the description

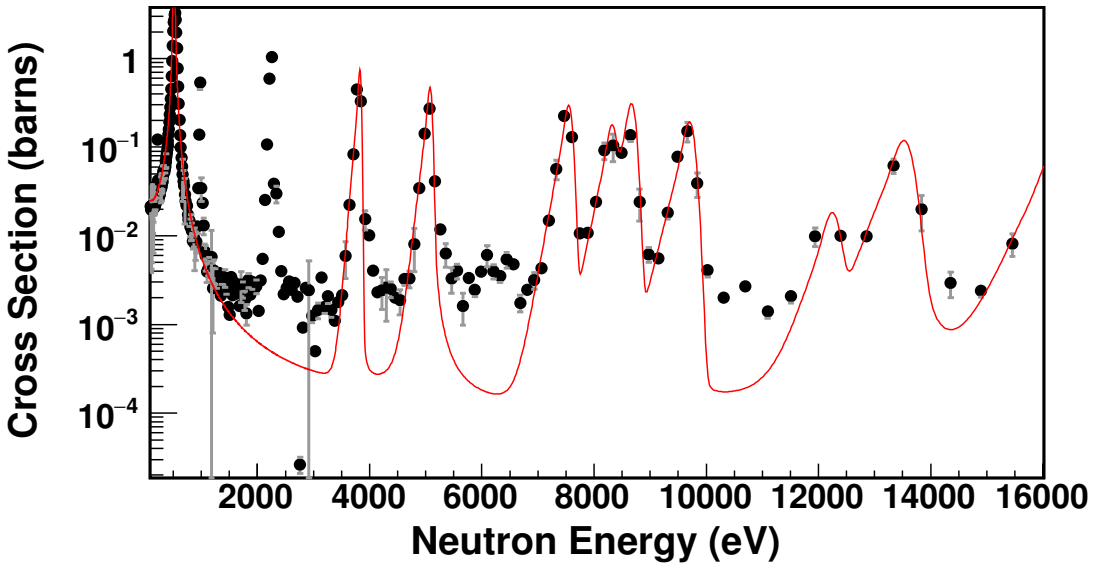

FIGURE 4.2: The ^{68}Zn(n,γ) cross section from 1 keV-16 keV compared the current recommended cross section [6, 5].

of the elemental capture cross section and attributed this discrepancy to resonance parameters for ^{67}Zn. Previous experimental techniques would have had difficulty in resolving this ^{68}Zn state in the midst of several resonances in ^{67}Zn, especially in elemental capture data. Since DANCE is a calorimeter, it provides clear discrimination of different isotopic contributions (see Figure 3.15). The cross section shown in Figure 4.2 at 8.5 keV is a factor of two lower than the evaluated cross section. This particular resonance appears very strongly in the single multiplicity $M = 1$ data explaining the reduced yield for $M = [2, 5]$.

Another significant deviation from the evaluated cross section is at higher energy, shown in Figure 4.3(a), for the 20.23 keV resonance reported by [42]. It is a possibility that a contribution from resonant neutron scattering in this energy region,

apparent in Figure 4.3(b), could be misidentified as capture yield in the previous work. It is important to note that the extra flightpath length of the scattered neu-

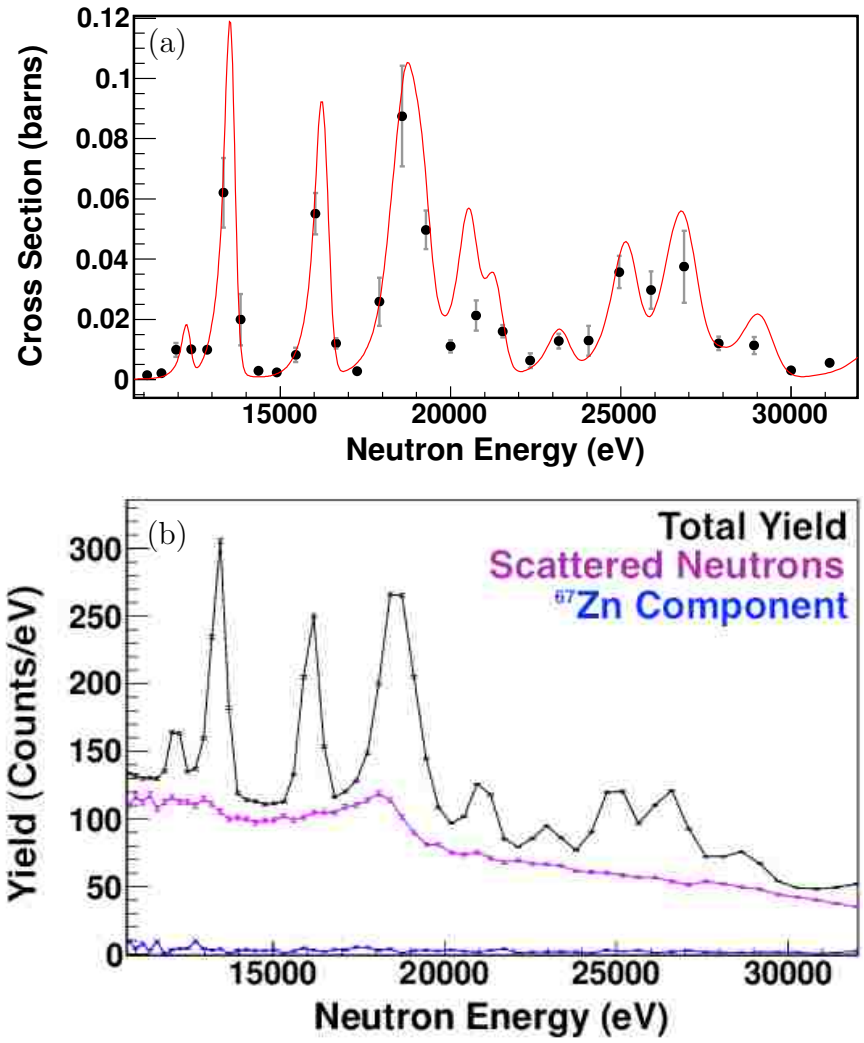

FIGURE 4.3: (a) The ^{68}Zn(n,γ) cross section compared the current recommended cross section [6, 5]. (b) The background characterization near 20 keV. It is important to note that there is an unaccounted for energy shift in the scattered neutron component.

tron would correspond to a shift in the calculated energy in both this experiment and the previous experiment. The neutron energy resolution in this region cannot rule out a capture resonance at this energy; however, additional analysis could provide a constraint on the gamma width (Γ_γ). The ability to distinguish scattered

neutron backgrounds from capture events is one of the advantages calorimeters such as DANCE have over previous experimental techniques.

The Maxwellian-Averaged Cross Sections (MACS) were calculated using Equation 4.2 as a sum over the binned cross section shown in Figure 4.1.

$$\begin{aligned}\langle \sigma v \rangle &= \frac{2}{\sqrt{\pi}} \frac{1}{(kT)^2} \int_0^\infty \sigma(E_n) E_n e^{-E_n/kT} \mathrm{d}E_n \\ &\simeq \frac{2}{\sqrt{\pi}} \frac{1}{(kT)^2} \sum_a^b \sigma_{E_n} E_n e^{-E_n/kT} \delta E_n \end{aligned} \tag{4.2}$$

The calculated MACS are shown in Table 4.1 with statistical uncertainties compared to values reported in the Karlsruhe Astrophysical Database of Nucleosynthesis in Stars (KADoNiS) [11] and the National Nuclear Data Center (NNDC) [5, 67]. An additional systematic uncertainty of 20% is associated with the results from this work from the efficiency as previously discussed. The MACS reported in KADoNiSv0.3 were calculated from the experimental data from Garg *et al.* [42], and the MACS calculated from ENDFVII.1/B is based on the work by Iwamoto [6, 67]. The MACS from this work favor the values from the new recommended ENDFVII.1/B MACS partly due to the agreement at higher energies between this work and the

TABLE 4.1: Maxwellian-Averaged Cross Sections (MACS) for a range of energies (kT from 20 keV to 100 keV) from this work compared to recommended values.

kT [keV]	This work $\langle \sigma v \rangle \pm \sigma^{(\mathrm{stat.})}$[mb]	NNDC [67] $\langle \sigma v \rangle$ [mb]	KADoNiS0.3[11] $\langle \sigma v \rangle$ [mb]
20	24.6 ± 0.6	25.4	26
25	22.9 ± 0.5	22.6	22
30	21.7 ± 0.4	20.7± 2.6	19.2±2.4
40	19.9 ± 0.3	18.4	16
50	18.7 ± 0.3	17.0	14
60	17.7 ± 0.2	16.1	13
70	16.9 ± 0.2	15.3	–
80	16.3 ± 0.2	14.8	12
90	15.7 ± 0.2	14.4	–
100	15.3 ± 0.2	14.1	11

model-driven calculated cross section of Iwamoto that included higher energy neutron capture data and additional channels resulting in an enhanced cross section at high energy [6].

As an outlook for continued work, the data from this experiment can further constrain the uncertainties on both ^{67}Zn(n,γ) and ^{68}Zn(n,γ). This DANCE data for ^{67}Zn(n,γ) could potentially have a substantial impact considering the 30% reduction in the 30 keV MACs by Iwamoto compared to the work by [41]. Preliminary

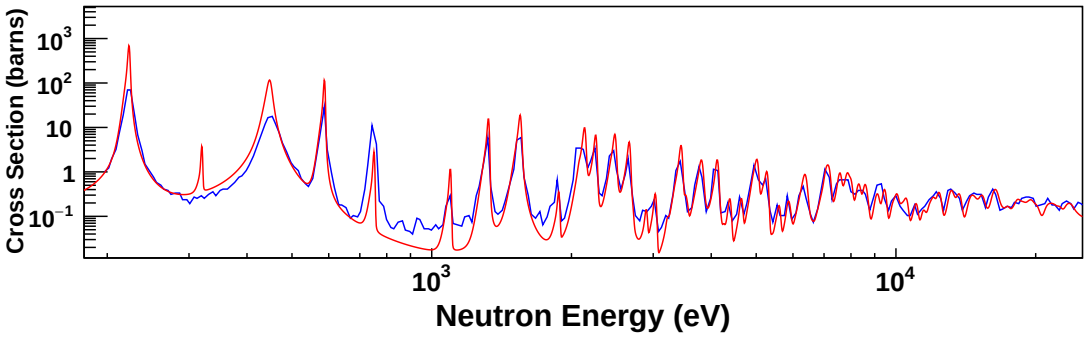

FIGURE 4.4: Preliminary ^{67}Zn cross section comparison. The data from this work is shown in blue, and the red line corresponds to the work by Iwamoto [6]. The absolute normalization of the data is arbitrarily scaled for comparison.

data shown in Figure 4.4 of the ^{67}Zn(n,γ) cross section looks promising; however, more work is required to extract the final cross section results. Even the ^{68}Zn target analysis reveals a resonance at 320 eV due to ^{66}Zn(n,γ) has been previously attributed to ^{67}Zn, and the ^{67}Zn can further improve the data on the $^{66-68}$Zn region. Having a significantly different Q-value (10.2 MeV), the background suppression for the ^{67}Zn target is much different than outlined in §3.5. The preliminary cross section for ^{67}Zn(n,γ) (with arbitrary absolute normalization) was produced by placing a narrow total energy gate ($E_{sum} > 10$ MeV) to select clean events above the highest energy barium capture resonance.

Chapter 5
ANASEN Motivation

The Array for Nuclear Astrophysics and Structure with Exotic Nuclei (ANASEN) is an instrument being developed to study charged-particle reactions using beams of radioactive nuclei that are important in stellar explosions. Measurements on proton-rich nuclei particularly in the region of ^{56}Ni are important for supernova ejecta where the νp process is a possible scenario for the Light Element Primary Process [31]. Reactions on proton-rich nuclei are also important for nucleosynthesis and energy generation in Type I X-ray bursts, where a sequence of proton capture reactions (rp process) occur similar to that of the νp-process. A major difference is that the νp-process starts with the iron group nuclei initially produced in a quasi-statistical equilibrium [31], and the rp process starts with nuclei formed from the triple-α and the αp process [68].

Type I X-ray bursts are the most common stellar explosions in the Galaxy and result from thermonuclear explosions on the surface of accreting neutron stars in binary systems. In such cases, a neutron star accretes hydrogen and helium rich material from the envelope of a companion star. Nuclear reactions produce energy on the surface, but due to the neutron star degeneracy, the temperature and density increase rapidly burning hydrogen in the hot CNO cycles. Helium accumulates on the surface of the neutron star until the triple-alpha reaction ignites thermonuclear runaway with a series of (α,p) and (p,γ) reactions, known as the αp-process, and eventually the rapid proton capture (rp) process [69]. The sequence of reactions that occurs, illustrated in Figure 5.1, potentially synthesizes nuclei as heavy as A=100. The study of these events can help us to understand the structure and

evolution of neutron stars in binary systems, but our understanding is limited in large part by a lack of nuclear data regarding charged particle reactions on radioactive isotopes that play a key role in the explosions.

Due to the intense gravitational field, Type I X-ray bursts are not expected to eject matter or contribute to the chemical evolution of the Galaxy; however, the isotopic abundances produced can have a substantial effect on the evolution of the host system and are important for understanding observations. Few of the important nuclear reactions have been previously studied, and new reaction measurements are required to accurately model the bursts and study neutron star systems [70]. New techniques like ANASEN allow measurements key reactions important for these systems with radioactive beams of relevant proton rich nuclei.

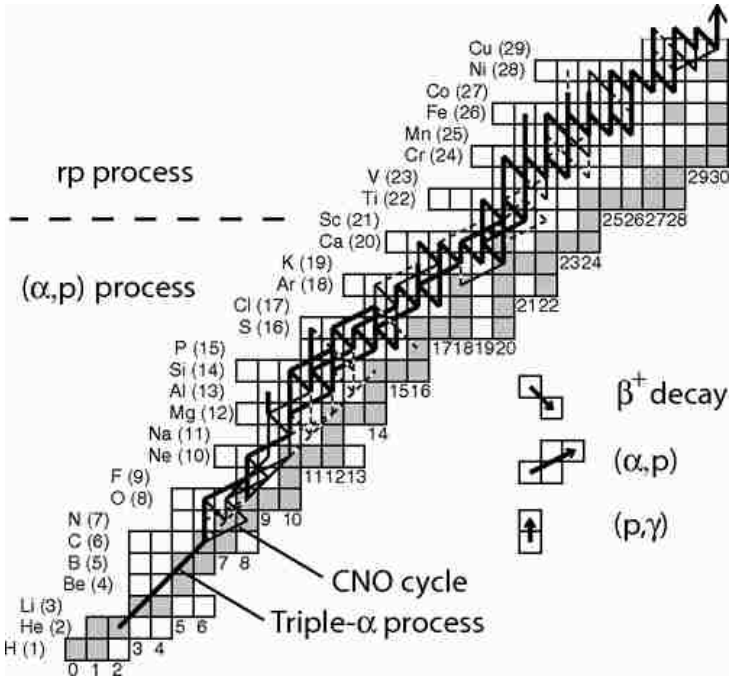

FIGURE 5.1: Figure from Matic *et al* illustrating the nuclear reactions that occur in Type I X-ray bursts [7]

Reaction network sensitivity studies have identified key reaction rates significantly affecting both energy generation and final elemental abundances in Type I

X-ray bursts [70]. Many of the reactions these studies have identified are α-induced reactions with low Q-values and weak reaction rates that limit energy production and stall nucleosynthesis in X-ray bursts. Recent state-of-the-art, multi-zone hydrodynamical simulations in particular identified (α, p) reactions on ^{14}O, ^{18}Ne, ^{22}Mg, and ^{56}Ni as being most important [71].

One of these reactions, $^{18}\mathrm{Ne}(\alpha, p)^{21}\mathrm{Na}$, governs breakout of the hot CNO cycles [68]. Because of its importance, $^{18}\mathrm{Ne}(\alpha, p)^{21}\mathrm{Na}$ has had the most experimental investigation [8]. Figure 5.2 shows the tension between different information on the cross section of interest. Two measurements of the time-inverse reaction $^{21}\mathrm{Na}(p, \alpha)^{18}\mathrm{Ne}$ have been measured (data points shown in Figure 5.2) [72]; however, such studies do not provide significant constraints on (α, p) reactions to excited states in the final nucleus, which likely provide the dominant contributions to the reaction rate [8]. Nuclear structure information from transfer reaction measurements by Matic *et al.* and others have been used to infer the reaction rate [73, 8]. Groombridge *et al.* performed a direct measurement on an extended helium gas target [74]; however, the results from that experiment have yet to be fully understood in the context of other available information on the reaction rate. Mohr *et al.* compares the all of the available information on the reaction rate, supplemented by additional information from the mirror nucleus, but the discrepancies with the time-inverse reactions are still uncertain [8]. While substantial uncertainties remain, what has been learned thus far experimentally does not agree well with statistical model estimates that form the basis of rates used in astrophysical models. Thus, it is important to measure these (α, p) reactions directly and precisely in the astrophysically relevant energy ranges.

The principle challenge in directly measuring (α, p) reactions is to construct a thick helium gas target to achieve high reaction yields while maintaining adequate

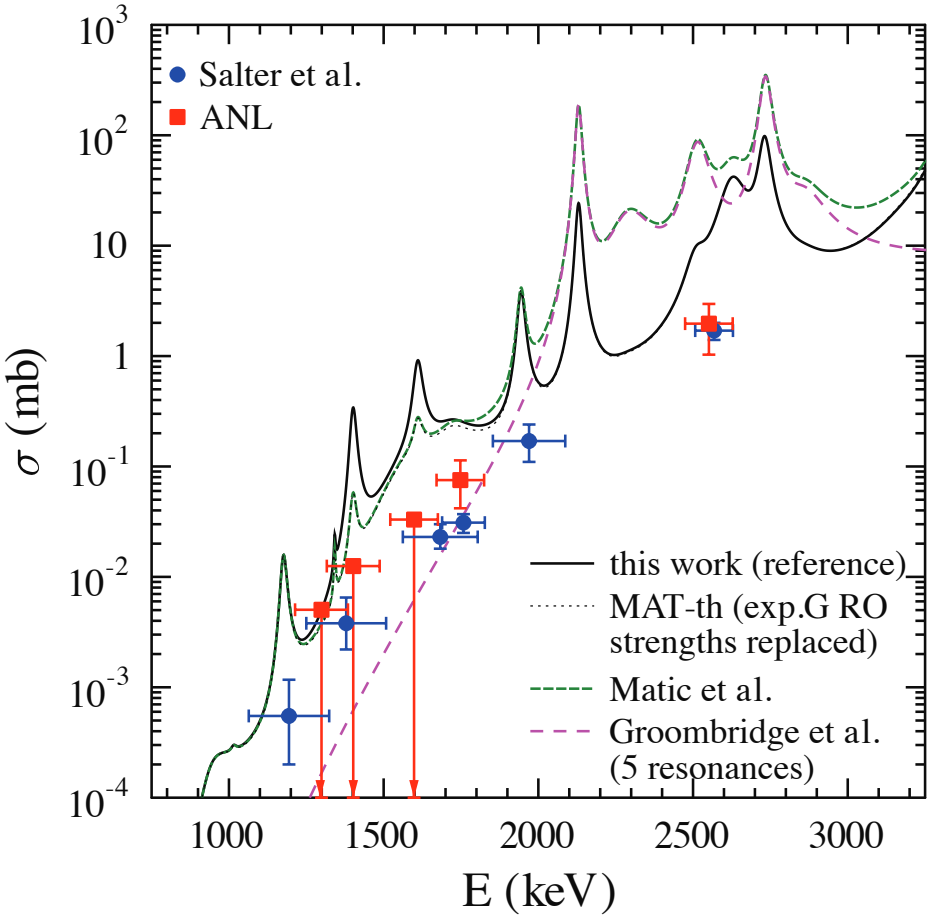

FIGURE 5.2: Comparison of available data in a study by *Mohr et al* [8]

resolution. Previous thick helium target measurements have typically used telescopes of silicon detectors operating in an extended gas volume, with limited solid angle coverage, target thickness, and resolution [74]. Tracking detectors and active gas targets are becoming increasingly more important in the push to study more exotic short-lived isotopes.

The LSU-FSU Array for Nuclear Astrophysics and Structure with Exotic Nuclei (ANASEN) is a charged particle detector array designed to measure these reactions using radioactive ion beams from the John D. Fox Superconducting Accelerator Laboratory at FSU and at the new ReA3 facility at the National Superconducting Cyclotron Laboratory (NSCL). ANASEN is designed in part for direct measure-

ments of (α, p) reactions with maximum sensitivity, allowing measurements with radioactive ion beam intensities of as little as 10^5 ions/s. The ReA3 facility at the NSCL also promises to provide nuclei that are important in the αp process that ignites X-ray bursts with sufficient intensities for direct (α, p) reaction studies using a sensitive instrument like ANASEN. This program promises to provide a broad basis in range of energies and isotopes that is needed to put our understanding of the αp process on a firm experimental footing.

Chapter 6
ANASEN: Active Gas Target Mode

An integral part of ANASEN is an *Active Gas Target* (AGT) capability where gas is used both as target and as part of a detector system to achieve detection efficiency over a broad range of angles while maintaining good energy resolution. The ANASEN AGT configuration is comprised of two essential components: 1) a large area array of double-sided silicon strip detectors (DSSDs): (Micron Semiconductor Super X3 and QQQ3) [75] backed by Scionix CsI(Tl) scintillators [76], and 2) a high-gain position-sensitive Multi-Anode Proportional Counter (MAPC). The event-by-event reconstruction using the DSSDs and the MAPC improves the resolution achievable with a thick target as the incident beam produces reactions in the target over a range of energies. This allows the entire excitation function to be measured simultaneously as the beam loses energy as a function of target depth. The use of AGTs will become extremely important for the study of new exotic beams that will be provided by ReA3 facility at MSU and the Facility for Rare Isotope Beams which is currently under construction.

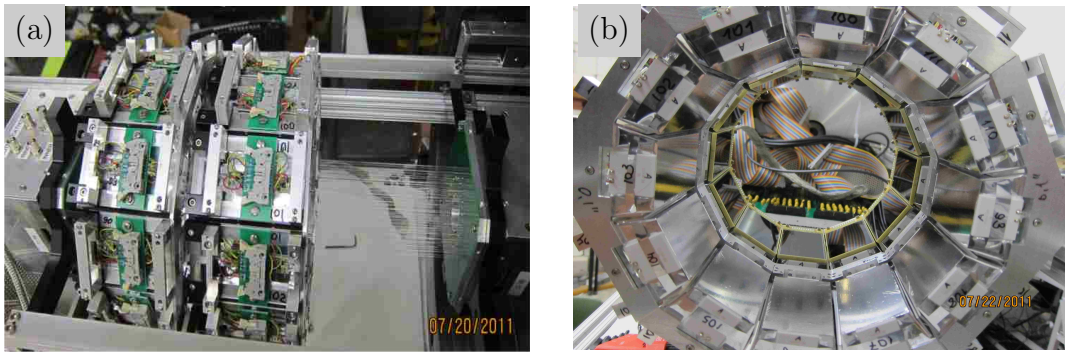

FIGURE 6.1: Photo of Initial Implementation of ANASEN. (a) Two rings of Super X3s-CsI Rings Installed around MAPC. (b) Beam View of ANASEN with one ring of Super X3s and the MAPC removed.

The initial implementation of ANASEN, shown in Figure 6.1, used a MAPC constructed with 19 anode wires in a barrel geometry at a radius of 3 cm from the center of the beam axis (z-axis). The MAPC measures energy deposited in a 1 cm diameter region around each anode wire, and provides the position of reaction products at one point close to the beam axis. A surrounding array of silicon detectors backed with CsI scintillators provide position and full energy reconstruction [9]. Furthermore, the energy signals from the DSSDs and MAPC together allow discrimination between particle species (protons, deuterons, tritons, ^{4}He, ^{6}He) described in §6.4.3, and the two position measurements enable the track reconstruction in §6.4.1. The excitation function can be determined through energy-loss calculations described in §6.4.2 and kinematics calculations described in §6.4.4 and §6.4.5.

6.1 ^{14}N$(\alpha, p)^{17}$O Commissioning Experiment

The reaction, ^{14}N$(\alpha, p)^{17}$O, was measured as an initial proof-of-principle test case of the AGT mode of ANASEN to study the detector performance. This reaction has been extensively studied with α beams on nitrogen targets [10], and has a historical significance of being the first nuclear reaction ever recorded [77]. The ^{14}N$(\alpha, p)^{17}$O excitation function has a number of clearly identifiable resonances that can be used to characterize the energy resolution of the spectra obtained with ANASEN. This test case reaction also has a very similar kinematic behavior to (α, p) reactions of interest for initial ANASEN experiments: ^{14}O$(\alpha, p)^{17}$F and ^{18}Ne$(\alpha, p)^{21}$Na. Furthermore, a benchmark for determining excited state contributions to reaction rates is provided by the rather large, 870 keV, separation between the ground state and the first-excited state in ^{17}O.

For this stable beam test, a ^{14}N beam was produced by the FSU FN pellotron tandem Van de Graf accelerator at 30 MeV. The beam quality (energy resolution,

spot size, and emittance) is unmatched by other types of accelerators. A nominal beam intensity of 10^6 ions/s was used for this test providing ample statistics in only six hours of data collection. Care was taken to limit the beam rate, since high beam particle rates are detrimental to the MAPC performance.

Various gas mixtures were tested during the experiment, and a preliminary analysis was performed online to select a gas mixture for this test. The data presented here was taken with the detector filled with 350 Torr helium 1% CO_2 admixture. The bias voltage on the detector was set to 650 Volts corresponding to approximately 50 Volts below the onset of breakdown. The presence of breakdown was prevented by careful monitoring of the MAPC signals and the bias supply current. Because the detector has a large series resistance of over 200 MΩ, bias supply currents as low as 0.1 μA are symptoms of breakdown within the detector. During this experiment, the detector gas was mixed in the chamber and valved off requiring periodic flushing and refilling the detector.

6.2 Silicon Array

The DSSDs are electrically segmented into perpendicular strips (see Figure 6.2). When a particle deposits energy in the silicon, signals are induced on orthogonal strips on the front and back sides of the detector. Correlating events between the two sides of the detector partitions detected events into *quasi pixels*. This capability is utilized in the energy and position calibrations. The Super X3s were designed with a uniform resistive layer on the front side resulting in an upstream U_i and downstream D_i signal from the two edges of each front strip i [78]. The Super X3s are oriented with the front strips running parallel to the beam axis (z-axis). See Figure 6.2 for schematics of the silicon detector geometries. A precise position ($\delta z \approx 1.5$ mm) is determined by the *resistive charge-division method* between the upstream and downstream ends [53].

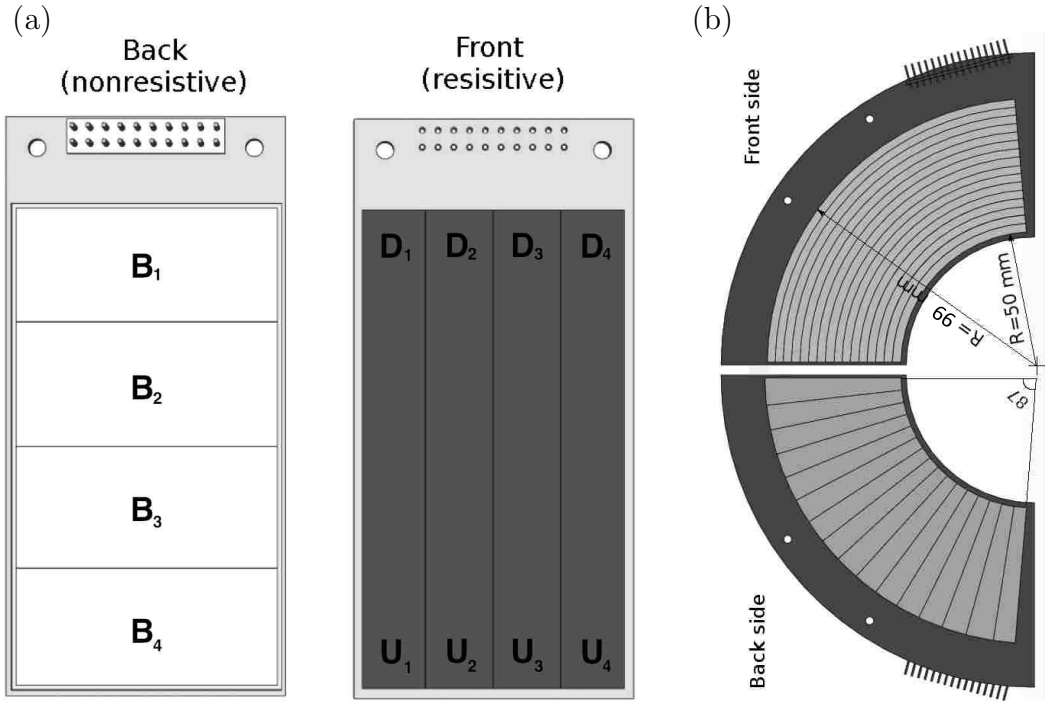

FIGURE 6.2: Sketches of the Micron Semiconductor Super X3 (a) and QQQ3 (b) illustrate the perpendicular segments in each detector type.

6.2.1 Silicon Energy Calibration

The first stage of the calibration is an offset pedestal subtraction. A well calibrated pulser is used to determine the zero voltage offset (or pedestal) (p_i) for each channel of the electronics. The pedestal should correspond to the detector zero point energy; however, incomplete charge collection, ballistic deficit and crosstalk can contribute to a small shift to the energy offset of about 100 keV. After subtracting the pedestal from the pulser calibration, a linear energy calibration (with a gain g_i and energy offset o_i) is then applied for each channel of the silicon detectors. The pedestal subtraction is done for all silicon signals and is implied in the rest of this section. The pedestal offset p_i can be absorbed into the detector offset, but it is extremely useful for the Super X3 position to constrain the relative offsets between two ends of the same front strip (See §6.2.2).

An additional, sixty-four calibration parameters are needed for the QQQ3 detectors and twenty-four for the Super X3s. By selecting events when one pair of perpendicular strips registers, a full relative energy calibration of the QQQ3 strip detectors can be determined *in situ* for the data of interest directly and automatically using the following relationship:

$$\begin{aligned} E &= g_i^{(f)} F_i + o_i^{(f)} \\ &= g_j^{(b)} B_j + o_j^{(b)} \\ \Rightarrow g_j^{(b)} B_j - g_i^{(f)} F_i + o_j^{(b)} - o_i^{(f)} &= 0 \end{aligned}$$

Each of the sixteen QQQ3 front signals F_i can be matched to each of the 16 back segments B_j by a variety of linear fitting methods to provide 62 out of the 64 needed parameters. Then a single energy calibration with a source of known energy can be applied to the entire detector.

Similarly for the SuperX3, after subtracting the voltage offset, each pair of front signals U_i and D_i are coincident with each back signal B_j providing a relation that is useful for calibration.

$$\begin{aligned} E = E_i^{(u)} + E_i^{(d)} &= \underbrace{g_i^{(u)} U_i + o_i^{(u)}}_{E_i^{(u)}} + \underbrace{g_i^{(d)} D_i + o_i^{(d)}}_{E_i^{(d)}} \\ = E_j^{(b)} &= g_j^{(b)} B_j + o_j^{(b)} \\ \Rightarrow g_j^{(b)} B_j - g_i^{(u)} U_i - g_i^{(d)} D_i + o_j^{(b)} - \left(o_i^{(u)} + o_i^{(d)} \right) &= 0 \end{aligned} \tag{6.1}$$

Since the front offsets $o_i^{(u)}$ and $o_i^{(d)}$ only appear as a sum in Equation 6.1, they cannot be determined individually by energy calibration alone. These offsets play an important role in the position calculation.

6.2.2 Super X3 Position

It is *vital* to perform proper energy calibrations before considering the detector position. The gains $g^{(u)}$ and $g^{(d)}$ are determined by the energy calibration while

the individual offsets $o^{(u)}$ and $o^{(d)}$ are still undetermined. However, the offsets can be constrained to within 100 keV by a precise pulser calibration. In this case, the energy calibration constraint on the sum of the offsets can be used as an approximation $o^{(u)} \simeq o^{(d)} \simeq (o^{(u)} + o^{(d)})/2$ which is approximately 5% of the electronics threshold. The position along the length of the detector $Z_{si}^{(det)}$ can then be calculated using,

$$\begin{aligned} Z_{si}^{(det)} &= (7.5cm)\,\frac{E^{(u)}}{E^{(b)}} = (7.5cm)\left(1 - \frac{E^{(d)}}{E^{(b)}}\right) \\ &= \left(\frac{7.5cm}{2}\right)\left(1 + \frac{E^{(u)} - E^{(d)}}{E^{(b)}}\right), \end{aligned} \tag{6.2}$$

depending on which front side signals are present. See Figure 6.3(a) for an example of the behavior of the Super X3 position when the energy calibration is neglected. The $\sim 1/E$ divergence in the position is due to the error introduced by not accounting for the offsets. In order to diagnose this error in position, it is very useful to use broad range of particle energies in the position calibration rather than a mono-energetic alpha source.

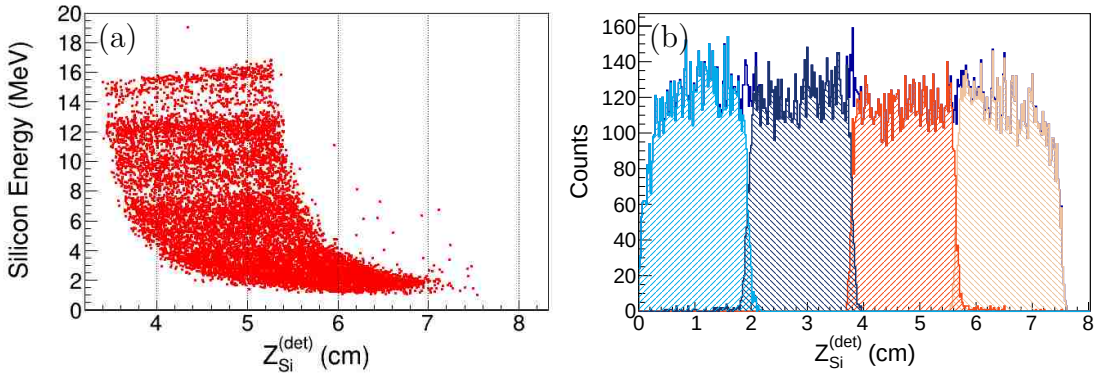

FIGURE 6.3: (a) SuperX3 "Position" vs. Energy for a single *quasi pixel* without an energy calibration. (b) SuperX3 Position for a single front strip gated on the four back segments.

Finally, as illustrated in Figure 6.3(b) the position can be validated and refined using the five known positions of the back strip borders (Each back strip is of equal

width of 1.875 cm) by correlating the front side position with the back channel that fired. For each back segment, the position at half maximum amplitude of the front side position distribution is constrained to the known location of the back segment border. Care must be taken at the edges of the detector to choose the correct form of Equation 6.2 when using the outer border of the detector as a constraint. If a large dataset is available an alternative method to define the edge of the strips selects *border hits* that share energy between two adjacent back segments [9]. This method usually requires stable beam intensities and either long runtimes or undesirable high rates on the silicon detectors. The position within the silicon detector can be transformed into world coordinates using the measured locations of the detectors within the array.

6.3 Proportional Counter

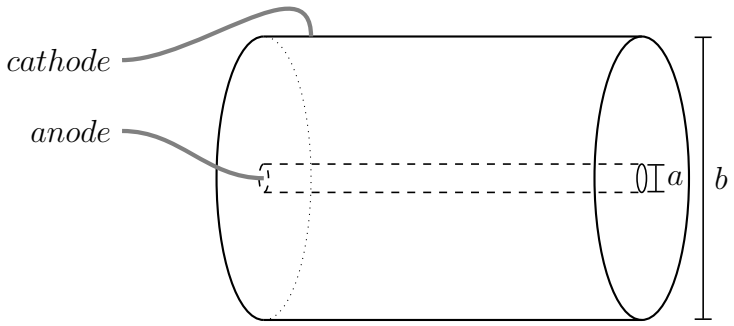

FIGURE 6.4: Single anode cylindrical proportional counter

The typical geometry of a proportional counter, shown in Figure 6.4, is a gas-filled cylindrical cathode tube with a thin anode wire with bias voltage $+V$ along the central axis. In this geometry, the electric field inside the detector is given by,

$$\mathcal{E}(r) = \frac{V}{r \ln(b/a)} \tag{6.3}$$

Electrons and ions produced by ionization of the detector gas drift towards the anode and cathode respectively. Away from the anode, the mean free path between

collisions with the detector gas prevents substantial acceleration of the charges. Near the anode wire, the electric field is sufficiently high that, within one mean free path, electrons can gain enough energy to ionize the detector gas resulting in a proportional increase in the number of charge carriers, n, with distance [53].

$$\frac{dn}{dx} = \alpha(\mathcal{E})n \tag{6.4}$$

The multiplication M of the number of charge carriers in a process known as a *Townsend Avalanche* depends upon the gas species, applied voltage V, and the gas pressure P. The *Townsend coefficient* α is zero below a minimum electric field $\mathcal{E}_{min}$ and increases monotonically throughout the operational range of the detector.

Making the approximation of a linear increase in Townsend Coefficient with electric field strength, the multiplication is parameterized by the *Diethorn Equation*,

$$\ln M = \frac{V}{\ln(b/a)} \frac{\ln 2}{\Delta V} \left(\ln \frac{V}{Pa \ln(b/a)} - \ln K \right), \tag{6.5}$$

where ΔV and $K = \mathcal{E}_{min}/P$ are a constant for a given gas mixture [79]. Neglecting the logarithmic term in Equation 6.5, the gas gain of the proportional counter should increase roughly exponentially with the bias voltage qualitatively describing the increase in signal size shown in Figure 6.5 [53].

The original design of the Multi-Anode Proportional Counter (MAPC) that is central to the ANASEN active gas target mode consists of 19 individual proportional counter regions. Operating at high multiplication is necessary for detecting protons because they lose a small amount of energy in the detector gas. The anode diameter limits the maximum electric field achievable for the detector for a given operating voltage, thus limiting the maximum multiplication. Each region is defined by a 7 μm diameter carbon fiber anode wire that is surrounded by eight 75 μm diameter gold plated tungsten wires that form the cathode (see Figure 6.6).

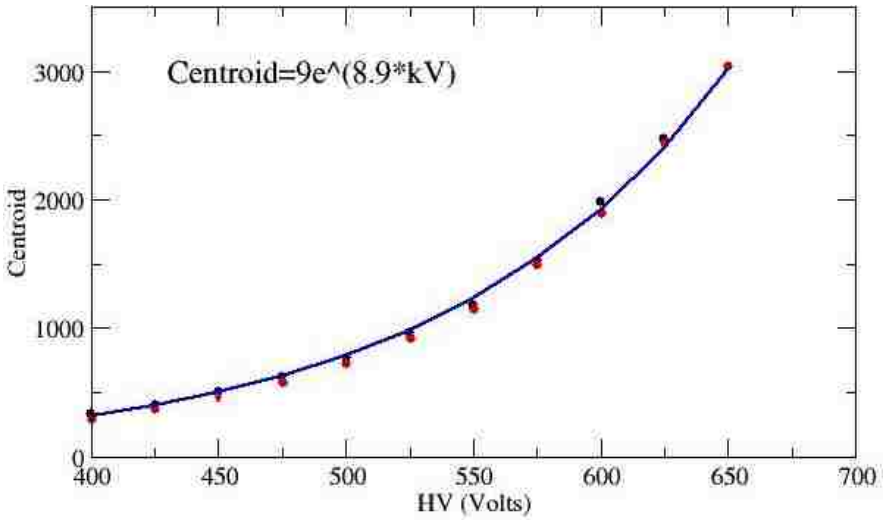

FIGURE 6.5: Plot showing the exponential increase signal size in ADC channels for an ^{241}Am alpha source.

Carbon fiber wire is the only material available that provides a reasonable mechanical strength for such a small diameter anode. Carbon is also the ideal material because it has a uniform, high resistance per unit length (≈ 2.7 kΩ/cm^2). Similar to the Super X3 postion (§6.2.2), this allows position information to be extracted using the resistive charge division method [9] discussed in §6.3.2.

A distance of three centimeters from the beam axis was chosen for the location of anode wires as a compromise to keep the anode wires far from, and insensitive to, the beam region while maintaining the ability to precisely reconstruct particle tracks described in §6.4.1. At this radius, segmentation into 19 proportional counter regions optimizes the cylindrical symmetry of the field near the wire (Figure 6.6). The detector was intentionally designed to be dead (no drifting of charges) near the axis because the beam and *beam-like* heavy recoils have higher Z and produce much more ionization than protons or alpha particles. Most importantly, the beam particle rate is much higher than the number of charge particles produced from nuclear reactions on the target gas.

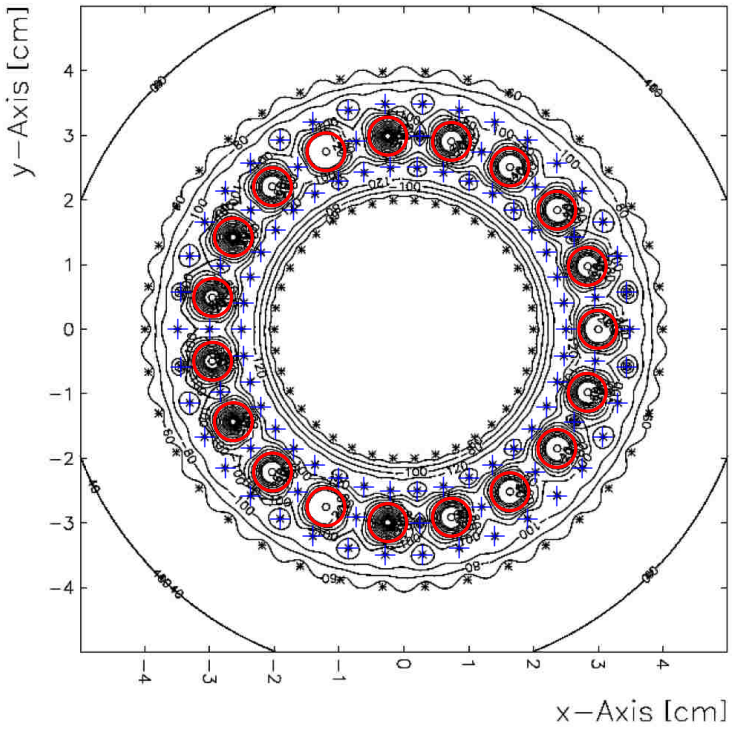

FIGURE 6.6: Cross-sectional view of equipotential contours from Garfield [9] for the proportional counter illustrating the 19 sensitive volumes segmented by the grounded cathode wires (marked in blue) having a cylindrical field in a region near the wire (highlighted in red).

Additional inner and outer guard rings were constructed with the purpose of field shaping and shielding the detector from charge produced near the beam axis; however, the effect of biasing these rings is quite complicated and has not yet been clearly demonstrated. A shift in the breakdown voltage of the detector occurs when biasing the guard rings indicating a change in the electric field near the anode wire. The influence of shaping wires or additional guard rings could be revisited for further study.

6.3.1 Pulser Calibration of the Preamplifier

The proportional counter was instrumented with a 64 channel Mesytec MPR-Log charge sensitive preamplifier [80]. This novel preamplifier is designed to have a gain that is approximately constant for low signal amplitudes while gradually

shifting to a lower gain for large signals (as illustrated in Figures 6.7 and 6.8). This allows a wide input range of charge to be measured with an acquisition system of limited dynamic range. The preamplifier signals were amplified and shaped into semi-gaussian pulses by a multi-channel shaping amplifier.

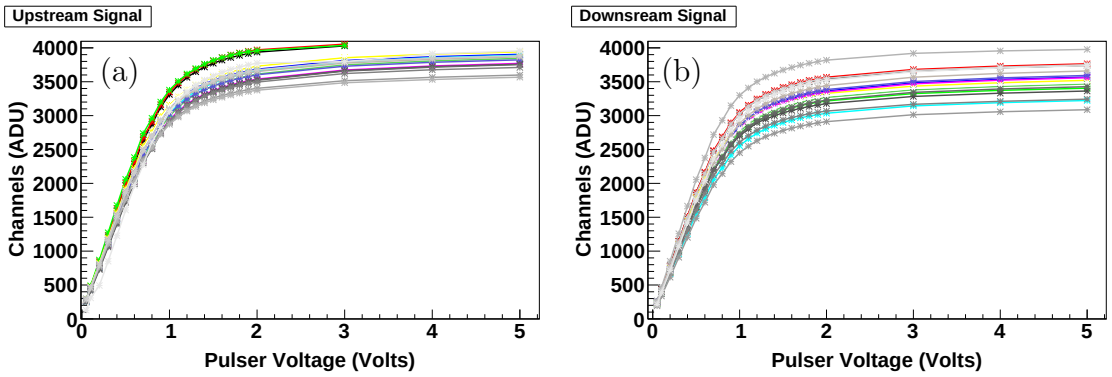

FIGURE 6.7: (a) Pulser calibration curves for the low gain setting for each of the 19 upstream channels. (b) Same as (a) for the downstream channels.

This complicated preamplifier response is clearly not linear, and although the response is described as logarithmic, it does not accurately follow a logarithmic function. In order to calibrate this preamplifier, it is necessary to perform multiple pulser measurements to build an interpolation table of the signal size measured by the ADCs versus pulser input voltage. When the electronic gain is increased,

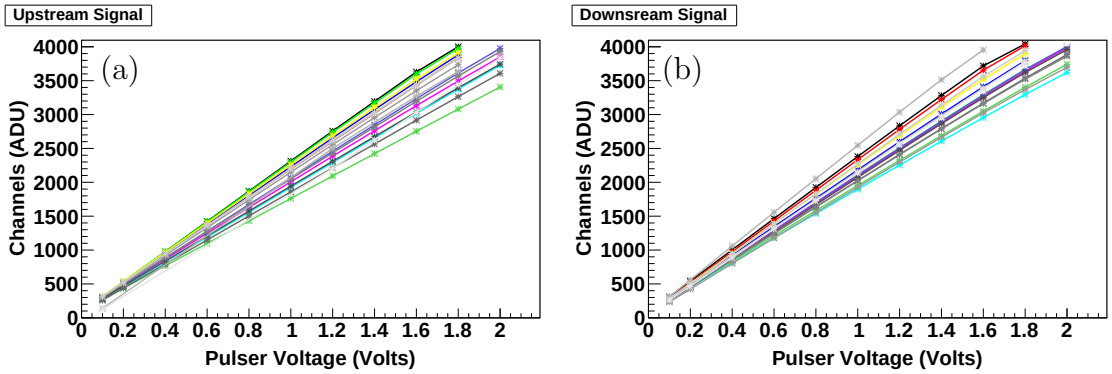

FIGURE 6.8: Same as Figure 6.7 using the high gain setting.

the low gain region is pushed off scale of the 12-bit peak-sensing ADCs and the

improved electronic dynamic range is not available. The resulting preamplifier response is approximately linear, yet a multipoint pulser calibration and interpolation is still needed to account for variations in the gain.

6.3.2 Proportional Counter Position

Once the proportional counter pulser calibration has been completed, Equation 6.6 is used to calculate the proportional counter position using the constants α and β determined for each individual wire by using a 5.3 MeV ^{210}Po alpha needle source that is inserted into the proportional counter at various depths along the beam axis.

$$Z_{PC} = \alpha \left(\frac{E_U - E_D}{E_U + E_D} \right) + \beta \tag{6.6}$$

In a variety of helium plus carbon-dioxide gas mixtures, the position of a similar 5.4 MeV ^{241}Am alpha source was used to determine the position resolution achievable. At sufficiently high bias voltages it is shown in Figure 6.9 that about 2 mm position resolution can be achieved. However, the measurements with helium gas were made at low pressure $P \approx 50$ Torr due to the limited range of the alpha particles.

Unlike the Super X3s, there is no independent full energy measurement and gain variations from the two ends of the same wire, resulting from the preamplifier channel-to-channel gain spread seen in Figures 6.7 and 6.8, are neglected in the position calculation. Also, the calibration from the alpha source is at a fixed energy, and the extrapolation of this calibration to the energy range of interest can be problematic especially when the response of the preamplifier is not linear over the full range of interest.

6.3.3 Sporadic Signals

In the detector fill gas, especially with helium, the excitation of atomic levels competes with the ionization process leading to the production of ultraviolet emis-

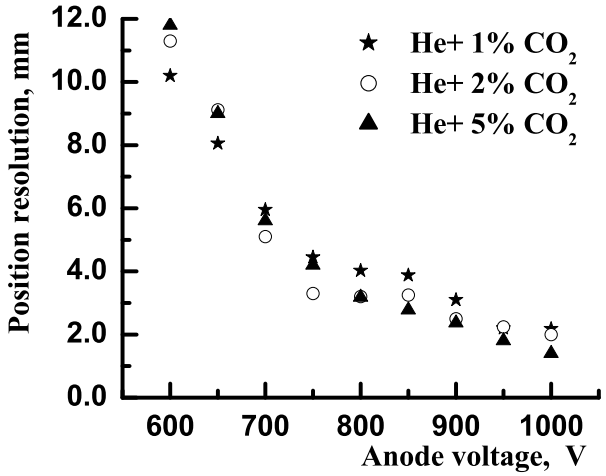

FIGURE 6.9: Proportional Counter Position Resolution in various helium carbon-dioxide gas mixtures for ^{241}Am needle source [9].

sion [53]. This is problematic for two reasons: 1) the excitation of the helium atom without the emission of an electron does not contribute directly to the detector signal, and 2) the emission of an ultraviolet photon can produce secondary ionization by the photoelectric effect resulting in spurious pulses throughout the detector volume. These effects are detrimental to both the position and energy determination from the measured signals. These sporadic signals have a negligible affect on the performance of proportional counters operating at low gas multiplications. In the regime of high multiplication where ANASEN operates, this can be extremely important. When the multiplication is increased to an extreme, the secondary pulses eventually lead to a saturation of charge within the detector. This is the operating principle behind Geiger counters, which produce signals with no position or energy information, providing only a means of counting ionization events. Optimal proportional counter performance is achieved by not operating under unnecessarily high multiplication [53].

To mitigate the production of UV photons, a quenching gas must be added to absorb the photons into atomic states that do not lead to further UV emission. Additionally, a steep dependence of the multiplication on bias causes any small drift in the detector bias to lead to poor resolution. The introduction of a quench gas allows the higher gas multiplication to be reached without these adverse effects. It is important to note that proportional counter quench gases should not be confused with *quench* gases used for Geiger counters that rely on an entirely different mechanism to quench ionized charge [53]. During the $^{14}\mathrm{N}(a,p)$ experiment, a number of covalent gases (methane, CO_2, and H_2) at various mixture ratios were tested for the ANASEN AGT. In the online analysis, a quench gas of 1% CO_2 was selected for the initial test experiment.

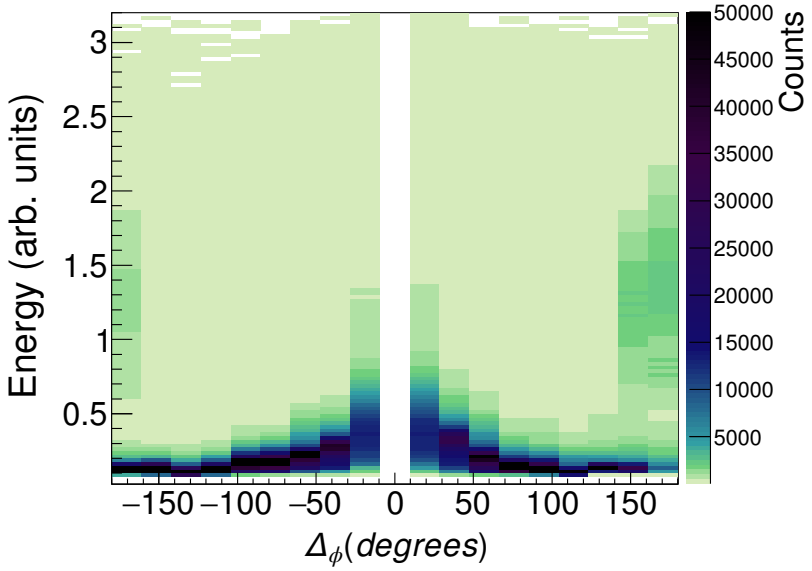

FIGURE 6.10: Signal pattern coincident with a saturation event in the proportional counter plotted versus angular separation from saturated wire. All wires experience *crosstalk* with intensity decreasing with distance. Signals at 180° separation are consistent with alpha scattering.

High values of gas multiplication are necessary for detecting protons which produce very little ionization in the gas. This can be problematic when a large amount of charge is deposited in the detector; then the gas multiplication is too high, re-

sulting in spurious pulses in the detector. Figure 6.10 shows an effect observed in the $^{14}\mathrm{N}(\alpha, p)$ measurement where all wires produce signals in coincidence with a highly ionizing event defined by an event that saturates the detector electronics. The amplitude of the spurious pulse is highest near the highly ionizing event and decreases geometrically with distance. The spurious pulse amplitude is comparable to the proton signal size at 180° away from the saturated wire. This is a problematic background for any two body reaction where protons are produced coincident with a heavy ion. It was also seen in hydrogen target gas elastic scattering experiments. Since ANASEN is an extended target, even small angle scattering can reach the anode wires. All events of this type must be vetoed, and the cut applied in the analysis is to reject all events where the readout electronics register a saturation. This cut rejects a number of potentially "good" events. Two groups near 180° in Figure 6.10 are tentatively attributed to $^{14}\mathrm{N}(\alpha, \alpha)$, and it is possible that some $^{14}\mathrm{N}(\alpha, p)$ events are also being rejected.

It should be noted that this effect is not simply eliminated by the introduction of more quenching gas. Increasing the quenching gas also increases the number of heavy ions in the target gas. This increases the potential for highly ionizing events due to elastic scattering on large Z nuclei in addition to increasing the stopping power of the target gas. Thus the problem of determining the optimum gas composition is quite complicated and requires further study.

6.4 Two-Body Reaction Reconstruction

Reconstruction of an event depends upon non-relativistic kinematics and energy loss calculations. We intend to select two-body reactions depicted in the laboratory frame by Figure 6.11. We begin by assuming all detections result from two-body reactions and, using the reconstructed beam energy and reaction Q-value, later reject events that are kinematically inconsistent. The reconstruction relies on the

detection of the light projectile ($p, t, ^3\mathrm{He}, \alpha$, etc) at two points and the determination of energy losses of the beam and the light particle through the target gas mixture.

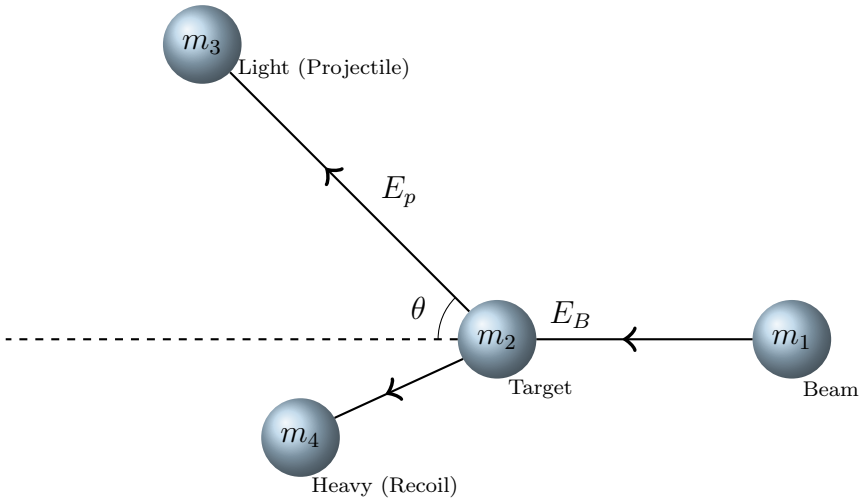

FIGURE 6.11: Schematic for a two body reaction in the laboratory frame

In the current implementation of ANASEN, the heavy recoil is not detected. The upgrade described in §7.2 has the potential to provide information about the heavy recoil for additional discrimination of backgrounds.

6.4.1 Event Selection and Two Point Tracking

Event singles are recorded by the data acquisition system when a silicon detector *back* channel triggers. Since random coincidences can cause additional triggers for a valid two body event, it is acceptable for multiple silicon detectors to trigger for a given event. However, events with more than one hit within a single detector are rejected. To reduce the effect of random coincidences, each silicon trigger is validated by the restriction that within a detector only one back channel fires in coincidence with a single front strip with one or both sides present. See §6.2.2 for more details on the silicon position determination. Further restriction and cor-

rections are applied such that the position reconstructed from front of the silicon detector is within the physical range of the back segment that triggered.

For a single event to be consistent with a two-body reaction, each silicon hit is correlated with a proportional counter signal located azimuthally within $\pm 20^\circ$ relative to the silicon hit. This restriction allows a possible coincidence between a silicon strip with up to three proportional counter wires. To remedy this, the maximum amplitude hit in the proportional counter is the one selected as the *true* coincidence. Ideally, the two detections of the particle track would be at exactly the same azimuthal angle; however, the azimuthal resolution of the track is limited by angular straggling in the gas as well as the segmentation of the DSSD and MAPC.

$$\sigma_{\phi_{Si}} = 360^\circ/(12 \text{ detectors})/(4 \text{ front strips}) = 7.5^\circ$$

$$\sigma_{\phi_{PC}} = 360^\circ/(19 \text{ wires}) = 18.9^\circ$$

$$\sigma_{\phi_{\text{TRACK}}} \gtrsim \sqrt{\sigma^2_{\phi_{Si}} + \sigma^2_{\phi_{PC}}} \simeq 20^\circ$$

In practice, the mismatch between the segmentation of the two detectors further limits the relative azimuthal resolution.

Once the event coincidences between the silicon array and the proportional counter are selected, the polar angle θ of the light particle can be calculated. This angle is critical for determining the center-of-mass energy of the reaction described in §6.4.5. This angle is also important for interpreting the proportional counter energy loss measurement to allow particle identification explained in section §6.4.3.

$$\theta = \arctan\left(\frac{r_{xy}}{\Delta z}\right) = \arctan\left(\frac{\sqrt{x^2_{Si} + y^2_{Si}} - \sqrt{x^2_{PC} + y^2_{PC}}}{z_{Si} - z_{PC}}\right) \tag{6.7}$$

It is important to note here that the angle θ could be defined differently. For example, more complicated methods allow the beam position to vary over an estimated beam geometry [74]. Using this angle θ, the reaction depth z is extrapolated back

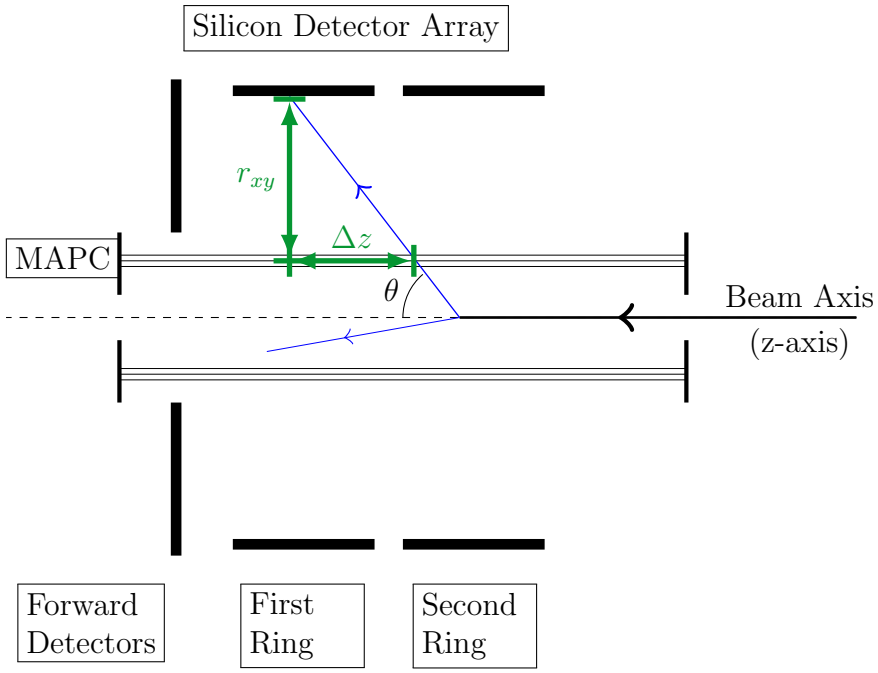

FIGURE 6.12: Schematic representation of ANASEN

to the central axis assuming that is the exact location of the beam. It is important to optimize the beam centering, focus, and emittance, to minimize any error introduced by assuming the beam direction and detector axis are aligned.

$$z = z_{Si} - \frac{\tan(\theta)}{\sqrt{x_{Si}^2 + y_{Si}^2}} \tag{6.8}$$

The reaction depth is needed to calculate the beam energy loss in the gas which is described in §6.4.2 and the Q-value of the reaction in section §6.4.4. This position information is what defines the AGT mode of ANASEN.

6.4.2 Energy Loss Calculations

Upstream of ANASEN the beam is energy selected, then loses energy in the entrance window and gas mixture, and then reacts with the target gas. Additionally, the light particle loses energy in the gas mixture before depositing the remainder of its energy in the silicon. Determining the particle energies at the reaction location, relevant for the kinematics calculations, depends upon calculated energy losses. The energy loss of a charged particle through an absorber depends upon

the particle energy, charge, and mass in addition to the absorber density and composition. The mean energy loss in a thin layer of material is given by the specific energy loss (or stopping power): $S(E)$ = -dE/dx. For this analysis, tabulated stopping powers were calculated using the binary collision code SRIM (Stopping and Range of Ions in Matter) which simulates ion interactions in matter [81]. The stopping powers used for the ^{14}N(a,p) analysis are plotted in Figure 6.13 in units of energy per unit mass thickness. Mass thickness is the product of the absorber

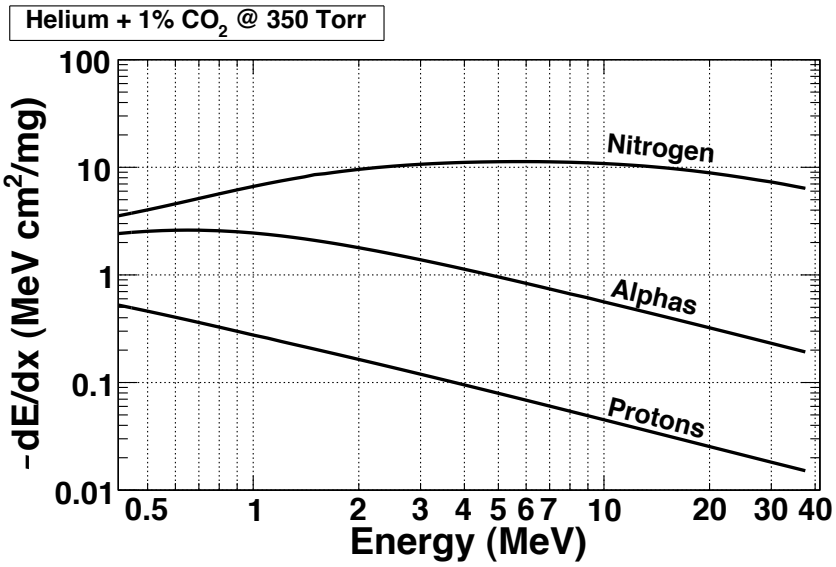

FIGURE 6.13: Stopping powers for alpha particles, protons, and ^{14}N in a helium carbon-dioxide gas mixture at 350 Torr calculated with SRIM.

thickness and density which is indicative of the number of electrons in the absorber because most common absorbers have similar Z/M. This is a natural unit for expressing stopping powers because the main mechanism for energy loss arises from ion-electron collisions. Multiplying the stopping power per unit mass thickness by density yields the stopping power in energy per unit length which is used in the

following integrations.

$$E(x+h) = E(x) - \int_{x}^{x+h} S\big(E(x')\big)\mathrm{d}x' \tag{6.9}$$

$$= E(x+n\Delta x) = E_n \simeq E_0 - \sum_{i=0}^{n-1} S(E_i)\Delta x$$

$$\Rightarrow E_n = E_{n-1} - S(E_{n-1})\Delta x \tag{6.10}$$

The energy of a particle after traversing a distance h through some material is calculated by integrating the stopping power along the forward path of the particle as shown in equation 6.9 approximated by a left Riemann sum. Equation 6.10 is implemented as a multistep recursive relation starting with the known energy E_0. At each iteration the value of the stopping power $S(E_i)$ at energy E_i is linearly interpolated from SRIM tabulated values, and then the energy E_{i+1} at the beginning of next step is calculated. However, equations 6.9 can be rewritten slightly approximating the integration instead by a right Riemann sum.

$$E(x+h) = E(x) - \int_{x}^{x+h} S\big(E(x')\big)\mathrm{d}x' \tag{6.11}$$

$$= E_n \simeq E_0 - \sum_{i=1}^{n} S(E_i)\Delta x$$

$$= E_{n-1} - S(E_n)\Delta x$$

$$\Rightarrow E_{n-1} = E_n + S(E_n)\Delta x \tag{6.12}$$

This allows the initial energy E_0 before losing energy in an absorber to be calculated from the known final energy E_n and thickness h.

6.4.3 Particle Identification

When a charged particle penetrates a layer of thin material, such that the stopping power is approximately constant, the energy loss ΔE is the product of the layer thickness t and the average stopping power S_{avg} [53].

$$\Delta E = tS_{avg} \tag{6.13}$$

For a particle with a given energy E, the average stopping power S_{avg} depends mainly on the particle charge squared. Thus, the charge of the particle can be determined from measuring the energy loss ΔE in a thin layer to determine S_{avg}, and the residual energy E in a second layer. This technique is called ΔE-E particle identification and is typically done using a two layered *particle-identifier telescope* of detectors viewing a small range of angles [53]. In ANASEN, the proportional counter measures the ΔE energy loss, and most of the residual energy is deposited in the silicon array.

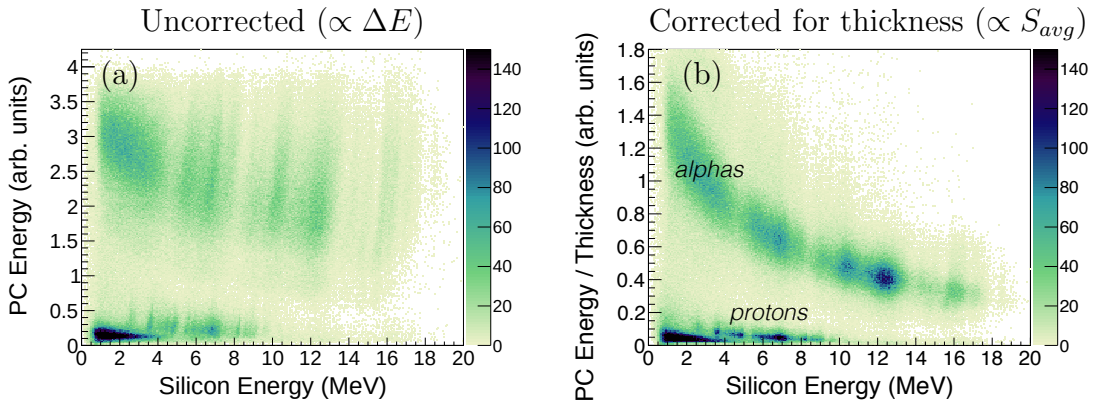

FIGURE 6.14: Tracking of the light particle angle improves particle identification resolution. (a) Energy loss in Proportional Counter versus Silicon Energy. (b) Energy loss in proportional counter adjusted for apparent thickness versus Silicon Energy. Both (a) & (b) contain events for the forward silicon detectors from the ^{14}N(a,p) dataset.

The energy measured by the MAPC is proportional to the total energy loss in the gas as long as the energy loss in both the active and dead regions is small. In this limit, the effect of the energy loss in dead regions on the particle identification is negligible. The proportional counter is parallel to the beam with an apparent thickness varying as the cosecant of the polar angle over a large range (see Figure 6.12 for a schematic of the geometry) and is easily corrected for angle

using,

$$S_{avg} = \frac{\Delta E}{t} \propto \Delta E \sin\theta. \tag{6.14}$$

The loci of points corresponding to protons and alphas shown in Figure 6.14 are well-separated after correcting for the apparent thickness. In other ANASEN experiments discrimination between protons and tritons as well as ^{6}He from ^{4}He has been demonstrated [82, 83]. The two dimensional gate applied to select proton events is shown in Figure 6.15.

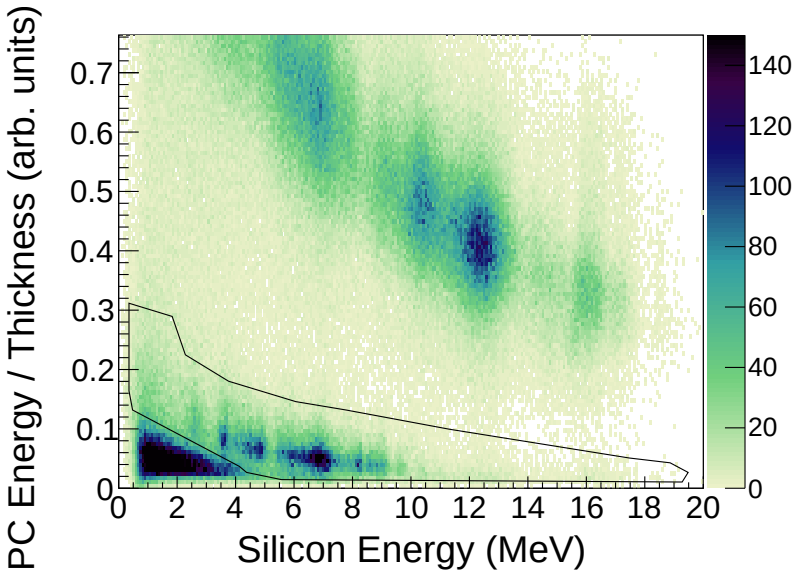

FIGURE 6.15: Particle identification plot showing the proton cut in black.

6.4.4 Q-value Determination

Determining the Q-value provides indication that the events of interest are indeed reconstructed properly. Furthermore, the Q-value distribution provides a discrimination between reactions that produce the heavy recoil in its ground state ($E_x^{\text{heavy}} = 0$) or in possible excited states ($E_x^{\text{heavy}} > 0$).

$$Q = \frac{m_3 + m_4}{m_4} E_p - \frac{m_4 - m_1}{m_4} E_B - 2\frac{\sqrt{m_1 m_3 E_p E_B}}{m_4} \cos\theta \tag{6.15}$$

$$= (m_4 + m_3 - m_1 - m_2)c^2 - E_x^{\text{heavy}} \tag{6.16}$$

The Q-value for the reaction is calculated using equation 6.15 using the reconstructed angle of the light particle θ, the beam energy $E_B(z)$ at a reaction depth z, the proton energy E_p immediately after the reaction, and the particle masses m_{1-4}. The beam energy is calculated starting from the rigidity selected radioactive beam energy and a series of energy loss calculations until finally reaching a depth z in the target. As shown in Figure 6.16 the ground state contribution ($E_x^{\text{heavy}} = 0$, $Q = -1.19$ MeV) is the dominant process. There is a signature of the first excited state contribution ($E_x^{\text{heavy}} = 0.87$ MeV, $Q = -2.06$ MeV); however, the Q-value resolution of approximately 1 MeV prevents clear discrimination between the two contributions.

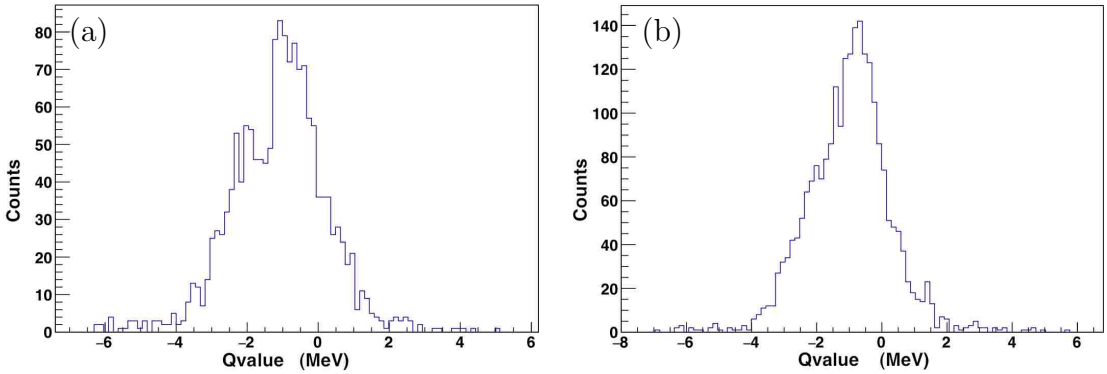

FIGURE 6.16: Representative Q-value distributions for two different energy regions showing overlapping components from ground state and first excited states in the recoiling nucleus. (a) The Q-value for center-of-mass energies 3.5 MeV to 4 MeV. (b) Same as (a) for center-of-mass energies 4 MeV to 4.5 MeV. The signature of the excited state contribution is most visible in (a) corresponding to the center-of-mass energy region where an excess is seen in the cross section from this work (see Figure 6.18).

It is important to note that the center-of-mass energy calculation described in §6.4.5 assumes a known Q-value. The Q-value spectra shown in Figure 6.16(a) and 6.16(b) are only used to distinguish specific states, and using the known Q-value to calculate the center-of-mass energy provides an enhancement to the center-of-mass

energy resolution. Since the excited state contribution cannot be separated in this case, center-of-mass energies calculated for the excited states are *inaccurate*.

6.4.5 Center-of-Mass Energy Calculation

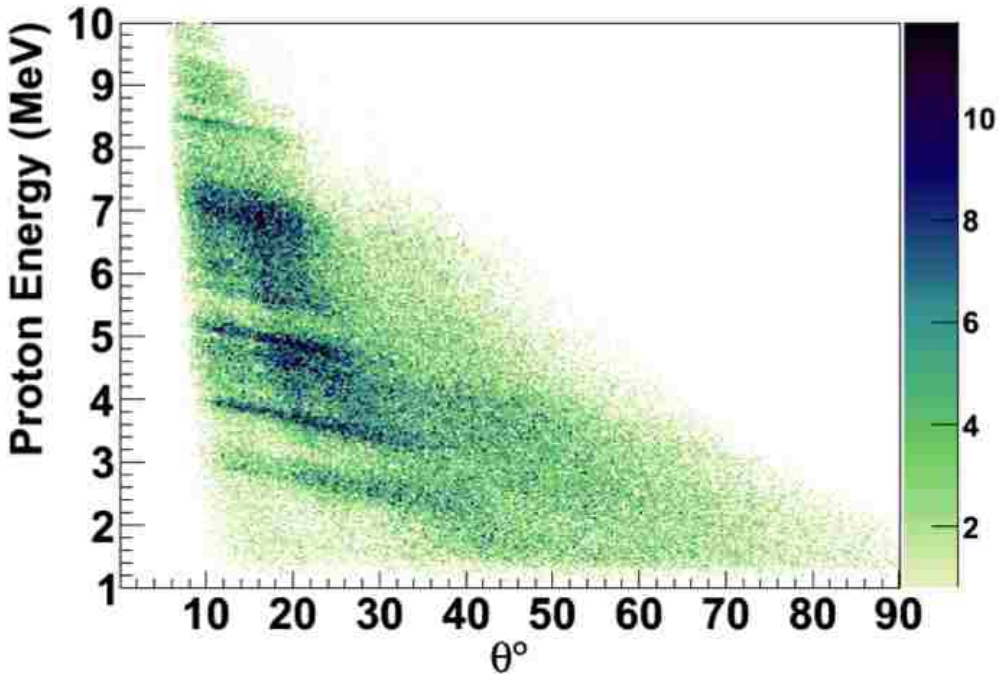

FIGURE 6.17: ^{14}N(α, p) Proton residual energy detected in the silicon detectors versus laboratory angle. Kinematic curves corresponding to center-of-mass energies that match resonances in the compound nucleus ^{18}F are visable at forward angles.

Using the known Q-value of the reaction and assuming different final states can be separated by Q-value, Equation 6.15 can be inverted to find the beam energy, E_B, at the location the reaction occurred from the proton energy and angle. This provides a better measure of the beam energy than the E_B which is determined by energy loss calculations using the reaction depth and known thicknesses of energy absorbing layers before the chamber. This leads to an enhancement in the resolution of the calculated center-of-mass energies using:

$$E_{cm} = \frac{M_2}{M_1 + M_2} E_B \tag{6.17}$$

The center-of-mass energy distribution is shown in Figure 6.18, scaled to compare to the regular kinematics measurement with an implanted ^{14}N target [10]. The

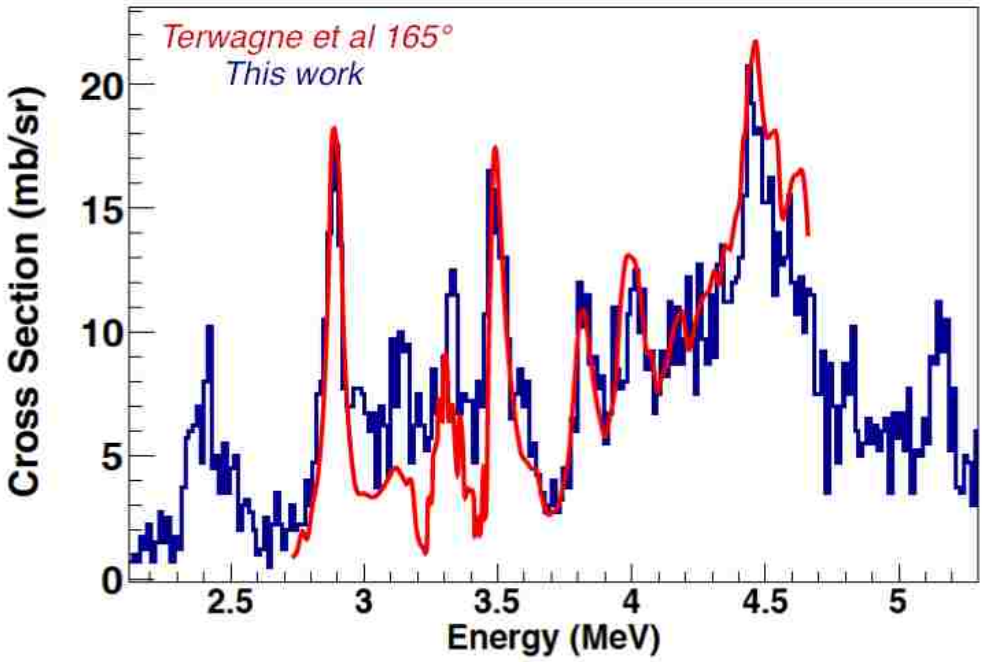

FIGURE 6.18: Excitation Function for the ^{14}N(α, p) reaction for forward detectors compared to the data from Terwagne *et al.* [10].

excess in yield in the region between 3 MeV and 3.5 MeV is due to the unseparated excited state contribution. As can be seen from the Q-value distribution shown in Figure 6.16(a) the excited state contribution is significant in this region. In this angular range, Terwagne *et al* report the first ^{14}N$(\alpha, p_1)^{17}$O* cross section in the region of 4.6 MeV to 5.6 MeV which would appear as an increased yield at lower energies due to effect of the Q-value error in the ANASEN spectra [10].

6.5 Towards ^{18}Ne(α, p) Radioactive Beam Experiment

The first attempt at measuring an (α, p) reaction with a radioactive beam was performed at the RESOLUT (REsonating SOlenoid Upscale Transmission) beamline of the John D. Fox Superconducting Linear Accelerator Laboratory at FSU. Approximately 0.5×10^4 ^{18}Ne$/s$ with 6% purity were produced by RESOLUT with

the *in-flight* method using the ^{16}O(^{3}He, n)^{18}Ne production reaction with a ^{3}He target at 350 Torr at 77° K producing a final radioactive beam energy in the target chamber of 56.3 MeV. To produce the radioactive beams, the in-flight technique filters and focuses the reaction products that are forward traveling with "beam-like" velocities. The reaction products have a range of initial angles and energies, which results in a beam with an increased energy spread and angular divergence at the target location relative to the ^{14}N tandem beam.

A number of successes were achieved in this experiment. A scintillator foil instrumented with a silicon photomultiplier (SiPM) was used to measure the timing relative to the accelerator RF signal to separate events due to the radioactive beam (^{18}Ne) from the more intense primary beam (^{16}O) as shown in Figure 6.19(b). As

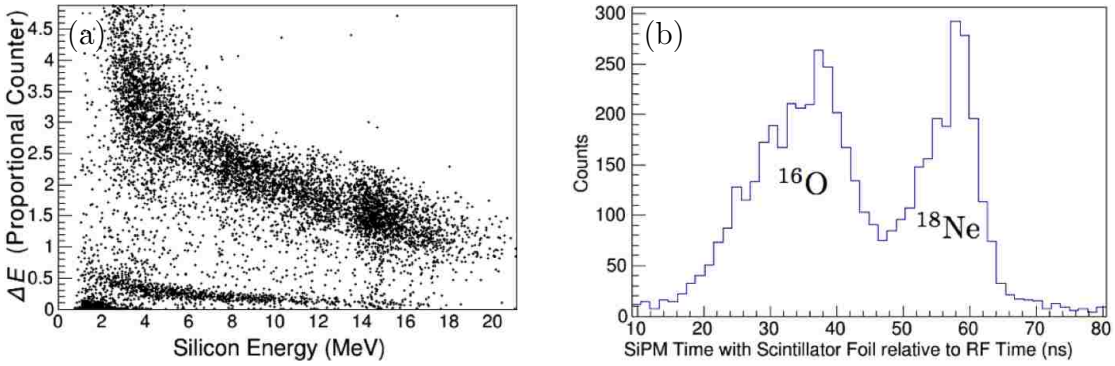

FIGURE 6.19: (a) ^{18}Ne(α, p) data from FSU experiment showing the identification of protons and alpha particles and (b) time-of-flight separation of the radioactive beam from the stable primary beam for proton events.

shown in Figure 6.19(a) protons and alpha particles were identified. Although, the number of protons detected were much higher than that expected by rate estimates using a 10 millibarn ^{18}Ne(α, p) cross section. Due to an sharply peaked intensity of protons originating from the upstream region of the detector, most likely the excess of protons were produced from background reactions occurring in the scintillator foil. Another complication arises from the increased emittance of

the radioactive beam as compared to the stable tandem beam used in the $^{14}\mathrm{N}(\alpha, p)$ experiment. The geometry of the beam is a limiting factor for the AGT mode of ANASEN. Increased emittance leads to more highly ionizing events in the proportional counter performance and introduces an error in the "on-axis" assumption in the reconstruction AGT mode of ANASEN. The new radioactive beams available from ReA3 at the NSCL are stopped, separated, and then reaccelerated which promises to provide well-defined beam geometry more suitable for ANASEN.

Chapter 7
Conclusions

Understanding the complex origins of intermediate mass nuclei (Ni-Sn) requires new direct measurements of nuclear reaction rates. This thesis addresses two projects targeting measurements of nuclear cross sections important for understanding nucleosynthesis in hot astrophysical environments.

We developed an approach using ANASEN for measurements of charged-particle reactions with radioactive ion beams that are important in stellar explosions. An active gas target capability is being developed, and a demonstration of direct (α, p) reaction measurements were conducted. Upgrades to the capabilities of ANASEN will refine this experimental technique for future experiments.

Direct measurements of neutron capture on ^{67}Zn and ^{68}Zn were performed using the Detector for Advanced Neutron Capture Experiments (DANCE) at the Los Alamos Neutron Science Center (LANSCE). A new $^{68}\mathrm{Zn}(n, \gamma)$ cross section in the neutron energy range from 150 eV to 850 keV and MACS from 20 keV-100 keV are reported along with the details of the analysis. New cross sections and MACS for $^{67}\mathrm{Zn}(n, \gamma)$ in the same energy range are forthcoming.

7.1 Implications of new ^{68}Zn MACS Result with DANCE

The new ^{68}Zn Maxwellian-Averaged Cross Sections for neutron energies from 20 keV to 100 keV determined in this work are listed in Table 4.1 and shown in Figure 7.1. These results provide a confirmation of the newer evaluated cross section [65, 6, 5] by Iwamoto which suggest a higher cross section, above 100 keV, than the previous measurement [42]. An Online tool NETZ[1] was used to estimate

[1] NETZ is not an acronym but rather the German word for network.

the influence of the new MACS on nucleosynthesis in the weak s process [12, 13]. The NETZ tool uses a simplified single neutron pulse model for the nucleosynthesis; however, it provides an preliminary estimate of the sensitivity of individual MACS that is qualitatively very similar to the more detailed sensitivity study by Pignateri *et al.* shown in Section 2.2. In the calculations shown in Figure 7.2, the MACS for ^{68}Zn are scaled by a constant where the reference MACS were taken from KADoNiS0.3 [84, 11].

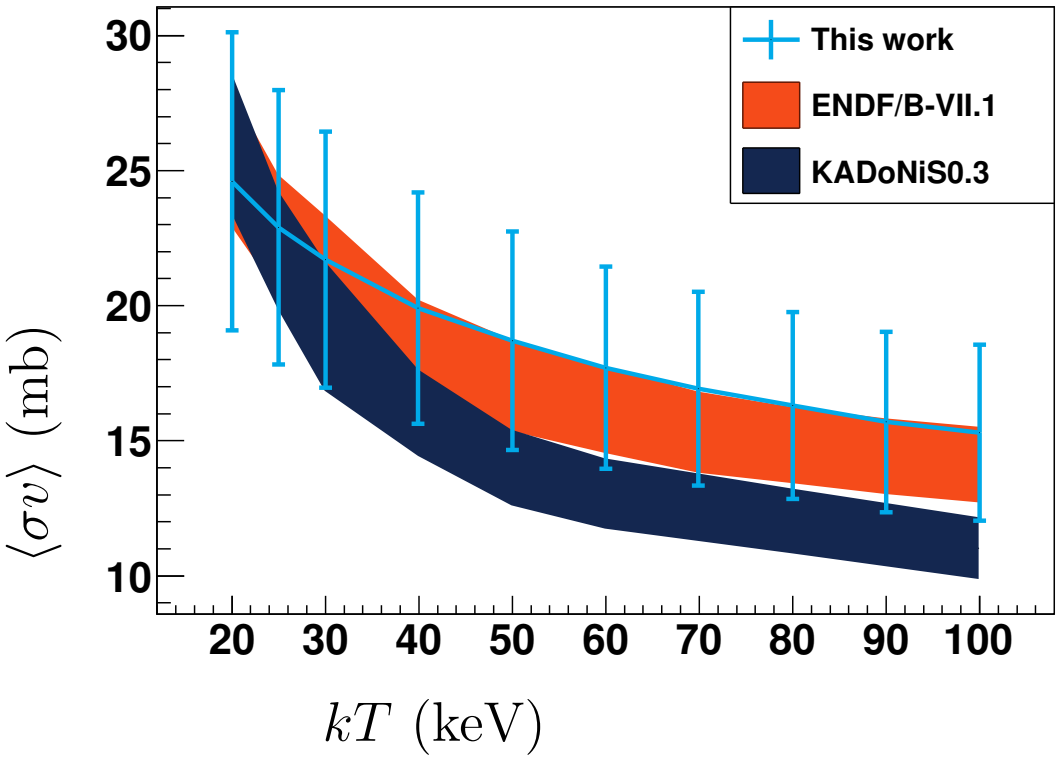

FIGURE 7.1: Plot of the MACS shown in Table 4.1 uncertainties on the standard MACS cross sections at each energy were conservatively estimated using the relative uncertainty reported at 30 keV by KADonNis0.3 [11]. Error bars shown for this work are the sum of the statistical and systematic uncertainties discussed in §4

The higher MACS near 90 keV will have a significant impact on the carbon shell burning phase of the weak s process. Further work on reducing the 20% systematic uncertainty in the efficiency from this measurement will provide a better determi-

nation of the MACS in this energy range and reduce uncertainties on abundance calculations. The effect of a 20% change in the ^{68}Zn(n,γ) cross section is illustrated in Figure 7.2 where weak s process abundances from A=74-90 are altered by nearly 10%. However, the cut efficiency does not vary substantially with neutron energy and results in a global scaling of the MACS. Despite the large 20% uncertainty, which place the MACS from this work in agreement with the KADoNIS0.3 compilation [11], the relative trend of the MACS with neutron energy depends upon the statistical uncertainties listed in Table 4.1 that are estimated to be less than 3%. Future work could further reduce the uncertainties in the MACS results from the DANCE ^{68}Zn(n,γ) experiment.

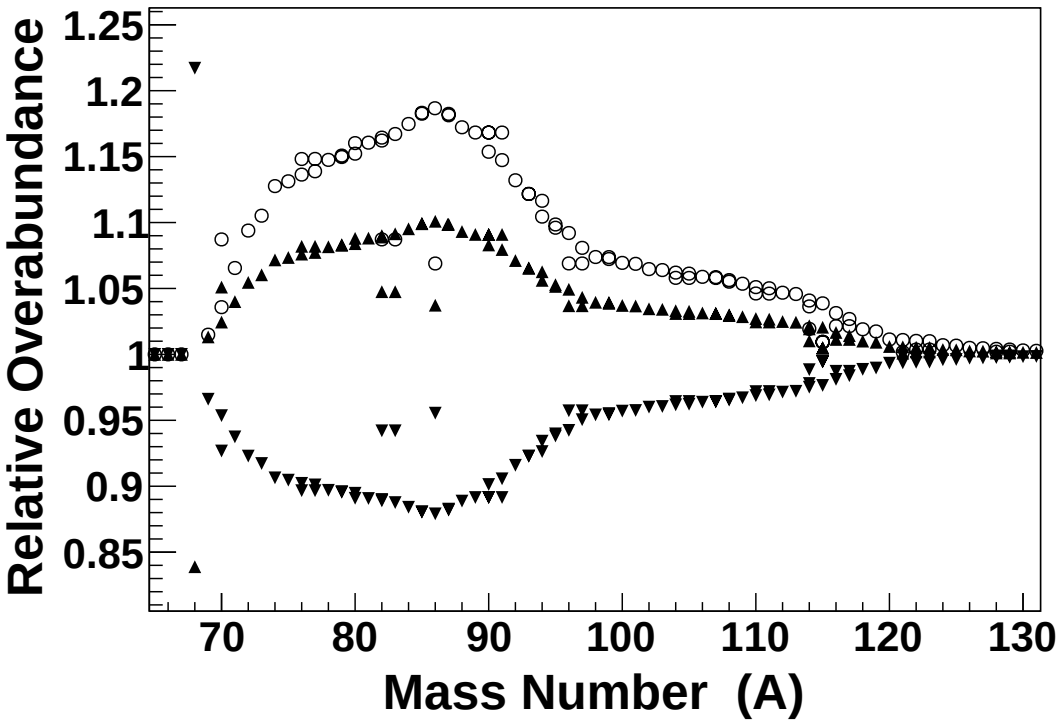

FIGURE 7.2: Sensitivity calculation using the NETZ Online tool [12, 13] showing the relative change in abundance as a function of mass number. Filled triangles represent the effect of a 20% ^{68}Zn MACS uncertainty on weak s process abundances. Upward (Downward) pointing triangles correspond to scaling the standard ^{68}Zn MACS up (down) by 20%. Open circles represent the effect of a 40% increase in the ^{68}Zn MACS.

The largest change is a 40% increase at 100 keV in the MACS relative to KADoNiS0.3 [11]. Since NETZ uses only a single scale factor, the effect scaling up the MACS at all neutron energies by a factor of 1.4 was used to investigate the significance of the higher MACS reported in this work. This resulted in up to a 20% change in the calculated weak s process abundances; however, this is most likely an overestimate of the influence of the higher MACS near 100 keV. In future work a more accurate determination of the weak s process abundances will be performed using a detailed stellar model, similar to the model used by Pignateri [2], including this new MACS for ^{68}Zn(n,γ) and a new MACS for ^{67}Zn(n,γ).

7.2 ANASEN Development

For many (α, p) reaction measurements, better Q-value resolution is needed than was achieved with the first version of the active target. The ground state and excited state contribution are overlapping in distribution shown in Figure 6.16. The ability to distinguish the population of excited states can be important achieving good center-of-mass energy resolution. Both good Q-value resolution and center-of-mass energy resolution can be important factors in determining the reaction rate.

We are developing a new active target design that incorporates a novel gas ionization detector to instrument the region near the beam with an ion chamber (IC) and improves the geometry of the MAPC. This new design required extending the footprint of the proportional counter, which is an improvement on its own for two reasons. The larger footprint includes finer segmentation using 24 anode wires, which is better matched to the geometry of the silicon array, improving angular reconstruction. Secondly, discharging or high rates with large multiplication lead to destruction of the quench gas introducing contaminants in the gas mixture, and both are detrimental for the detector performance and lifetime. This is more likely

to occur the closer the anode wires are to the beam axis and is correlated with the sporadic pulses in the MAPC. Moving the anodes wires further from the beam axis will reduce the presence of sporadic pulses described in §6.3.3. In addition to the adjustments to the geometry, an IC can provide a measurement of recoils at large scattering angles to improve the event reconstruction algorithms and assist in diagnosing sporadic pulses.

In the design of the IC, electric potential finite-element calculations (shown in Figures 7.3(a) and 7.3(b)) were performed to determine the path of charge carriers and the behavior of induced signals. The Shockley-Ramo Theorem [85, 86] is a quasi-static approximation used to predict and interpret the induced signals produced by both solid-state and gaseous ionization detectors. In this framework, charge drifting is governed by the electric field lines, and the induced charge at the signal electrode is determined by the change in weighting potential, φ_w, experienced along the path of charge q_0: $Q_{\text{induced}} = q_0 \Delta\varphi_w$. See He *et al.* [87] for a review of various applications of the Shockley-Ramo Theorem producing a number of examples and derivations.

The charge produced inside the detector is the desired quantity to measure rather than a path-dependent signal. This leads to the introduction of a Frisch grid in most ordinary ion chambers explicitly constraining the weighting potential to be zero everywhere except for a small region near the anode [53]. The design in the new ANASEN IC utilizes a "coplanar" anode configuration utilized in previous ionization based detectors in "planar" [87, 53] and later in cylindrical geometries [88, 89, 90]. As illustrated in the calculation shown in Figure 7.3(b), a subtraction of dual electrodes achieves an effective Frisch grid weighting potential. For localized ionization, such as the Bragg peak of charge particles stopping in the ion chamber region, this coplanar configuration has the potential to provide an

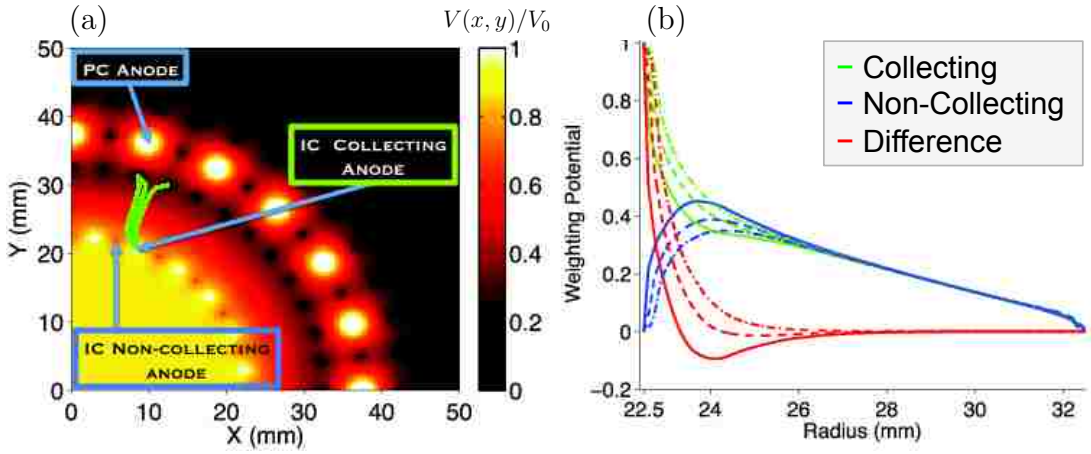

FIGURE 7.3: (a) Electric potential of proportional counter and ion chamber configuration with representative electric field lines inside IC region. The color scale represents the potential $V(x, y)/V_0$ where V_0 is the proportional counter bias voltage. The IC bias voltage in this case was set to $V_0/2$. (b) Weighting potential calculation demonstrating effective Frisch grid functionality for three representative charge trajectories. Line patterns correspond to the three different trajectories shown in green in (a).

estimate of radial position [89, 90]. The IC detector has been tested successfully with an ^{241}Am alpha source in isobutane gas at a pressure of approximately 100 Torr. An in-beam test experiment is needed to determine if the ion chamber indeed can provide a usable heavy-recoil signal to improve the resolution and background suppression. In the ^{241}Am source tests performed at LSU, a significant noise cancellation was observed upon subtracting the two signals. Since external sources will similarly effect both signal lines, any pickup noise is mitigated in a differential signal.

As part of the ANASEN upgrade, we have also upgraded the MAPC electronics. We have instrumented the detector with new linear preamplifiers and are developing a new digital data acquisition system that should improve the detector resolution, thresholds, and dynamic range. The new preamplifiers are coupled to the MAPC inside of the vacuum chamber and a second-stage, external linear amplifier allows variable gain control. A digital data acquisition system is now under

development to be used with the new preamplifiers in the MAPC readout. A new mounting scheme was also designed for the array to aid in accessing the individual detector components and improve the portability of ANASEN. Incorporated into the new detector mounting scheme is a target actuator system which allows the use of solid targets for calibration purposes. Systematic studies of the detector performance with the new target system are currently being performed, and a new campaign of ANASEN experiments has commenced.

References

[1] F. Käppeler, R. Gallino, S. Bisterzo, and Wako Aoki. The *s* process: Nuclear physics, stellar models, and observations. *Rev. Mod. Phys.*, 83:157–193, Apr 2011.

[2] M. Pignatari, R. Gallino, M. Heil, M. Wiescher, F. Käppeler, F. Herwig, and S. Bisterzo. The Weak s-Process in Massive Stars and its Dependence on the Neutron Capture Cross Sections. *Ap. J.*, 710:1557–1577, February 2010.

[3] J Ullmann. An Overview of DANCE; A 4pi BaF_2 Detector For Neutron Capture Measurements at LANSCE. *Progress of theoretical physics*, 96(2):275–306, 1996.

[4] J.M. Wouters, A.A. Vicente, T.A. Bredeweg, E. Esch, R.C. Haight, R. Hatarik, J.M. O'Donnell, R. Reifarth, R.S. Rundberg, J.M. Schwantes, S.A. Sheets, J.L. Ullmann, D.J. Vieira, and J.B. Wilhelmy. Acquisition-analysis system for the DANCE (detector for advanced neutron capture experiments) BaF_2 gamma-ray calorimeter. *IEEE Transactions on Nuclear Science*, 53(3):880–885, June 2006.

[5] M Chadwick et al. ENDF/B-VII.1 Nuclear Data for Science and Technology: Cross Sections, Covariances, Fission Product Yields and Decay Data. *Nuclear Data Sheets*, 112(12):2887–2996, December 2011.

[6] Keiichi Shibata, Osamu Iwamoto, Tsuneo Nakagawa, Nobuyuki Iwamoto, Akira Ichihara, Satoshi Kunieda, Satoshi Chiba, Kazuyoshi Furutaka, Naohiko Otuka, Takaaki Ohasawa, Toru Murata, Hiroyuki Matsunobu, Atsushi Zukeran, So Kamada, and Jun-ichi Katakura. JENDL-4.0: A New Library for Nuclear Science and Engineering. *Journal of Nuclear Science and Technology*, 48(1):1–30, January 2011.

[7] A. Matic, A. M. van den Berg, M. N. Harakeh, H. J. Wörtche, M. Beard, G. P. A. Berg, J. Görres, P. LeBlanc, S. OBrien, M. Wiescher, K. Fujita, K. Hatanaka, Y. Sakemi, Y. Shimizu, Y. Tameshige, A. Tamii, M. Yosoi, T. Adachi, Y. Fujita, Y. Shimbara, H. Fujita, T. Wakasa, J. P. Greene, R. Crowter, and H. Schatz. High-precision $^{28}\mathrm{Si}(p,t)^{26}\mathrm{Si}$ reaction to determine $^{22}\mathrm{Mg}(\alpha,p)^{25}\mathrm{Al}$ reaction rates. *Physical Review C*, 84(2), August 2011.

[8] P. Mohr and A. Matic. Examination and experimental constraints of the stellar reaction rate factor $\mathrm{N}_A \langle \sigma v \rangle$ of the $^{18}\mathrm{Ne}(\alpha,p)^{21}\mathrm{Na}$ reaction at temperatures of x-ray bursts. *Physical Review C*, 87, 2013.

[9] E. Koshchiy, J. C. Blackmon, G. V. Rogachev, Wiedenhöever, L. Baby, P. Barber, D. Bardayan, J. Belarge, D. Caussyn, E. D. Johnson, K. Kemper, A. N. Kuchera, L. E. Linhardt, K. T. Macon, M. Matoš, L. L. Mondello, and

D. Santiago-Gonzales. Anasen: the array for nuclear astrophysics and structure with exotic nuclei. *NIM A*, in preparation.

[10] G. Terwagne, G. Genard, M. Yedji, and G. G. Ross. Cross-section measurements of the ^{14}N$(\alpha, p)^{17}$O and ^{14}N$(\alpha, \alpha)^{14}$N reactions between 3.5 and 6 MeV. *Journal of Applied Physics*, 104(8):084909, 2008.

[11] I. Dillmann, R Plag, F Käppeler, and T Rauscher. The third update of the "karlsruhe astrophysical database of nucleosynthesis in stars". *EFNUDAT Fast Neutrons, Proceedings of the Scientific Workshop on Neutron Measurements*, 2009.

[12] S. Jaag, J. Ostermller, R. Plag, R. Reifarth, S. Schmidt, and M. Weigand. NETZ.

[13] M. Weigand, T. A. Bredeweg, A. Couture, K. Göbel, T. Heftrich, M. Jandel, F. Käppeler, C. Lederer, N. Kivel, G. Korschinek, M. Krtička, J. M. O'Donnell, J. Osterm oller, R. Plag, R. Reifarth, D. Schumann, J. L. Ullmann, and A. Wallner. ^{63}Ni(n, γ) cross sections measured with DANCE. *Physical Review C*, 92(4), October 2015.

[14] E. M. Burbidge, G. R. Burbidge, William A. Fowler, and F. Hoyle. Synthesis of the elements in stars. *Rev. of Mod. Phys.*, 29:547, 1957.

[15] A. G. W. Cameron. Nuclear Astrophysics. *Annual Review of Nuclear and Particle Science*, 8:299–326, 1958.

[16] C. Lederer and *et al.* ^{62}Ni(n, γ) and ^{63}Ni(n, γ) cross sections measured at the n_{TOF} facility at cern. *Phys. Rev. C*, 89:025810, Feb 2014.

[17] F. Käppeler, H. Beer, and K. Wisshak. s-process studies in the light of new experimental cross sections: distribution of neutron fluences and r-process residuals. *The Astrophysical Journal*, 257:821–846, June 1982.

[18] C. Arlandini, F. Käppeler, K. Wisshak, R. Gallino, M. Lugaro, M. Busso, and O. Straniero. Neutron Capture in Low-Mass Asymptotic Giant Branch Stars: Cross Sections and Abundance Signatures. *The Astrophysical Journal*, 525(2):886–900, November 1999.

[19] C. Travaglio, R. Gallino, E. Arnone, J. Cowan, F. Jordan, and C. Sneden. Galactic Evolution of Sr, Y, and Zr: A Multiplicity of Nucleosynthetic Processes. *The Astrophysical Journal*, 601(2):864–884, February 2004.

[20] Z. Y. Bao, H. Beer, F. Käppeler, F. Voss, K. Wisshak, and T. Rauscher. Neutron cross sections fot nucleosynthesis studies. *At. Data and Nucl. Data Tabl.*, 76:70, 2000.

[21] Sachiko Amari. Recent Progress in Presolar Grain Studies. *Mass Spectrometry*, 3(Special_Issue_3):S0042–S0042, 2014.

[22] A. Couture and R. Reifarth. Direct measurements of neutron capture on radioactive isotopes. *Atomic Data and Nuclear Data Tables*, 93(5):807–830, September 2007.

[23] F. Montes, T. C. Beers, J. Cowan, T. Elliot, K. Farouqi, R. Gallino, M. Heil, K.-L. Kratz, B. Pfeiffer, and M. Pignatari. Nucleosynthesis in the early galaxy. *The Astrophysical Journal*, 671(2):1685, 2007.

[24] J. Cowan, C. Sneden, T. Beers, J. Lawler, J. Simmerer, J. Truran, F. Primas, J. Collier, and S. Burles. Hubble Space Telescope observations of heavy elements in metal-poor galactic halo stars. *The Astrophysical Journal*, 627(1):238, 2005.

[25] Christopher Sneden, John J. Cowan, and Roberto Gallino. Neutron-Capture Elements in the Early Galaxy. *Annual Review of Astronomy and Astrophysics*, 46(1):241–288, September 2008.

[26] C. Sneden, J. Cowan, J. Lawler, I. Ivans, S. Burles, T. Beers, F. Primas, V. Hill, J. Truran, M. Fuller, B. Pfeiffer, and K. Kratz. The Extremely Metal-poor, Neutron Capture-rich Star CS 22892-052: A Comprehensive Abundance Analysis. *The Astrophysical Journal*, 591(2):936–953, July 2003.

[27] S. Honda, W. Aoki, Y. Ishimaru, and S. Wanajo. Neutron-Capture Elements in the Very Metal-poor Star HD 88609: Another Star with Excesses of Light Neutron-Capture ElementsBased on data collected at the Subaru Telescope, which is operated by the National Astronomical Observatory of Japan. *The Astrophysical Journal*, 666(2):1189, 2007.

[28] M. Pignatari and R. Gallino. The Weak *s* Process at Low Metallicity. In *AIP Conference Proceedings*, volume 990, pages 336–338. AIP Publishing, March 2008.

[29] U. Frischknecht, R. Hirschi, M. Pignatari, A. Maeder, G. Meynet, C. Chiappini, F-K. Thielemann, T. Rauscher, C. Georgy, and S. Ekström. *s* -process production in rotating massive stars at solar and low metallicities. *Monthly Notices of the Royal Astronomical Society*, 456(2):1803–1825, February 2016.

[30] C. Fröhlich and D. Hatcher. Influence of nuclear reaction rates on the nucleosynthesis in neutrino-driven winds. *EPJ Web of Conferences*, 93:03008, 2015.

[31] S. Wanajo, H-T. Janka, and S. Kubono. Uncertainties in the νp -process: Supernova dynamics versus nuclear physics. *The Astrophysical Journal*, 729(1):46, March 2011.

[32] N. Prantzos, M. Hashimoto, and K. Nomoto. The s-process in massive stars - Yields as a function of stellar mass and metallicity. *Astronomy and Astrophysics*, 234:221–229, 1990.

[33] C. M. Raiteri, R. Gallino, and M. Busso. S-processing in massive stars as a function of metallicity and interpretation of observational trends. *The Astrophysical Journal*, 387:263, March 1992.

[34] M. Pignatari and R. Gallino. The Weak sProcess at Low Metallicity. In *AIP Conference Proceedings*, volume 990, pages 336–338. AIP Publishing, March 2008.

[35] C. M. Raiteri, M. Busso, G. Picchio, and R. Gallino. S-process nucleosynthesis in massive stars and the weak component. II - Carbon burning and galactic enrichment. *The Astrophysical Journal*, 371:665, April 1991.

[36] H. Nassar, M. Paul, I. Ahmad, D. Berkovits, M. Bettan, P. Collon, S. Dababneh, S. Ghelberg, J. P. Greene, A. Heger, M. Heil, D. J. Henderson, C. L. Jiang, F. Käppeler, H. Koivisto, S. O'Brien, R. C. Pardo, N. Patronis, T. Pennington, R. Plag, K. E. Rehm, R. Reifarth, R. Scott, S. Sinha, X. Tang, and R. Vondrasek. Stellar (n, γ) cross section of ^{62}Ni. *Phys. Rev. Lett.*, 94(9):092504, Mar 2005.

[37] A. Alpizar-Vicente, T. Bredeweg, E.-I. Esch, U. Greife, R. Haight, R. Hatarik, J. O'Donnell, R. Reifarth, R. Rundberg, J. Ullmann, D. Vieira, and J. Wouters. Neutron capture cross section of ^{62}Ni at s-process energies. *Physical Review C*, 77(1), January 2008.

[38] I. Dillmann, M. Heil, R. Käppeler, R. Plag, T Rauscher, and F.-K. Thielemann. KADoNiS- the Karlsruhe Astrophysical Database of Nucleosynthesis in Stars. *AIP Conf. Proc.*, 819:123, 2009.

[39] J. Marganiec, I. Dillmann, C. Domingo Pardo, F. Käppeler, R. Reifarth, R. Gallino, M. Pignatari, and P. Grabmayr. Neutron capture cross sections of ^{74}Ge, ^{76}Ge, and ^{75}As at 25 kev. *Phys. Rev. C*, 79:065802, Jun 2009.

[40] M. Heil, F. Käppeler, E. Uberseder, R. Gallino, and M. Pignatari. Neutron capture cross sections for the weak *s* process in massive stars. *Phys. Rev. C*, 77:015808, Jan 2008.

[41] J. Garg, V. Tikku, J. Harvey, R. L Macklin, and J. Halperin. Phys. Rev. C 24, 1922 (1981) - Statistical properties of complex states of ^{67}Zn. *PRC*, 24(5):1922–1939, November 1981.

[42] J. Garg, V. Tikku, J. Harvey, J. Halperin, and R. Macklin. Neutron resonance parameters of ^{68}Zn + n and statistical distributions of level spacings and widths. *Physical Review C*, 25(4):1808–1823, April 1982.

[43] H. M. Agrawal, J. B. Garg, V. K. Tikku, J. A. Harvey, and R. L. Macklin. High-resolution neutron total and capture cross sections in ^{67}Zn. *Journal of Physics G: Nuclear and Particle Physics*, 18(6):1069–1087, June 1992.

[44] R. Reifarth, S. Dababneh, M. Heil, F. Kppeler, R. Plag, K. Sonnabend, and E. Uberseder. Neutron activation of natural zinc samples at kT = 25 keV. *Physical Review C*, 85(3), March 2012.

[45] P. Lisowski and K. Schoenberg. The Los Alamos Neutron Science Center. *Nuclear Instruments and Methods in Physics Research Section A: Accelerators, Spectrometers, Detectors and Associated Equipment*, 562(2):910–914, June 2006.

[46] SAMMY, Multilevel R-Matrix Fits to Neutron and Charged-Particle Cross-Section Data Using Bayes' Equations.

[47] A. Couture. private communication, February 2016.

[48] M. Heil, R. Reifarth, M.M Fowler, R.C. Haight, F. Käppeler, R.S. Rundberg, E.H. Seabury, J.L Ullmann, J.B. Wilhelmy, and K. Wisshak. A detector for (n, γ) cross-section measurements at a spallation neutron source. *Nuclear Instruments and Methods in Physics Research Section A: Accelerators, Spectrometers, Detectors and Associated Equipment*, 459(1-2):229–246, February 2001.

[49] R. Reifarth, T.A. Bredeweg, A. Alpizar-Vicente, J.C. Browne, E.-I. Esch, U. Greife, R.C. Haight, R. Hatarik, A. Kronenberg, J.M. O'Donnell, R.S. Rundberg, J.L. Ullmann, D.J. Vieira, J.B. Wilhelmy, and J.M. Wouters. Background identification and suppression for the measurement of (n, γ) reactions with the DANCE array at LANSCE. *Nuclear Instruments and Methods in Physics Research Section A: Accelerators, Spectrometers, Detectors and Associated Equipment*, 531(3):530–543, oct 2004.

[50] Trace. Stable Isotopes Supplier. http://www.tracesciences.com/.

[51] J. L. Ullmann, T. Kawano, T. A. Bredeweg, A. Couture, R. C. Haight, M. Jandel, J. M. O'Donnell, R. S. Rundberg, D. J. Vieira, J. B. Wilhelmy, J. A. Becker, A. Chyzh, C. Y. Wu, B. Baramsai, G. E. Mitchell, and M. Krtička. Cross section and γ-ray spectra for $^{238}\mathrm{U}(n, \gamma)$ measured with the DANCE detector array at the Los Alamos Neutron Science Center. *Physical Review C*, 89(3), March 2014.

[52] M. Jandel, T. A. Bredeweg, E. M. Bond, M. B. Chadwick, R. R. Clement, A. Couture, J. M. O'Donnell, R. C. Haight, T. Kawano, R. Reifarth, R. S. Rundberg, J. L. Ullmann, D. J. Vieira, J. B. Wilhelmy, J. M. Wouters, U. Agvaanluvsan, W. E. Parker, C. Y. Wu, and J. A. Becker. Neutron capture cross section of Am 241. *Physical Review C*, 78(3), September 2008.

[53] G. Knoll. *Radiation detection and measurement*. John Wiley, Hoboken, N.J, 4th ed edition, 2010.

[54] P. Finnerty, S. MacMullin, H.O. Back, R. Henning, A. Long, K.T. Macon, J. Strain, R.M. Lindstrom, and R.B. Vogelaar. Low-background gamma counting at the Kimballton Underground Research Facility. *NIM A*, 642(1):65–69, June 2011.

[55] W. T. Eadie, D. Drijard, F. James, M. Roos, , and B. Sadoulet. *Statistical Methods in Experimental Physics*. North-Holland, 1971.

[56] S. Mosby, T. A. Bredeweg, A. Chyzh, A. Couture, R. Henderson, M. Jandel, E. Kwan, J. M. O'Donnell, J. L. Ullmann, and C. Y. Wu. Improved neutron capture cross section of ^{239}Pu. *Phys. Rev. C*, 89:034610, Mar 2014.

[57] W. Press, editor. *Numerical recipes in FORTRAN: the art of scientific computing*. Cambridge University Press, Cambridge [England] ; New York, NY, USA, 2nd ed edition, 1992.

[58] R. Brun and F. Rademakers. ROOTan object oriented data analysis framework. *Nuclear Instruments and Methods in Physics Research Section A: Accelerators, Spectrometers, Detectors and Associated Equipment*, 389(1):81–86, 1997. See also http://root.cern.ch/.

[59] Eddy Offermann. This macro shows several ways to perform a linear least-squares. ROOT Data Analysis Framework.

[60] F. Bečvàř. Simulation of γ cascades in complex nuclei with emphasis on assessment of uncertainties of cascade-related quantities. *Nuclear Instruments and Methods in Physics Research Section A: Accelerators, Spectrometers, Detectors and Associated Equipment*, 417(2-3):434–449, November 1998.

[61] T. von Egidy and D. Bucurescu. Experimental energy-dependent nuclear spin distributions. *Physical Review C*, 80(5), November 2009.

[62] S.G. Kadmenskij, V.P. Markushev, and V.I. Furman. *Yad. Fiz.*, 37, 1983.

[63] M. Krtička. private communication, June 2016.

[64] M. Jandel, T.A. Bredeweg, A. Couture, M.M. Fowler, E.M. Bond, M.B. Chadwick, R.R.C. Clement, E.-I. Esch, J.M. ODonnell, R. Reifarth, R.S. Rundberg, J.L. Ullmann, D.J. Vieira, J.B. Wilhelmy, J.M. Wouters, R.A. Macri, C.Y. Wu, and J.A. Becker. GEANT4 simulations of the DANCE array. *Nuclear Instruments and Methods in Physics Research Section B: Beam Interactions with Materials and Atoms*, 261(1-2):1117–1121, August 2007.

[65] N. Iwamoto. New Evaluation of Neutron Nuclear Data for Zinc Isotopes. *Journal of Nuclear Science and Technology*, 44(9):1131–1141, September 2007.

[66] S. F. Mughabghab, M. Divadeenam, and N.E. Holden, editors. *Neutron cross sections*, volume 1A. Academic Press, New York, 4th ed. edition, 1981.

[67] B. Pritychenko and S.F. Mughabghab. Neutron Thermal Cross Sections, Westcott Factors, Resonance Integrals, Maxwellian Averaged Cross Sections and Astrophysical Reaction Rates Calculated from the ENDF/B-VII.1, JEFF-3.1.2, JENDL-4.0, ROSFOND-2010, CENDL-3.1 and EAF-2010 Evaluated Data Libraries. *Nuclear Data Sheets*, 113(12):3120–3144, December 2012.

[68] H. Schatz, A. Aprahamian, J. Grres, M. Wiescher, T. Rauscher, J.F. Rembges, F.-K. Thielemann, B. Pfeiffer, P. Mller, K.-L. Kratz, H. Herndl, B.A. Brown, and H. Rebel. rp-process nucleosynthesis at extreme temperature and density conditions. *Physics Reports*, 294(4):167–263, February 1998.

[69] C. Iliadis. *Nuclear physics of stars*. Physics textbook. Wiley-VCH-Verl, Weinheim, 2007. OCLC: 180973597.

[70] A. Parikh, J. José, and F. Moreno. The effects of variations in nuclear processes on Type I X-Ray Burst nucleosynthesis. *The Astrophysical Journal Supplement Series*, 178:110–136, 2008.

[71] R. Cyburt et al. Kepler: Light curve impact, submitted to APJ.

[72] P. Salter, M. Aliotta, T. Davinson, H. Al Falou, A. Chen, B. Davids, B. Fulton, N. Galinski, D. Howell, G. Lotay, P. Machule, A. Murphy, C. Ruiz, S. Sjue, M. Taggart, P. Walden, and P. Woods. Measurement of the $^{18}\mathrm{Ne}(\alpha, p_0)^{21}\mathrm{Na}$ Reaction Cross Section in the Burning Energy Region for X-Ray Bursts. *Physical Review Letters*, 108(24), June 2012.

[73] A. Matic, A. M. van den Berg, M. N. Harakeh, H. J. Wrtche, K. Fujita, K. Hatanaka, Y. Sakemi, Y. Shimizu, Y. Tameshige, A. Tamii, M. Yosoi, T. Adachi, Y. Fujita, Y. Shimbara, H. Fujita, T. Wakasa, P. O. Hess, B. A. Brown, and H. Schatz. High-precision (p, t) reaction measurement to determine $^{18}\mathrm{Ne}(\alpha, p)^{21}\mathrm{Na}$ reaction rates. *Physical Review C*, 80(5), November 2009.

[74] D. Groombridge, A. C Shotter, W. Bradfield-Smith, S. Cherubini, T. Davinso, A. Di Pietro, J. Gorres, A. M Laird, P. Leleux, Ad. Musumarra, A. Ninane, A. N. Ostrowski, J. Rahighi, H. Schatz, M. Wiescher, and P. J. Woods. Breakout from the hot cno cycle via the $^{18}\mathrm{Ne}(\alpha, p)^{21}\mathrm{Na}$ reaction. ii. extended energy range $\mathrm{E}_{c.m}$ 1.7-2.9 mev. *Physical Review C*, 66:1–10, 2001.

[75] Micron Semiconductor. Micron silicon detector catalogue, Janurary 2016. http://www.micronsemiconductor.co.uk/pdf/cat.pdf.

[76] SCIONIX. Dedicated scintillation detectors. http://www.scionix.nl.

[77] P. M. S. Blackett and D. S. Lees. Investigations with a Wilson Chamber. I. On the Photography of Artificial Disintegration Collisions. *Proceedings of the Royal Society A: Mathematical, Physical and Engineering Sciences*, 136(829):325–338, May 1932.

[78] L. Pratt. *Study of* ^{18}Ne *using the array for nuclear astrophysics and structure with exotic nuclei*. PhD thesis, Louisiana State University, 2014.

[79] W. Diethorn. A methane proportional counter system for natural radiocarbon measurements. Technical Report NYO-6628, United States Atomic Energy Commission, Technical Information Service, 1956., Oak Ridge, Tennessee, 1956.

[80] Mesytec. Mpr-16/32/64-log. http://www.mesytec.com/products/datasheets.

[81] J. Ziegler, M.D. Ziegler, and J.P. Biersack. SRIM, The stopping and range of ions in matter (2010). *NIM B*, 268(11-12):1818–1823, June 2010.

[82] G. V. Rogachev, L. Baby, J. Belarge, J. C. Blackmon, V. Z. Goldberg, E. D. Johnson, E. Koshchiy, A. N. Kuchera, J. Lai, L. Linhardt, K. Macon, M. Matoš, D. Santiago-Gonzales, and I. Wiedenhöever. Clustering in A= 10 nuclei. In *Journal of Physics: Conference Series*, volume 436, page 012041. IOP Publishing, April 2013.

[83] G V Rogachev, M L Avila, A N Kuchera, L T Baby, J Belarge, J Blackmon, V Z Goldberg, E D Johnson, K W Kemper, E Koshchiy, L Linhardt, K Macon, D Santiago-Gonzalez, and I Wiedenhöver. Clustering in non-self-conjugate nuclei ^{10}Be and ^{18}O. *Journal of Physics: Conference Series*, 569:012004, dec 2014.

[84] R. Reifarth. private communication, June 2016.

[85] W. Shockley. Currents to Conductors Induced by a Moving Point Charge. *Journal of Applied Physics*, 9(10):635, 1938.

[86] S. Ramo. Currents Induced by Electron Motion. *Proceedings of the IRE*, 27(9):584–585, September 1939.

[87] Z. He. Review of the Shockley Ramo theorem and its application in semiconductor gamma-ray detectors. *Nuclear Instruments and Methods in Physics Research Section A: Accelerators, Spectrometers, Detectors and Associated Equipment*, 463(1-2):250–267, May 2001.

[88] C.J. Sullivan, Z. He, G.F. Knoll, G. Tepper, and D.K. Wehe. A high pressure xenon gamma-ray spectrometer using a coplanar anode configuration. *Nuclear Instruments and Methods in Physics Research Section A: Accelerators, Spectrometers, Detectors and Associated Equipment*, 505(1-2):238–241, June 2003.

[89] S. Kiff, Z He, and G.C. Tepper. Radial position sensing in a coplanar-grid high-pressure xenon gamma-ray spectrometer. *IEEE Transactions on Nuclear Science*, 53(3):1380–1384, June 2006.

[90] S. Kiff, Z. He, and G. Tepper. Improving Spectroscopic Performance of a Coplanar-Anode High-Pressure Xenon Gamma-Ray Spectrometer. *IEEE Transactions on Nuclear Science*, 54(4):1263–1270, August 2007.

Appendix A: Total Energy Spectra Illustrating Background Subtraction for $E_n > 50$ keV and M=[2,5]

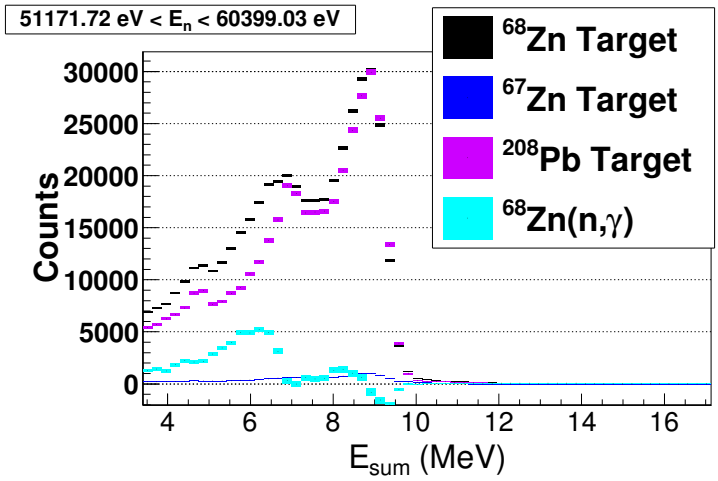

FIGURE 7.4: Representative background-subtracted E_{sum} distribution shown along with the fitted background components for 51172 eV $< E_n <$ 60399 eV.

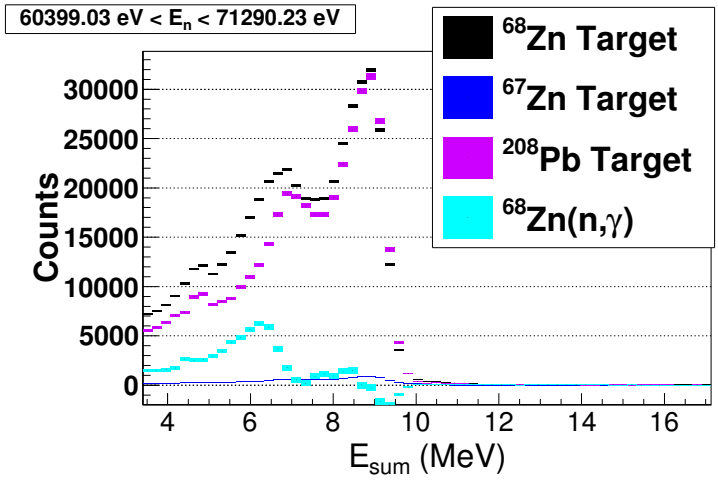

FIGURE 7.5: Representative background-subtracted E_{sum} distribution shown along with the fitted background components for 60399 eV $< E_n <$ 71290 eV.

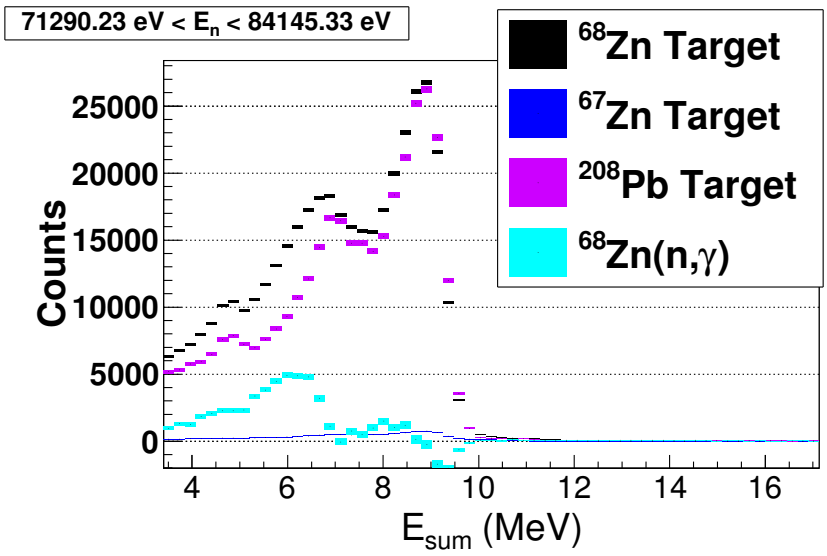

FIGURE 7.6: Representative background-subtracted E_{sum} distribution shown along with the fitted background components for 71290 eV $< E_n <$ 84145 eV.

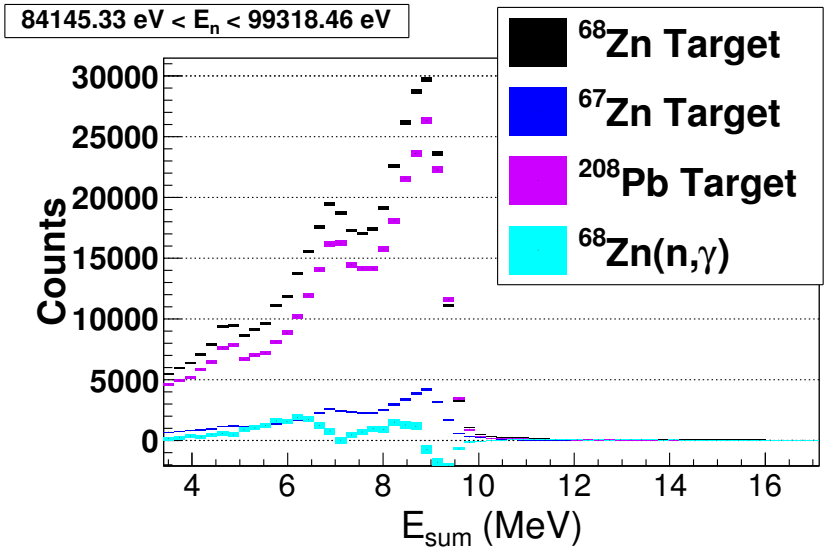

FIGURE 7.7: Representative background-subtracted E_{sum} distribution shown along with the fitted background components for 84145 eV $< E_n <$ 99318 eV.

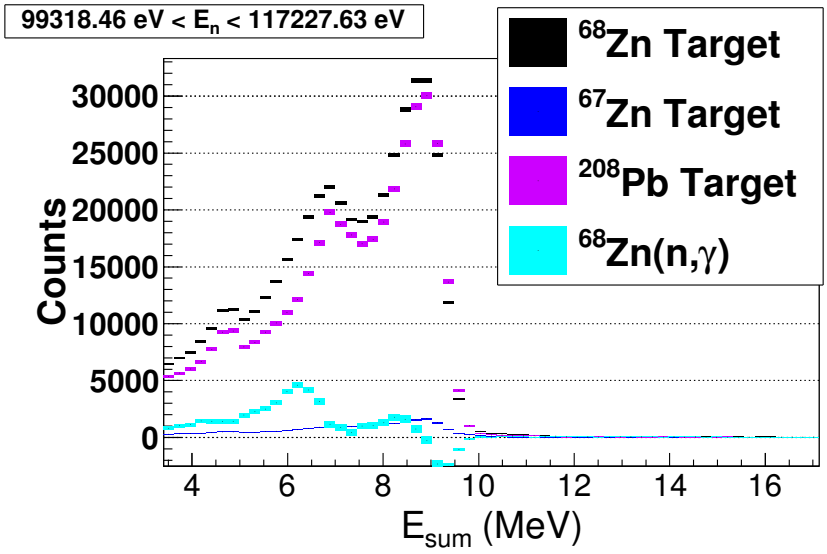

FIGURE 7.8: Representative background-subtracted E_{sum} distribution shown along with the fitted background components for 99318 eV $< E_n <$ 117228 eV.

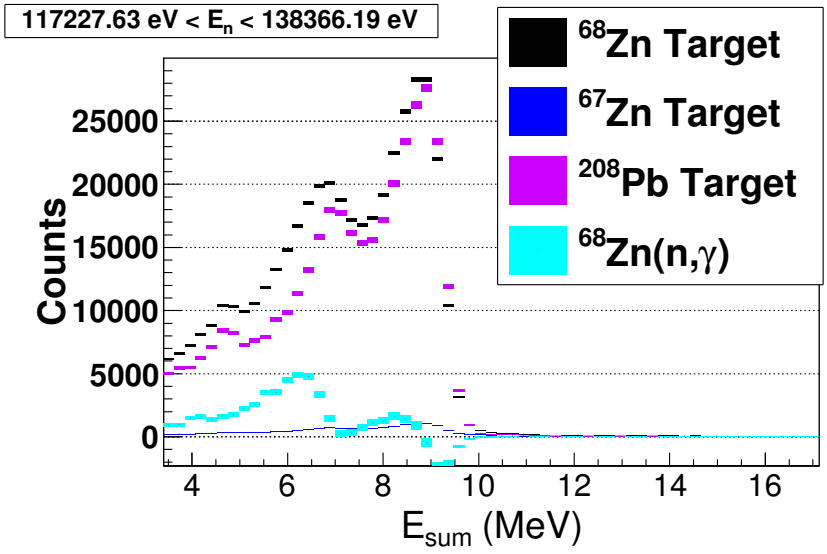

FIGURE 7.9: Representative background-subtracted E_{sum} distribution shown along with the fitted background components for 117228 eV $< E_n <$ 138366 eV.

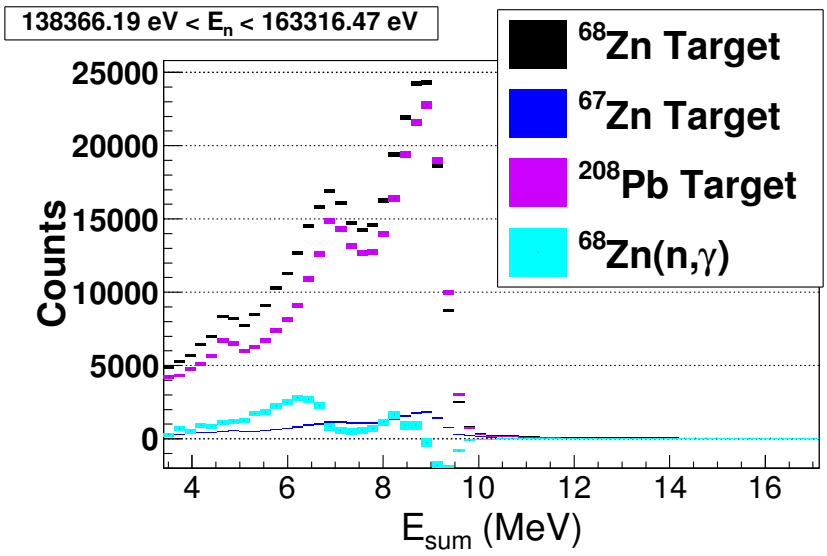

FIGURE 7.10: Representative background-subtracted E_{sum} distribution shown along with the fitted background components for 138366 eV $< E_n <$ 163316 eV.

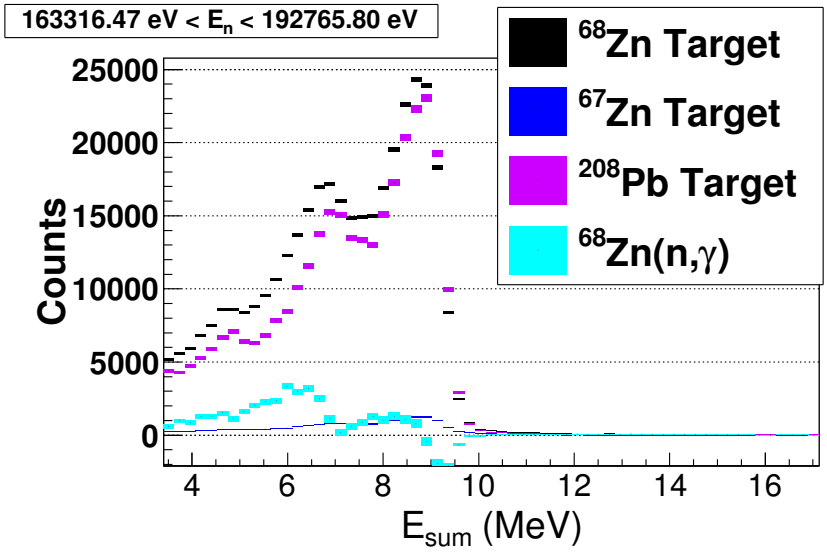

FIGURE 7.11: Representative background-subtracted E_{sum} distribution shown along with the fitted background components for 163316 eV $< E_n <$ 192766 eV.

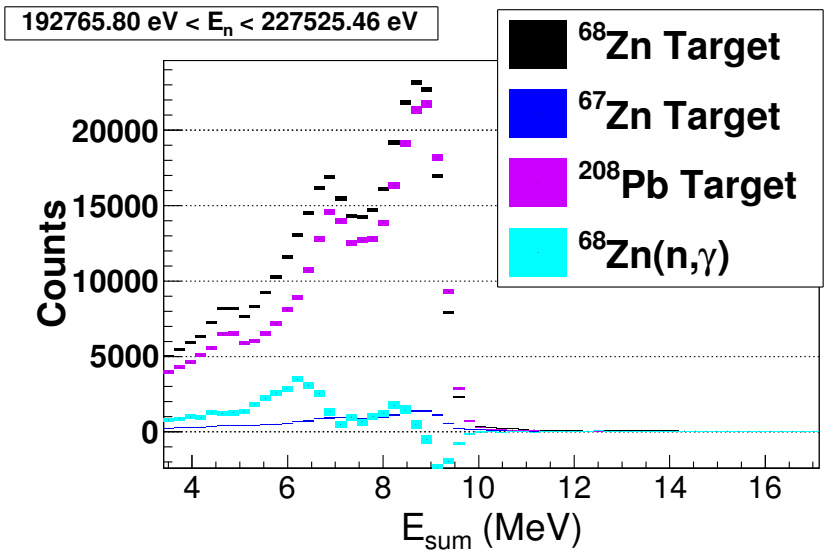

FIGURE 7.12: Representative background-subtracted E_{sum} distribution shown along with the fitted background components for 192766 eV $< E_n <$ 227525 eV.

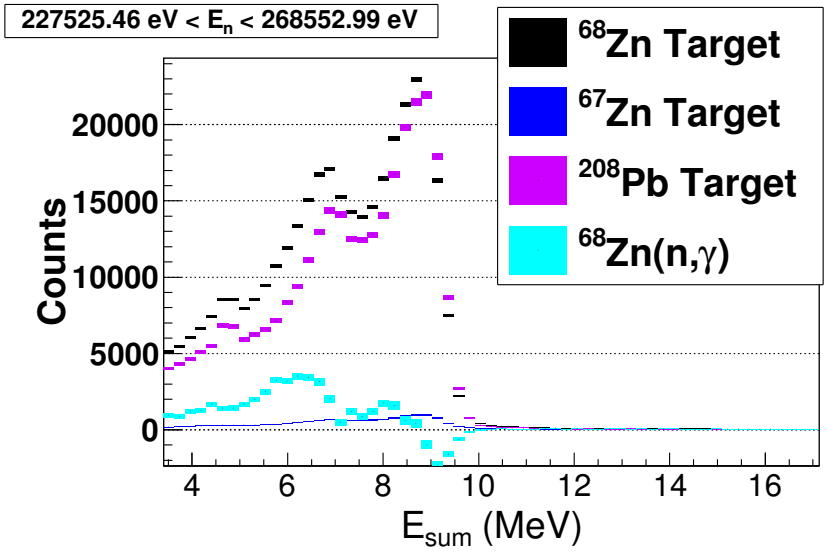

FIGURE 7.13: Representative background-subtracted E_{sum} distribution shown along with the fitted background components for 227525 eV $< E_n <$ 268553 eV.

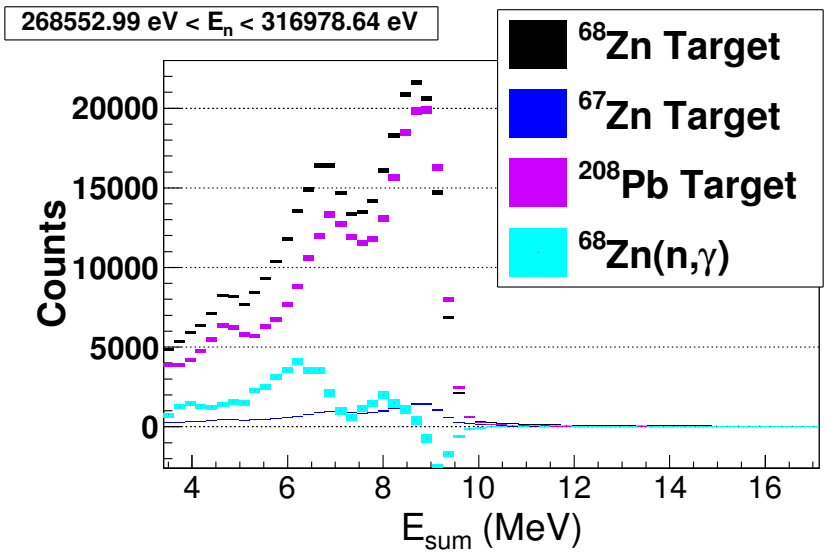

FIGURE 7.14: Representative background-subtracted E_{sum} distribution shown along with the fitted background components for 268553 eV $< E_n <$ 316979 eV.

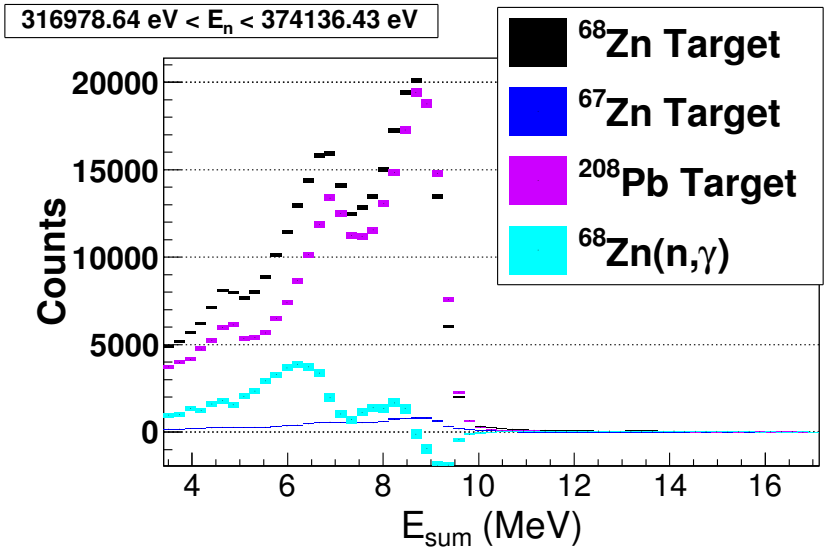

FIGURE 7.15: Representative background-subtracted E_{sum} distribution shown along with the fitted background components for 316979 eV $< E_n <$ 374136 eV.

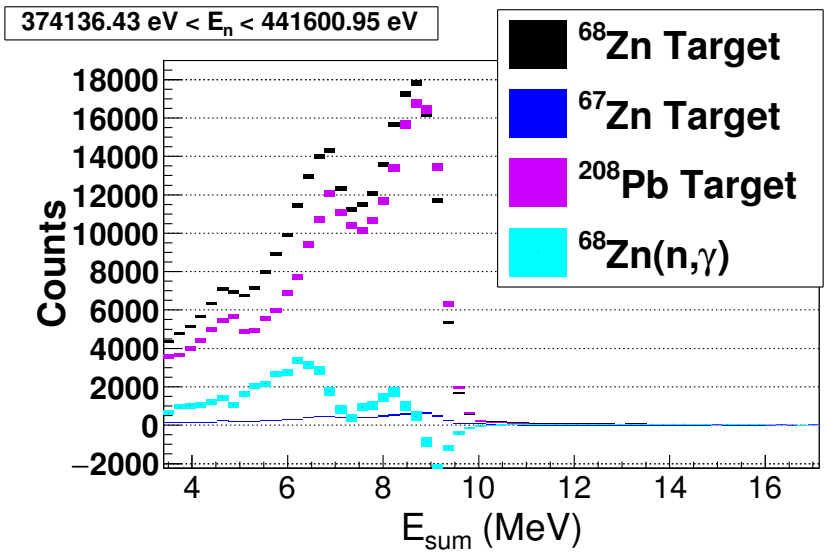

FIGURE 7.16: Representative background-subtracted E_{sum} distribution shown along with the fitted background components for 374136 eV $< E_n <$ 441601 eV.

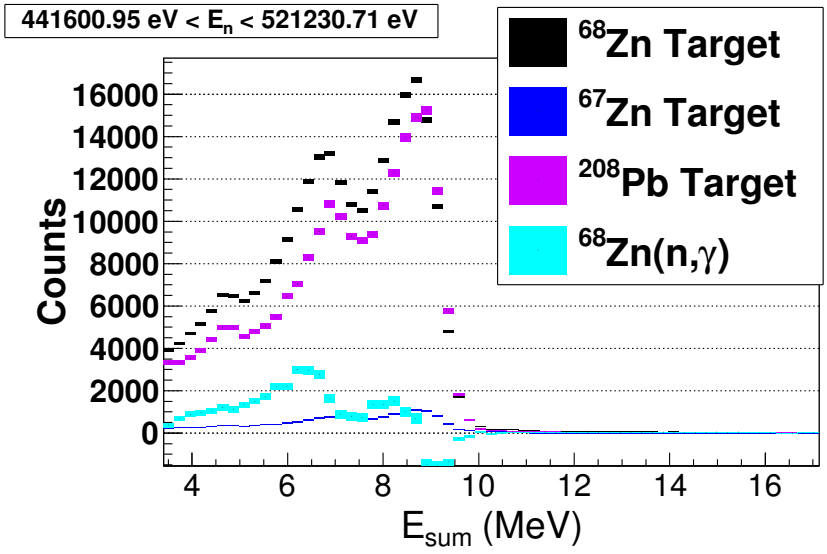

FIGURE 7.17: Representative background-subtracted E_{sum} distribution shown along with the fitted background components for 441601 eV $< E_n <$ 521231 eV.

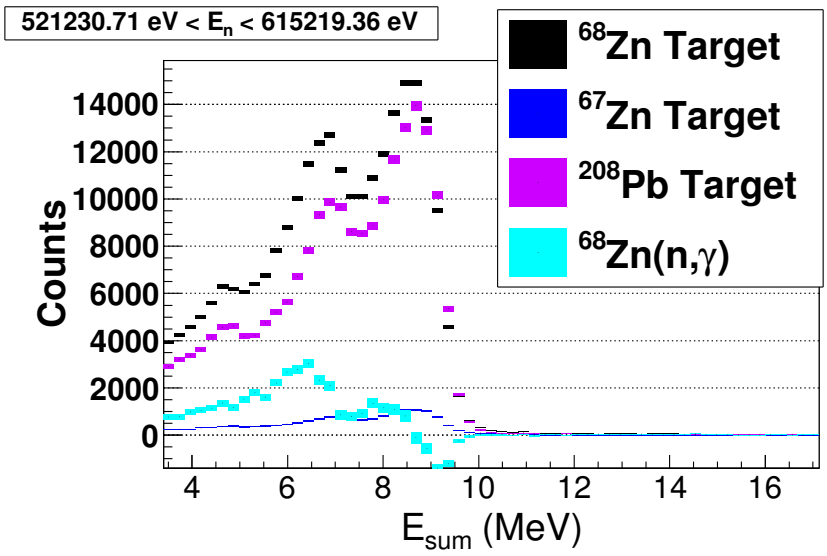

FIGURE 7.18: Representative background-subtracted E_{sum} distribution shown along with the fitted background components for 521231 eV $< E_n <$ 615219 eV.

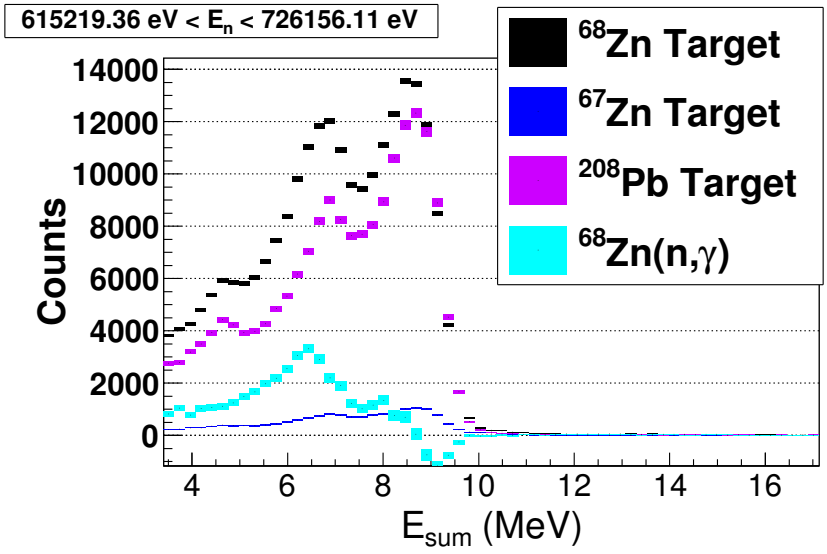

FIGURE 7.19: Representative background-subtracted E_{sum} distribution shown along with the fitted background components for 615219 eV $< E_n <$ 726156 eV.

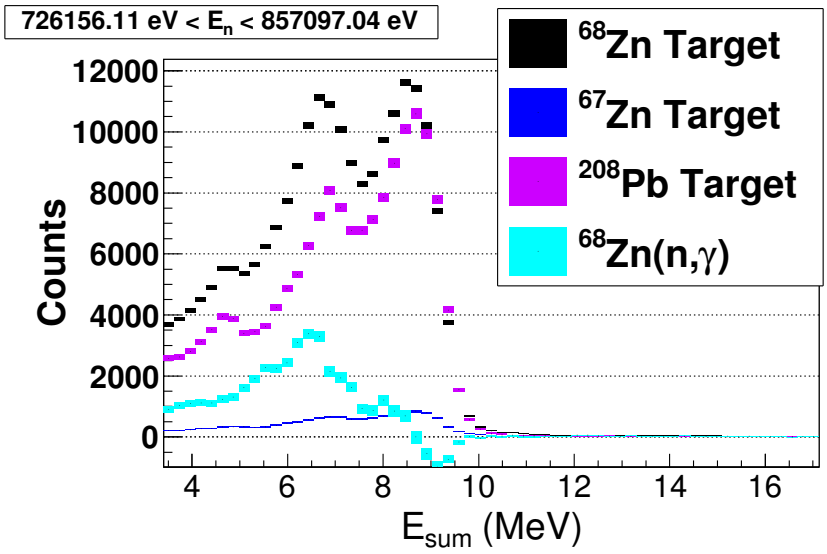

FIGURE 7.20: Representative background-subtracted E_{sum} distribution shown along with the fitted background components for 726156 eV $< E_n <$ 857097 eV.

Appendix B: DICEBOX Comparison of E_{sum} and MSC spectra for M=[2,5]

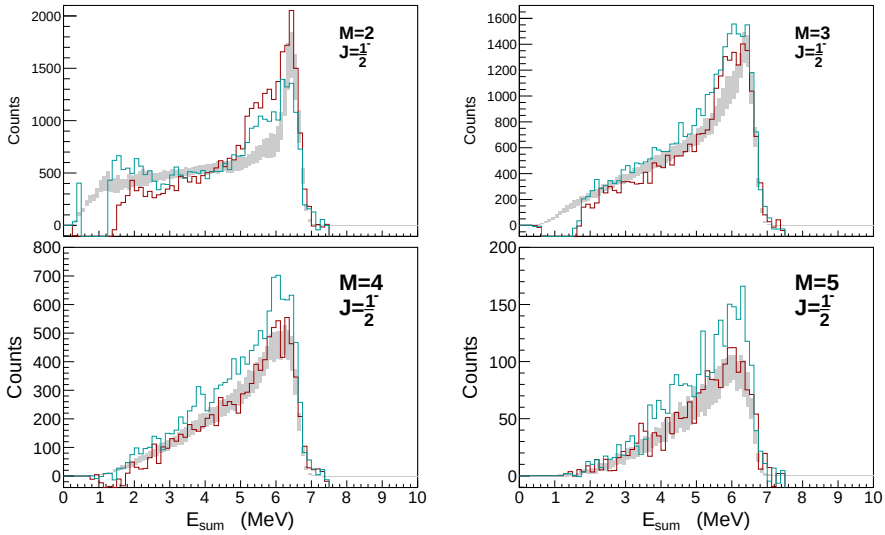

FIGURE 7.21: E_{sum} distribution comparison between data (colored lines) and DICEBOX simulation average ± std. dev. (grey band) for $J^{\pi} = \frac{1}{2}^{-}$.

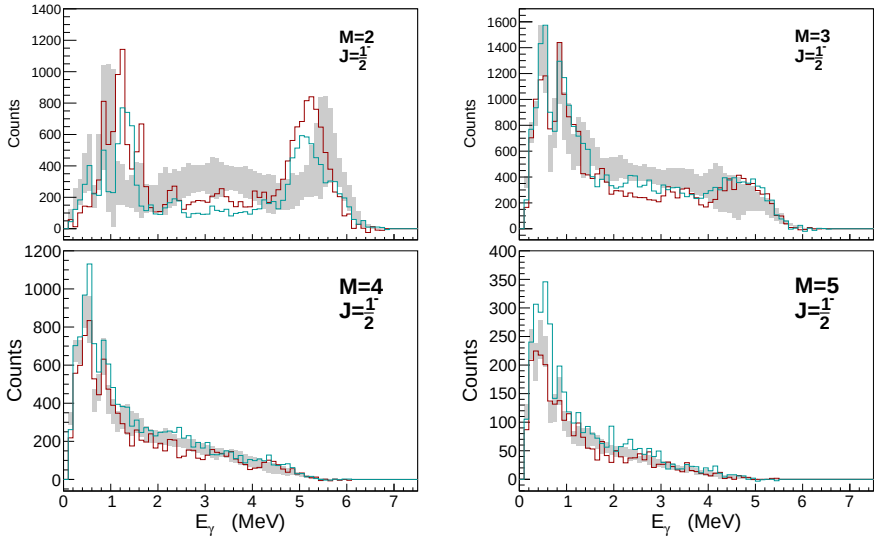

FIGURE 7.22: MSC comparison between data (colored lines) and DICEBOX simulation average ± std. dev. (grey band) for $J^{\pi} = \frac{1}{2}^{-}$ (See §3.6).

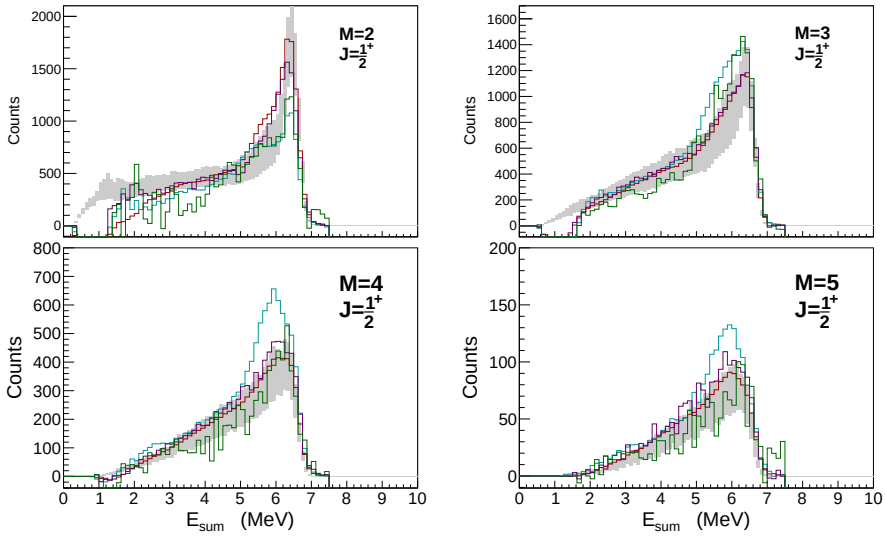

FIGURE 7.23: E_{sum} distribution comparison between data (colored lines) and DICEBOX simulation average ± std. dev. (grey band) for $J^{\pi} = \frac{1}{2}^{+}$.

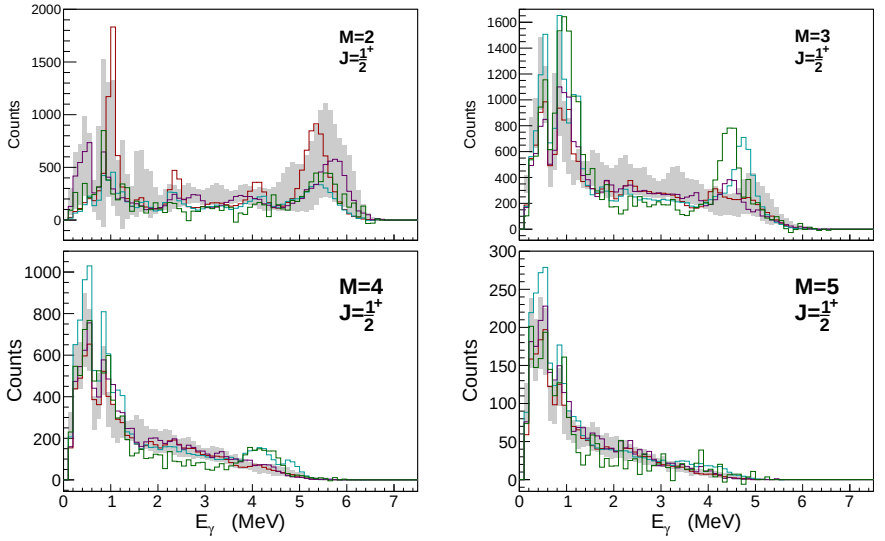

FIGURE 7.24: MSC spectra comparison between data (colored lines) and DICEBOX simulation average ± std. dev. (grey band) for $J^{\pi} = \frac{1}{2}^{+}$ (See §3.6).

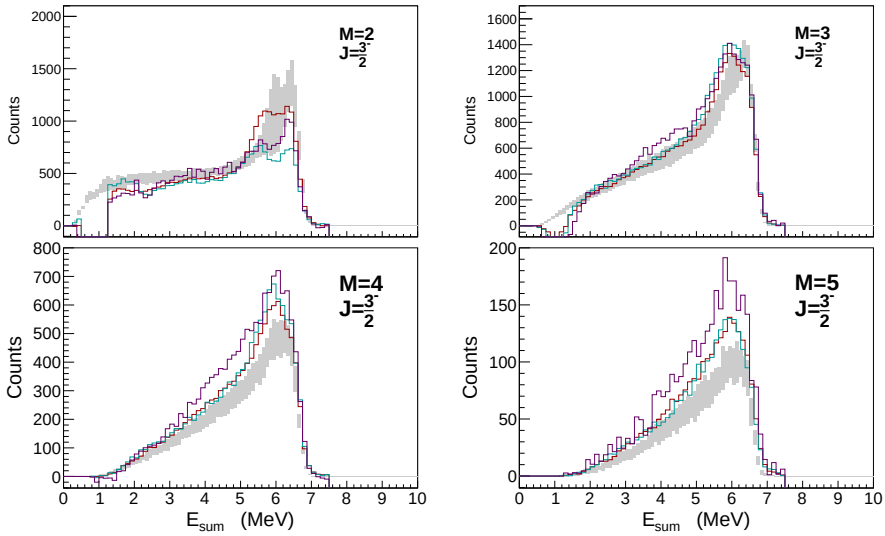

FIGURE 7.25: E_{sum} distribution comparison between data (colored lines) and DICEBOX simulation average ± std. dev. (grey band) for $J^{\pi} = \frac{3}{2}^{-}$.

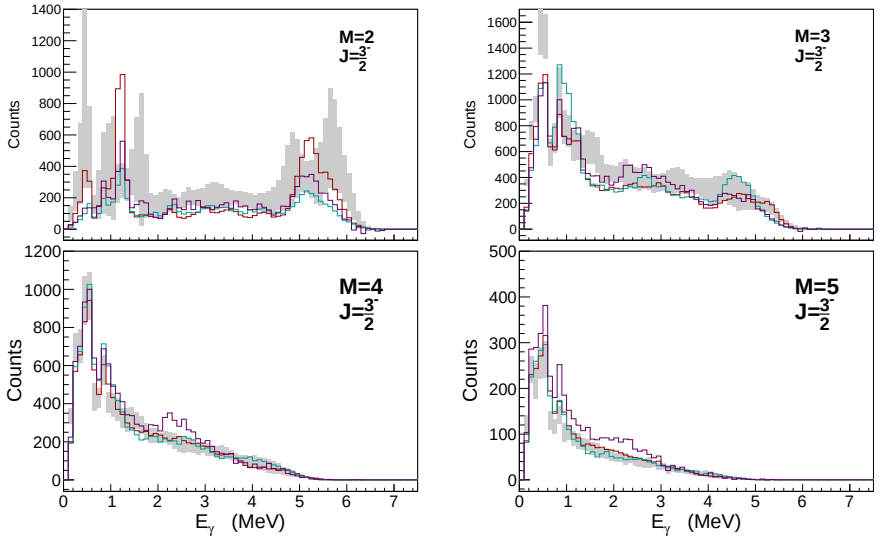

FIGURE 7.26: MSC spectra comparison between data (colored lines) and DICEBOX simulation average ± std. dev. (grey band) for $J^{\pi} = \frac{3}{2}^{-}$ (See §3.6).

Vita

Kevin Thomas Macon was born in Chapel Hill, North Carolina. Tarheel born, he completed his undergraduate studies at The University of North Carolina at Chapel Hill in May 2010. In June of 2010, he came to Louisiana State University to pursue graduate studies in physics and plans to continue his studies in a postdoctoral fellowship at Notre Dame University in South Bend, IN.